

Multi-Frequency VLBI Observations of the Active Galaxy NGC 1052

INAUGURAL-DISSERTATION

zur
Erlangung des Doktorgrades
der Mathematisch-Naturwissenschaftlichen Fakultät
der Universität zu Köln



vorgelegt von

Anne-Kathrin Baczko

aus Erlangen, Deutschland

Köln 2020

Berichtersteller:

Prof. Dr. Andreas Eckart
Prof. Dr. J. Anton Zensus

Tag der letzten mündlichen Prüfung: 18.12.2019

Abstract

Active galactic nuclei (AGN) are among the most energetic sources in the universe, a large fraction of which are visible across the entire electromagnetic spectrum. Historically a zoo of different types of AGN were categorized based on a variety of observational properties, which can be explained by one unification scheme. A subset of these sources is characterized by relativistic outflows, called jets. The standard model assumes intrinsic symmetry between the jet and the counter-jet. Radio interferometric observations provide the highest achievable resolution which is key to understanding the physics driving AGN jets.

The scope of this thesis is to investigate the physical processes responsible for the launching and collimation of relativistic jets. This is achieved with Very Long Baseline Interferometry (VLBI) at centimetre and millimetre wavelengths of the double-sided relativistic outflows within the active galaxy NGC 1052. At a distance of only 20 Mpc, linear scales down to a few hundred Schwarzschild radii can be imaged with mm-VLBI. The orientation of both jets close to the plane of the sky makes NGC 1052 an ideal target to study the symmetry-paradigm predicted by the unification scheme.

The thesis is organized as follows. The first two chapters will give an introduction on our current understanding of launching, collimation, and emission processes of AGN and their jets as well as an overview on the technique of VLBI. In chapters 3 through 5 I will present the analysis and results of a multi-frequency and multi-epoch study on NGC 1052. Chapter 6 summarizes these findings and places them within the context of current AGN/jet scholarship. Additional information on the analysis is provided in tabular and graphical form in the appendices A and B. During my thesis work I developed a set of python scripts for calibration and analysis, which are presented in appendix C. In the following I give a short overview on the main results from this dissertation.

Observations of NGC 1052 at 22 GHz and 43 GHz over 4 years suggest an intrinsic asymmetry between both jets, which evolve east- and westwards in the plane of the sky. Based on a study of the outflow velocities, the eastern jet was found to be significantly faster than the western jet. Overall faster velocities were found compared to earlier estimates performed at lower frequencies. As the observing frequency increases regions are imaged at closer proximity to the jet spine. Therefore, these results point towards a transversal velocity gradient within both jets.

The images from this study were used as input information for relativistic hydrodynamic simulations of the relativistic jets in NGC 1052. The simulations favor a scenario in which a slightly over-pressured jet, resulting from a pressure-mismatch between the jet and the ambient medium at the nozzle, penetrates into a decreasing-pressure ambient medium. A molecular torus has been included in the simulations to account for thermal absorption. Based on the simulation results the torus particle number density is estimated within the range 0.7–

$1.0 \times 10^{22} \text{cm}^{-2}$. This numerical estimate is consistent with estimates from X-ray and radio observations.

In addition, multi-frequency VLBI studies from 1.5 GHz to 86 GHz trace the absorbing effect of this torus, which covers large parts of the western, receding jet. It results in an emission gap between both jets whose size decreases with increasing frequency. Observations and simulations draw a consistent picture of the frequency-dependent thermal absorption of the non-thermal particles in the jet due to the optically thick structure. The torus only has a very small impact on the 43 GHz emission (and higher frequencies).

Both jets are extremely straight and unresolved, however, there is a slight change in the western jet direction at about 2 milliarcseconds, which cannot be observed in the eastern jet. This kind of structure can only be explained by asymmetries, intrinsic to the jet or arising from interactions with the ambient medium.

Zusammenfassung

Aktive Galaktische Kerne (AGK) gehören zu den energetischsten Quellen unseres Universums. Ein großer Teil dieser kann über das gesamte elektro-magnetische Spektrum hinweg beobachtet werden. Historisch hat sich ein Zoo verschiedenster AGK Typen entwickelt, welche sich aufgrund ihrer unterschiedlichen, beobachtbaren Eigenschaften differenzieren lassen. Diese Unterarten können innerhalb eines einheitlichen Modells beschrieben werden. Einige dieser Quellen zeigen relativistische Materieströme, welche Jets genannt werden. Das Standardmodell geht davon aus, dass beide Jets eine intrinsische Symmetrie haben. Um die physikalischen Grundgesetze zu verstehen, die AGKs antreiben, ist die höchste erreichbare Auflösung unabdingbar. Dies kann durch Radio-interferometrische Beobachtungen erreicht werden.

Im Rahmen dieser Doktorarbeit werden die physikalischen Prozesse untersucht, welche für die Erzeugung und Kollimation von Jets verantwortlich sind. Dies geschieht anhand von Beobachtungen der doppelseitigen, relativistischen Jets der aktiven Galaxie NGC 1052 mittels sehr langer Basislinieninterferometrie (VLBI) bei Wellenlängen von Zentimetern und Millimetern. Aufgrund der geringen Entfernung von 20 MPc, ist es möglich lineare Skalen von wenigen hundert Schwarzschild Radien mittels mm-VLBI zu untersuchen. Da die Jets in NGC 1052 nahezu innerhalb der Himmelsebene liegen, ist es die ideale Quelle um das Symmetrie-Paradigma, wie es vom vereinheitlichten Modell vorgeschlagen wird, genauer zu studieren.

Diese Arbeit ist wie folgt organisiert. Die ersten beiden Kapitel geben eine Einführung in unser aktuelles Verständnis von AGKs und der Erzeugung und Kollimation ihrer Jets, sowie einen Überblick über die VLBI Technik. In den Kapitel 3 bis 5 werde ich meine Analysen und Ergebnisse der Multi-Frequenz und Multi-Epochen Beobachtungen präsentieren. Kapitel 6 gibt eine Zusammenfassung der wichtigsten Ergebnisse der Arbeit und stellt sie in einen allgemeinen Kontext. Detailliertere Informationen bezüglich der Datenanalyse, welche im Haupttext präsentiert wird, wird in Form von Tabellen und Grafiken in den Anhängen A und B zur Verfügung gestellt. Im Zuge dieser Arbeit habe ich mehrere Python Skripte für die Kalibration und die Analyse der Beobachtungen entwickelt, welche in Anhang C näher beschrieben sind. Im folgenden gebe ich einen kurzen Überblick über die Hauptergebnisse dieser Dissertation.

Beobachtungen von NGC 1052 bei 22 GHz und 43 GHz über vier Jahre weisen auf eine intrinsische Asymmetrie zwischen den beiden sich nach Osten und Westen entwickelnden Jets hin. Mittels einer Analyse der Geschwindigkeiten der Materieströme in den 43 GHz Karten wurde festgestellt, dass der östliche Jet signifikant schneller ist als der Westliche. Im Vergleich mit früheren Berechnungen bei niedrigeren Frequenzen sind beide Jets schneller. Da Beobachtungen bei höheren Frequenzen Regionen im Jet abbilden, welche weiter innen liegen, deutet dies auf einen transversalen Geschwindigkeitsgradienten hin.

Die Bilder, welche aus diesen Beobachtungen resultieren, wurden als Eingangsgröße für speziell-relativistische Hydro-dynamische Simulationen verwendet, mit dem Ziel die relativistischen Jets in NGC 1052 nachzubilden. Als Ergebnis der Simulationen wird ein Szenario favorisiert, in welchem die Jets einen leichten Überdruck haben und durch ein Medium wandern, welches einen abfallenden Druckgradienten aufweist. Ein Überdruck bedeutet hierbei, dass der Druck am Entstehungspunkt des Jets höher ist als in dem ihn umgebenden Medium. Ein molekularer Torus wurde in die Simulationen einbezogen um thermische Absorption einzubeziehen. Unter Berücksichtigung der Simulationsergebnisse übereinstimmen die berechneten Teilchendichten von $0.7\text{--}1.0 \times 10^{22} \text{cm}^{-2}$ mit Abschätzungen aus Röntgen und Radio Beobachtungen.

Des weiteren wurden mittels VLBI Beobachtungen bei Frequenzen zwischen 1.5 GHz und 86 GHz die Absorptionseigenschaften des Torus untersucht, welcher große Teile des westlichen, sich von uns weg bewegenden Jets, überdeckt. Das Resultat ist eine Emissionslücke zwischen beiden Jets, deren Größe mit höherer Beobachtungsfrequenz kleiner wird. Sowohl Beobachtungen, als auch Simulationen, zeichnen ein konsistentes Bild einer frequenzabhängigen Absorption der nicht-thermischen Jet Teilchen in einer optisch dicken, zirkularen Struktur.

Beide Jets sind extrem gerade und unaufgelöst, wobei eine kleine Änderung der Jet Richtung bei ungefähr 2 Millibogensekunden im westlichen Jet beobachtet werden kann, welche im östlichen Jet nicht zu sehen ist. Diese Art von Struktur kann nur durch Asymmetrien erklärt werden, welche entweder intrinsisch im Jet vorkommen oder vom umgebenden Medium herühren.

Contents

List of Figures	III
List of Tables	V
1. Introduction	1
1.1. Active galactic nuclei	1
1.1.1. AGN unification	2
1.1.2. The central engine	4
1.1.3. Jets in AGN – formation and evolution	5
1.2. NGC 1052 – Radio-centric view of a double-sided jet in the plane of the sky .	7
1.3. Motivation of the herein presented work	9
2. Theory	12
2.1. Synchrotron radiation	12
2.2. Brightness temperature	13
2.3. Relativistic effects in AGN	15
2.3.1. Beaming and superluminal motion	15
2.4. Very Long Baseline Interferometry	17
2.4.1. Measuring radio signals	18
2.4.2. The basics of radio interferometry	18
2.4.3. VLBI calibration	21
2.4.4. Amplitude calibration	23
2.4.5. Imaging	24
3. Study of the asymmetry in the jet formation in NGC 1052	26
3.1. Data reduction	26
3.2. Results	30
3.2.1. Image stacking	31
3.2.2. Spectral Index maps	33
3.2.3. Flux density evolution	37
3.2.4. Kinematics	38
3.2.5. Brightness temperature and opening angle	39
3.3. Discussion	41
3.3.1. Torus	41
3.3.2. Jet properties	43
3.3.3. Source geometry	46

3.4. Using evolutionary algorithms to model relativistic jets	50
3.4.1. Simulation setup	50
3.4.2. Results from the the simulations	51
3.5. Conclusions	55
4. Multi-frequency observations of NGC 1052	57
4.1. Data reduction	57
4.1.1. Multi-frequency VLBA observations of NGC 1052	57
4.1.2. RadioAstron observation of NGC 1052	59
4.2. Results of the multi-frequency VLBA observation of NGC 1052	64
4.2.1. Image alignment	64
4.2.2. Component identification	66
4.2.3. Spectral analysis	68
4.2.4. Ridge-Line Analysis	70
4.3. Results of RadioAstron observation of NGC 1052	73
4.3.1. Ridge-Line Analysis	73
4.4. Discussion	74
4.4.1. Expansion of the jets in NGC 1052	77
4.4.2. Jet bending and precession or interaction with the ambient medium	78
4.5. Summary & Conclusions	78
5. GMVA observation of NGC 1052 in 2017	80
5.1. Data reduction, results and discussion	80
6. Summary & Outlook	86
Bibliography	VII
A. VLBA multi-epoch observation – parameters and additional figures	XIII
B. Images, alignment, and model fitting results of NGC 1052 from the VLBA multi-λ and RadioAstron data sets	XXIV
B.1. VLBA multi-frequency observation of NGC1052	XXIV
B.2. RadioAstron observation of NGC1052	XXXII
C. Development of Python scripts for calibration and analysis	XXXIII
C.1. Calibration using AIPS and PARSELTONGUE	XXXIII
C.1.1. ParseLTongue setup	XXXV
C.2. Data analysis Python scripting	XL

List of Figures

1.1. Intro: AGN unified model	3
1.2. Intro: image of M 87 taken with the EHT at 230 GHz	5
1.3. Intro: CD kink instabilities on large scales	7
1.4. Intro: NGC 1052 Radio morphology	8
1.5. Intro: GMVA detection of NGC1052	10
2.1. Theory: synchrotron spectrum	14
2.2. Theory: superluminal motion	15
2.3. Theory: atmospheric opacity depending on wavelength.	17
2.4. Theory: feed horns	19
2.5. Theory: basic two-element interferometer.	20
3.1. VLBA multi-epoch: gscale statistic	30
3.2. VLBA multi-epoch: clean maps with model-fit components overplotted . . .	31
3.3. VLBA multi-epoch: clean maps with model-fti components overplotted . . .	32
3.4. VLBA multi-epoch: stacked images for all observations from 2005 to 2009. .	33
3.5. VLBA multi-epoch: alignment and spectral index	35
3.6. VLBA multi-epoch: stacked spectral index map	36
3.7. VLBA multi-epoch: flux density ratios	37
3.8. VLBA multi-epoch: kinematics	38
3.9. VLBA multi-epoch: distance vs Tb and Major ax	40
3.10. VLBA multi-epoch: individual stacked images	44
3.11. VLBA multi-epoch: histogram of the apparent velocity	45
3.12. VLBA multi-epoch: parameter space $\theta_{\text{LOS}}\text{-}\beta$	45
3.13. VLBA multi-epoch: light curve based on model-fit components	47
3.14. Simulations: rest-mass density distribution for OP and PM jet	51
3.15. Simulations: simulation results for OP and PM jet	52
3.16. Simulations: synthetic multi-frequency VLBA images	53
3.17. Simulations: RA and GVMVA synthesis images	54
4.1. VLBA multi-frequency: projplot of C-Band image.	58
4.2. VLBA multi-frequency: final clean images.	59
4.3. RadioAstron: full uv-coverage.	60
4.4. RadioAstron: possm plot examples	62
4.5. RadioAstron: CLEAN images.	63
4.6. VLBA multi-frequency: alignment 1.5 GHz-5 GHz	65
4.7. VLBA multi-frequency: alignment 8.4 GHz-15 GHz	66

4.8. VLBA multi-frequency: contour maps with model components plotted on top.	67
4.9. VLBA multi-frequency: spectral index maps.	68
4.10. VLBA multi-frequency: spectrum for individual regions.	69
4.11. VLBA multi-frequency: jet-to-counterjet Ratio.	70
4.12. VLBA multi-frequency: original clean images with ridge-lines	71
4.13. VLBA multi-frequency: restored clean images with ridge-lines	72
4.14. VLBA multi-frequency: ridge-lines for restored clean images	73
4.15. VLBA multi-frequency: jet width and flux along the ridge-line	74
4.16. RadioAstron: clean image with ridge-line	75
4.17. RadioAstron: jet ridge-lines for RA and VLBA U, K, and Q	75
4.18. RadioAstron: jet width and flux along ridge-line RA and VLBA U, K, and Q	76
5.1. GMVA: CLEAN images	81
5.2. GMVA: uv -coverage of the 86 GHz observation	82
5.3. GMVA: projplot	83
5.4. GMVA: CLEAN images	84
5.5. GMVA: CLEAN Continuum spectrum from 1.5 GHz to 86 GHz	85
A.1. VLBA multi-epoch: individual Spectral index maps	XXI
B.1. VLBA multi-frequency: convolved maps	XXVII
B.2. VLBA multi-frequency: convolved maps	XXVII
B.3. VLBA multi-frequency: convolved maps	XXVIII
B.4. VLBA multi-frequency: ridge-lines for original clean images	XXIX
B.5. VLBA multi-frequency: freq. vs flux density	XXX
B.6. VLBA multi-frequency: freq. vs brightness temperature	XXXI
B.7. RadioAstron: FOURFIT example baseline ATCA-Hobart	XXXII
C.1. Scripting: calibration routine in AIPS for a VLBA observation	XXXIV
C.2. Scripting: python modules for calibration using PARSELTONGUE	XXXV
C.3. Example of the process to re-grid two given images and convolve them with the same beam. The two shown images at 1.5 GHz and 5 GHz are described in chapter 4. Before re-gridding the images did had a different fov. However, the images shown in the top panels are shrieked to the fov of the final images in the bottom panels, to better visualize the process of blurring with a larger beam.	XLIII

List of Tables

3.1. VLBA multi-epoch: image parameters 22 & 43 GHz	27
3.1. VLBA multi-epoch: image parameters 22 & 43 GHz	28
3.1. VLBA multi-epoch: image parameters 22 & 43 GHz	29
3.2. VLBA multi-epoch: common beam for spectral index maps	37
3.3. VLBA multi-epoch: averaged speeds for both jets	39
3.4. VLBA multi-epoch: fit parameter for brightness temperature and jet diameter	41
4.1. VLBA multi-frequency: CLEAN image parameters.	60
4.2. RadioAstron: CLEAN image parameters.	64
4.3. VLBA multi-frequency: shifts	65
5.1. GMVA: CLEAN image parameters	82
A.1. VLBA multi-epoch: model-fit component parameters	XIII
A.2. VLBA multi-epoch: model-fit component parameters	XIV
A.3. VLBA multi-epoch: model-fit component parameters	XV
A.4. VLBA multi-epoch: model-fit component parameters	XVI
A.5. VLBA multi-epoch: model-fit component parameters	XVII
A.6. VLBA multi-epoch: model-fit component parameters	XVIII
A.7. VLBA multi-epoch: model-fit component parameters	XIX
A.8. VLBA multi-epoch: model-fit component parameters	XX
A.9. VLBA multi-epoch: velocities	XXII
A.10. VLBA multi-epoch: <i>gscale</i> statistics	XXIII
B.1. VLBA multi-frequency: Gaussian model fit parameters	XXIV
B.1. VLBA multi-frequency: Gaussian model fit parameters	XXV
B.1. VLBA multi-frequency: Gaussian model fit parameters	XXVI

1 | Introduction

When thinking about galaxies, beautiful images as taken from the Hubble space telescope come to mind. Dominated by the thermal emission of millions of stars, large-scale structures of dust draw fascinating pictures in the sky, tracing large-scale spiral arms. There is a subclass called active galaxies which show a different kind of morphology. The whole stellar population is outshined by the most central area of the galaxy, where a vast amount of energy is produced that cannot be explained by thermal emission. Moreover, these galaxies are bright over the whole electro magnetic spectrum from radio over optical, x-rays, and even up to γ -rays. Their centers are called active galactic nuclei (AGN).

Even though they have been studied extensively since the beginning of the 20th century, our understanding of the physical mechanism driving these peculiar sources is vague. This PhD thesis is aimed to enrich our understanding of AGN by means of high-resolution studies at radio wavelengths of the galaxy NGC 1052. It is organized as follows: In chapter 1 I give a short introduction on AGN and our current understanding of the physical mechanisms behind their existence. Chapter 2 will describe the basic concepts and theoretical background needed later in the interpretation of the results and the discussion. Chapter 3 presents the outcome from a multi-epoch observation of the galaxy NGC 1052 at two frequencies. In Chapter 4 a multi-frequency dataset from 1.5 GHz up to 43 GHz is discussed. Chapter 5 presents radio observations at 86 GHz and chapter 6 will combine all presented results to draw a consistent picture of NGC 1052 and its impact on our understanding of AGNs. Throughout the thesis, figures without any reference in the caption are produced by myself. For clarity many tables and figures, as well as scripts and methods developed explicitly for this work will be presented as appendices at the end of the manuscript.

1.1. Active galactic nuclei

In this section I will give a short introduction on our current understanding of AGN starting with a historical view spanning over a century of astronomical observations. A more deep view on the underlying physics and classifications based on observed quantities can be found in [Urry & Padovani \(1995\)](#); [Zensus \(1997\)](#); [Marscher \(2009\)](#), and [Blandford et al. \(2019\)](#)

The history of AGN research reaches back to the beginning of the 20th century, when the optical spectra of the spiral nebulae in NGC 1068 revealed bright emission lines ([Fath 1909](#)). However, it took until the early 1940s that the work by [Seyfert \(1943\)](#) suggested a new type of galaxy based on the first systematic study of spectra of spiral nebulae which revealed broad optical emission lines. Today a subset of AGN are called "Seyfert galaxies", classified on their optical spectrum and mostly found in spiral galaxies. From there on the era of

AGN studies developed. One decade later, Baade & Minkowski (1954) detected the first radio galaxy: Cygnus A, which was identified with an extragalactic object and found to have a larger amount of energy emitted in the radio band compared to the total optical emission. In 1963, 3C 273 was associated with a compact optical counterpart at a cosmological distance of $z = 0.158$ (Schmidt 1963). This marks the discovery of so called quasi-stellar radio sources (quasars), which resembled stars in the optical images with respect to the point-like structure observed. In the following years more and more sources resembling the first detected extragalactic strong radio emitters were discovered and studied over a wide range of frequencies. The idea of an active galactic nucleus residing in the center of a subset of special galaxies was born.

Since then a vast amount of different types of AGN had been discovered leading to a zoo of different classifications. A complete review can be found in e.g., Krolik (1999) or Carroll & Ostlie (2017).

Based on the ratio of radio flux density at 5 GHz to the optical total flux at 4400Å AGN can be divided into being radio-quiet (ratio below 10) or radio-loud (ratio above 10) as established by (Kellermann et al. 1989). Seyfert galaxies are typically referred to being radio-quiet. They can be divided into two additional subclasses. The optical spectrum of Seyfert of type 1 shows thin as well as broad emission lines, whereas type 2 lack broad emission lines. Another class is known for being the brightest types within the AGNs, blazars (blazing quasi stellar objects), which resemble radio-loud quasars. Only 10% of AGN are radio-loud.

Radio galaxies can be seen as radio-loud counterparts of Seyfert galaxies, as both classes share similar occurrence of narrow and broad emission lines, distinguishing further into Narrow Line Radio Galaxies (NLRGs) and Broad Line Radio Galaxies (BLRGs). Typically two jets are observed and in most cases also bright radio lobes as well as hotspots. Contrary to Seyfert galaxies radio galaxies are often found in giant elliptical galaxies.

Another extension to Seyfert galaxies are so called Low Ionization Nuclear Emission Line Region (LINER) galaxies, which are very similar to Seyfert type 2, except the addition of strong low ionization lines (mostly OI $\lambda 6300\text{\AA}$; NII $\lambda\lambda 6548\text{\AA}, 6583\text{\AA}$), whereas continuum emission is normally weaker.

Fanaroff & Riley (1974) introduced another classification based on the morphology of the sources. Whereas Fanaroff-Riley (FR) type I are dominated by a bright central feature, and show typically a double-sided jet which decreases in flux density with distance, FR type II have only a one-sided jet, and two radio lobes, which often show bright hotspots.

1.1.1. AGN unification

All these different classes of AGN have in common to be the brightest objects in the universe, exceeding luminosities of $L_{\text{rad}} \gtrsim 10^{38} \text{erg s}^{-1}$ (Blandford et al. 2019). A variability on scales from hours, over months to years suggest the center to be smaller than a lightday ($3 \times 10^{13} \text{m}$). The amount of emitted energy cannot be explained by thermal processes (typical efficiency $\eta \sim 0.007$), but requires the efficiency only reached by the accretion of matter onto a black hole (BH) (typical at least $\eta \sim 0.1$).

Within the unified model of AGN, the different subclasses and observed properties can

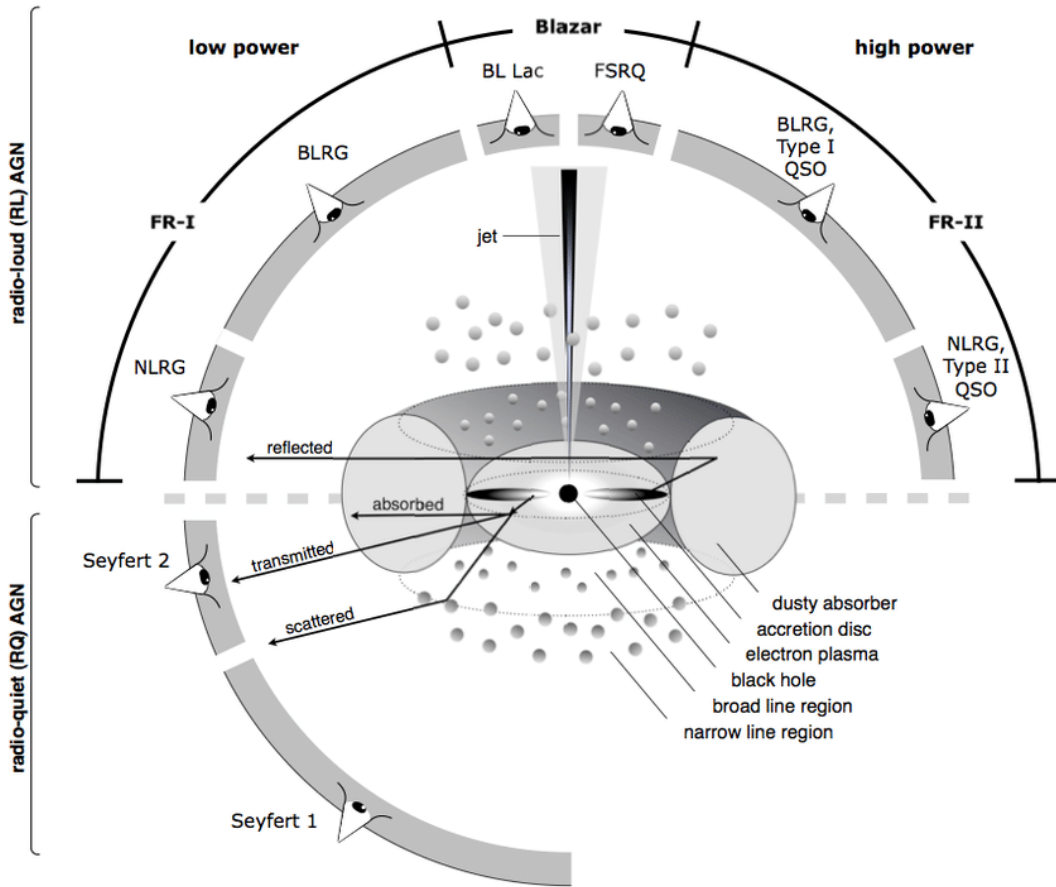


Figure 1.1.: Schematic sketch of the AGN structure based on the unification scheme (Beckmann & Shrader 2012).

be explained by a single model, consisting of a supermassive black hole (SMBH), which is surrounded by matter in form of an accretion disk (AD), a cold dusty torus, several orbiting clouds resulting in narrow and broad emission lines depending on their distance to the SMBH and thus having different velocities, and bipolar jets which are launched perpendicular to the accretion disk (compare Fig. 1.1 and Antonucci (1993); Urry & Padovani (1995)). The jets are highly collimated outflows which are accelerated towards relativistic speeds. The different classes and morphologies can then be explained simply by different viewing angles onto the AGN. For example a viewing angle of 0° would mean to look directly onto the relativistic jet, having the properties of a blazar. Whereas an angle of 90° leads to the observational properties of a radio galaxy.

The vast amount of energy released by an AGN cannot be explained by thermal processes, but is thought to have its origin in the emission of relativistic particles. Emission observed in the frequency range of $10^5 \text{ Hz} < \nu < 10^{16} \text{ Hz}$ can be explained by synchrotron radiation of relativistic, charged particles (see e.g., Pacholczyk 1970). Hence, the total power emitted by a

single electron is:

$$P_{\text{sync}} = \frac{4}{3} \sigma_T c \beta^2 \gamma^2 U_B , \quad (1.1.1)$$

where $\sigma_T = 8\pi r_e^2/3$ is the Thompson cross section with the classical electron radius $r_e = e^2/(m_e c^2)$ and the density of the magnetic field $U_B = B^2/8\pi$ (Rybicki & Lightman 1979). For more details on synchrotron radiation see Sect. 2.1

In the following sections I will shortly introduce the main constituents of the unified model. For a deeper understanding see Krolik (1999); Antonucci (1993); Urry & Padovani (1995) and Marscher (2009).

1.1.2. The central engine

The main driver of the AGN activity is the supermassive black hole (SMBH) with masses of $\sim 10^6 - 10^9 M_\odot$. A strong gravitational potential as it is the case for a SMBH is the only possibility to explain the amount of energy release in AGN. A black hole (BH) can be described by its mass M_{BH} and spin a . A possible charge of the BH is not relevant on astronomical scales and can be neglected because the infalling material will have no net electric charge. An important term for a BH is the so called *event horizon*, which represents the radius below which not even light can escape. A non-rotating BH is described within the Schwarzschild metric and the event horizon equals the so called Schwarzschild radius R_S , defined as:

$$R_S = \frac{2GM_{\text{BH}}}{c^2} \equiv 3 \frac{M_{\text{BH}}}{M_\odot} \text{km} \equiv 0.020 \text{AU} \frac{M_{\text{BH}}}{M_\odot} , \quad (1.1.2)$$

with the solar mass $M_\odot = 1.9891 \times 10^{30} \text{kg}$, the astronomical unit $\text{AU} = 1.5 \times 10^{11} \text{m}$, the gravitational constant G , and the speed of light c . It is convenient to also define the gravitational radius $R_g = 2R_S$, which is independent of the BH spin.

The Kerr metric (Kerr 1963) on the other hand describes a rotating black hole with a spin $a = (Jc)/(GM_{\text{BH}}^2)$, where J is the angular momentum of the BH and $0 \leq a \leq 1$. A non-zero spin reduced the size of the event horizon R_k as:

$$R_k = 2R_g(1 - \sqrt{1 - a^2}) . \quad (1.1.3)$$

A region important for the launching of AGN jets from a rotating BH is the ergosphere, which is outside of the event horizon and has a radius of:

$$R_e = R_g(1 - \sqrt{1 - a^2 \cos^2 \theta}) , \quad (1.1.4)$$

where θ is the angle measured from the pole of rotation. In this area the rotation of a BH causes the Lense-Thirring effect or frame dragging (see e.g., Bardeen & Petterson 1975) and allows matter inside the ergosphere to extract rotational energy from the BH.

Recently, the first image of the direct surrounding of the SMBH in the AGN M 87 at event-horizon scales was taken by the event horizon telescope (EHT EHT Collaboration et al.

(2019a); see Fig. 1.2). The final image reveals an asymmetric ring with a diameter of $43 \pm 3 \mu\text{as}$ and is consistent with the expectations of a Kerr black hole.

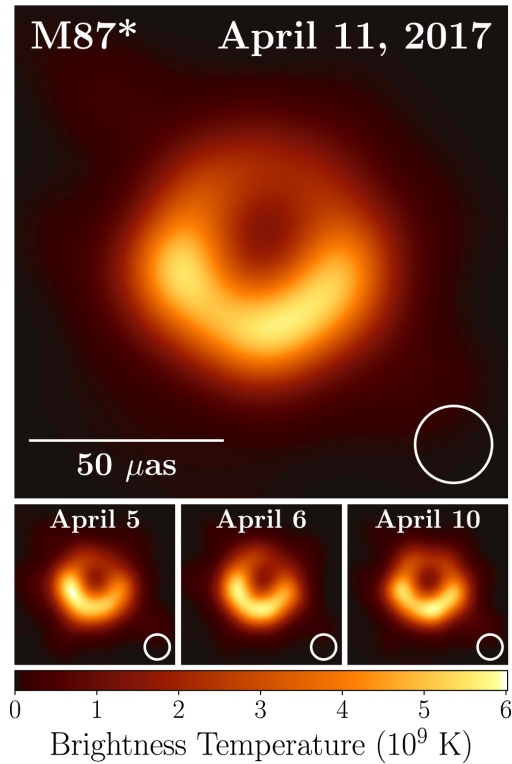


Figure 1.2: Image of M87, taken with the EHT at 230 GHz (EHT Collaboration et al. 2019a). The color scale represents the brightness temperature (see definition in Sect. 2.2) (Top:) averaged image for April 11, 2019 (Bottom:) similar images from three different days. The image is consistent with general relativistic magnetohydrodynamic (GMRHD) models of a Kerr black hole. It shows the so called *shadow* (e.g., Falcke et al. 2000) of the black hole as a central flux depression and an asymmetric *photon ring*. It can be explained by a SMBH spin pointing away from the Earth and the thus resulting effects of Doppler beaming on the moving plasma.

1.1.3. Jets in AGN – formation and evolution

How relativistic jets in AGN are formed and collimated is still not fully understood. Emitting over a wide range from radio up to GeV and TeV the jets accelerate to superluminal apparent velocities up to $\beta_{\text{app}} \sim 50c$ (MOJAVE, Lister et al. 2009). AGN jets typically have a power of $10^{43} - 10^{48} \text{ erg s}^{-1}$ (Ghisellini et al. (2014)). While penetrating the interstellar medium, jets may be slowed down and at some distance lobes are formed at their heads (Carroll & Ostlie 2017), probably forming a sharp shock feature in form of a hot spot. Even though several theories on the physical mechanism driving AGN jets exist, it is, yet, not fully understood how they are launched and how it is possible to keep them collimated up to distances of kpc, in rare cases even Mpc. Our current understanding is that they are launched by relativistic magnetohydrodynamics (RMHD) processes. These require large magnetic fields, whose origin could not be clarified observationally. There are two main theoretical models aiming to describe the process of launching: 1) as described by Blandford & Znajek (1977) with the ergosphere of the BH as the driving force or 2) following Blandford & Payne (1982) via the accretion disk. As observation do not clearly favor one of the two models, a big attempt in understanding the physics behind jet launching, acceleration and collimation is made by a large number of 2D and 3D numerical simulations.

Jet launching

As mentioned above one possibility to launch a relativistic jet is driven by the spinning black hole as described in [Blandford & Znajek \(1977\)](#). As stated in Sect. 1.1.2, matter within the ergosphere of a spinning BH extracts rotational energy from the BH via the Lense-Thirring effect or the Penrose mechanism ([Penrose & Floyd 1971](#)). There are magnetic fields expected to be frozen in the ergosphere of the BH. The Lense-Thirring effect results in a differential rotation of the magnetic field lines (see e.g., [Tchekhovskoy 2015](#)). As a final result magnetic field lines are pushed outwards guiding the escaping particles away from the center as bipolar outflows perpendicular to the AD.

The second way of jet launching is described by [Blandford & Payne \(1982\)](#) in which the magnetic field is anchored to the accretion disk. The jet is launched by magnetocentrifugal acceleration (see e.g., [Meier et al. 2001](#)). Whether the jets consist of electrons and positrons, light particles, or an electron-proton plasma is not yet clear ([Celotti & Fabian 1993](#); [Reynolds et al. 1996](#)).

As shown by several numerical simulations, jets launched by the [Blandford & Znajek \(1977\)](#) mechanism are faster as when launched by a magnetized accretion wind ([Blandford & Payne 1982](#)), see for example discussion in [Hawley & Krolik \(2006\)](#). Observations have revealed several different speed systems within the same jet (see for example the case of M 87, [Mertens et al. 2016](#)), showing a faster inner layer (spine) and a slower moving outer layer (sheath), which suggests that both ways of jet launching could co-exist within the same object.

Collimation – how to overcome instabilities

Another mystery of AGN jets are their collimation over large distances. In theory there are several mechanisms of instabilities which should result in de-collimation of the jets. Two examples are current-driven (CD) kink instabilities and Kelvin-Helmholtz instabilities (KH) for a magnetically and kinetically-dominated jet, respectively (see reviews by [Hardee 2008](#); [Perucho et al. 2012](#)). CD instabilities arise from a toroidal magnetic field resulting in a magnetically unstable jet. KH instabilities can be explained by a high velocity gradient between ambient medium and jet, and may even disrupt the jet [Perucho et al. \(2012\)](#). Among the processes that may help in reducing the impact of instabilities are high Lorentz factors, hot sheath layers around the jet, or poloidal, organized magnetic fields ([Hardee 2008](#); [Perucho et al. 2012](#)).

3D MHD simulations have shown that large-scale bends and stalling of the jets can be explained by kink instabilities (see Fig. 1.3; [Tchekhovskoy & Bromberg \(2016\)](#)). Further, the authors showed that the morphology of FR I and FR II can be reproduced by kink instabilities and different jet powers. Panels a) and b) in Fig. 1.3 use a powerful jet with $L_j \simeq 1.5 \times 10^{46} \text{erg s}^{-1}$ and panel c) a low power jet with $L_j \simeq 1.5 \times 10^{44} \text{erg s}^{-1}$. The model in panel a) assumes a flat power-law density profile of the ambient medium and in panel b) a break in the density of the ambient medium having a steeper profile at larger distance. The jets in a) and b) appear very straight until the development of backflows and hotspots. The jets are not much dependent on the density profile of the ambient medium. There are large scale bends observable due to kink instabilities. In case of the low power jet (Panel c) instabilities

are much more violent and stop the jet at a critical distance $r_c \sim 5 \text{ kpc}$ for a duration similar to the jet lifetime. Even after propagation has initiated again, both jets are affected by kink instabilities, leading to bending and precession.

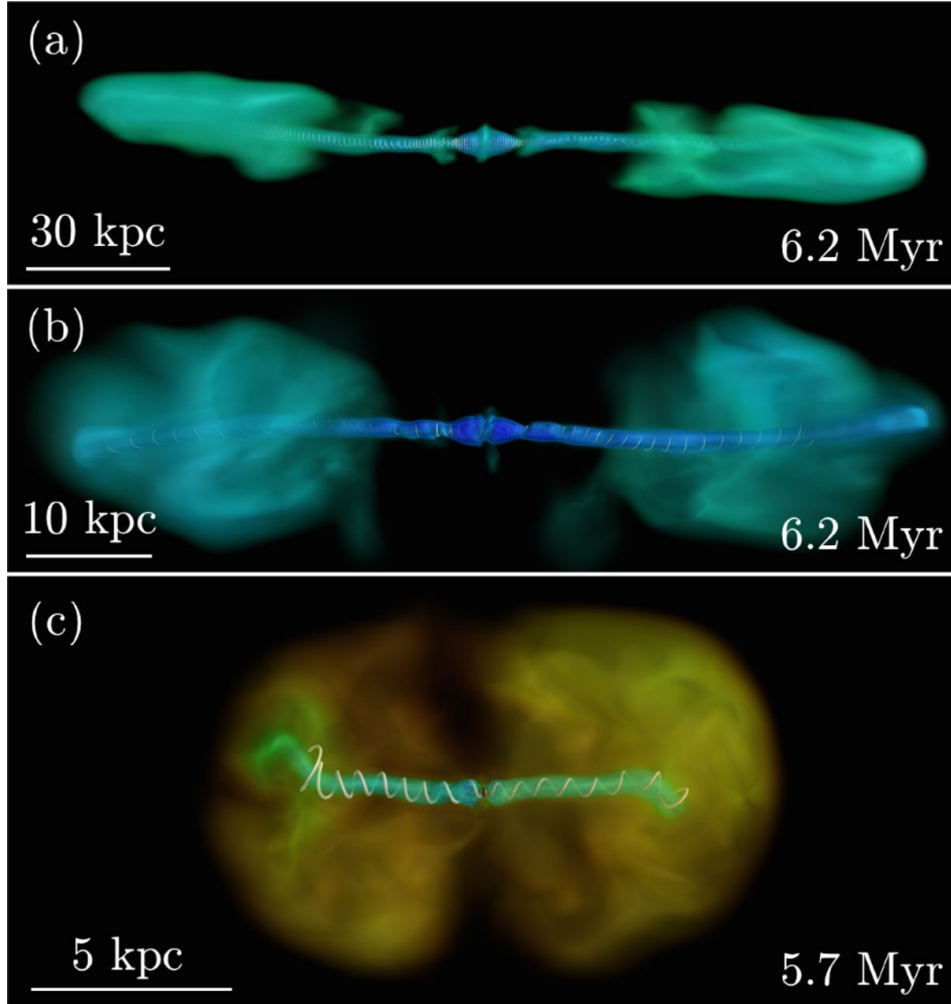


Figure 1.3.: 3D MHD simulations for powerful jets (Panels a and b) and low power jets (Panel c), respectively (Tchekhovskoy & Bromberg 2016). The color of the images represent the logarithm of the density with yellow-green being high and blue being low, the white lines show magnetic field lines.

1.2. NGC 1052 – Radio-centric view of a double-sided jet in the plane of the sky

The nearby giant elliptical galaxy (E 4) NGC 1052 hosts a low-luminous AGN whose super-massive black hole (SMBH) has a mass on the order of $M \simeq 1.55 \times 10^8 M_\odot$ (Woo & Urry 2002).

1. Introduction

The J2000 coordinates of this source are $02^{\text{h}}41^{\text{m}}04.7985^{\text{s}}$ in right ascension and $-8^{\circ}15'20.751''$ in declination (VLBA Calibrator Survey, [Beasley et al. \(2002\)](#)) and is located at a redshift of $z = 0.005037 \pm 0.000020$ ([Denicoló et al. 2005](#)). Independently of the cosmological redshift I will use the distance of $19.23 \pm 0.14 \text{ Mpc}$ ([Tully et al. 2013](#)) throughout this work, which has been derived based on surface brightness fluctuations. Estimating the distance of an object as close as NGC 1052 based on the recession velocity is risky as it is easily biased by peculiar velocities of the galaxy. This gives a linear scale of $0.093 \text{ pc mas}^{-1}$ and a proper motion of $\mu = 1 \text{ mas s}^{-1}$ corresponds to an apparent speed of $\beta = \mu/c = 0.3027$.

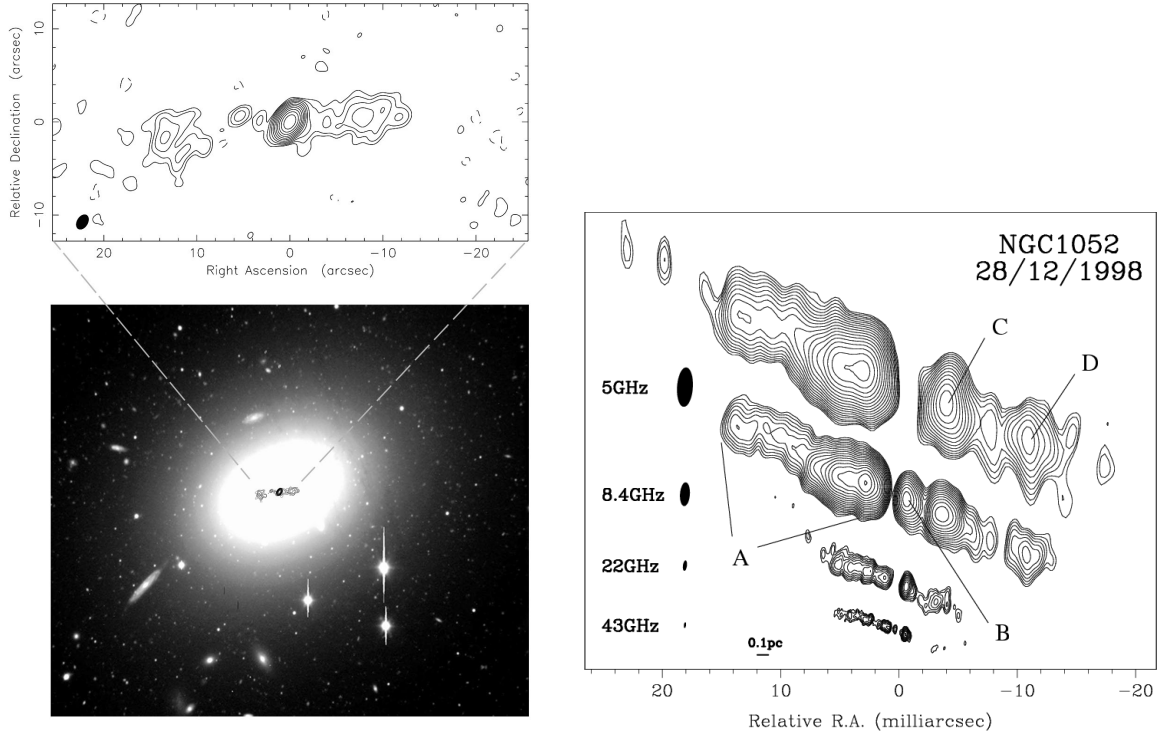


Figure 1.4.: NGC 1052 morphology (Left) The bottom panel shows an optical image of NGC 1052 observed with Keck at V-Band covering $5.6 \times 7.0 \text{ arcmin}$ ([Forbes et al. 2001](#)) with the large scale Radio CLEAN contour image observed with MERLIN at 1.4 GHz over-plotted, which are shown in more detail in the upper panel ([Kadler et al. 2004a](#)). (Right) CLEAN contour images at 5, 8.4, 22, and 43 GHz observed with the VLBA ([Kadler et al. 2004b](#)), revealing the small scale structures.

NGC 1052 had been observed over a wide frequency range. With a bolometric luminosity of $L_{\text{bol}} \sim 7 \times 10^{42} \text{ erg s}^{-1}$ and $\log(L_{\text{bol}}/L_{\text{edd}}) = -3.4$. NGC 1052 is close to the regime of Seyfert galaxies. However, based on its optical spectrum it had been classified as a low-ionization nuclear emission line region object (LINER) and is frequently used as reference to define this class ([Mayall 1939](#); [Fosbury et al. 1978](#); [Ho et al. 1997](#)). Observations in the mid-infrared with VLTI and MIDI show an unresolved nucleus $< 5 \text{ mas}$ in size. Based on these images [Fernández-Ontiveros et al. \(2019\)](#) favour a compact jet to be the origin of the near-infrared emission. A study of the spectral energy distribution (SED) over ten orders of

magnitude in frequency shows no big blue bump and infers the continuum emission to be of synchrotron origin [Reb et al. \(2018\)](#). Moreover, the observed continuum luminosity requires a high accretion power which may only be achieved by a thin accretion disc with an accretion rate of $\sim 7.3 \times 10^{-5} M_{\odot} \text{ yr}^{-1}$ truncated at a radius $r_{\text{tr}} \gtrsim 26 r_{\text{g}}$.

NGC 1052 shows a large scale radio structure of 3 kpc in size. A Very Large Array (VLA) image at 1.4 GHz reveals a double-sided jet structure at a position angle of 95° North to West, two radio lobes, and a dominating core region with about 85% of the total flux density ([Wrobel 1984](#)). High-angular resolution observations with very-long-baseline interferometry (VLBI) show a prominent parsec-scale double-sided jet structure at a position angle of around 70° oriented close to the plane of the sky at an inclination angle $> 70^{\circ}$ ([Kadler et al. 2004a](#); [Baczko et al. 2016a](#)). At centimeter wavelengths our view onto the central region is blocked by a geometrically thick structure perpendicular to the jets with an optical depth $\tau_{1 \text{ GHz}} \sim 300$ to 1000 and a column number density of 10^{22} cm^{-2} to 10^{24} cm^{-2} ([Kameno et al. 2001](#); [Sawada-Satoh et al. 2008](#)). It covers about $\sim 0.1 \text{ pc}$ towards the eastern, approaching jet and $\sim 0.7 \text{ pc}$ towards the western, receding jet. The free-free absorption in the torus results in an emission gap between both jets which becomes smaller towards higher frequencies (see [Fig. 1.4](#); [Kameno et al. \(2001\)](#); [Vermeulen et al. \(2003\)](#); [Kadler et al. \(2004a,b\)](#); [Brenneman et al. \(2009\)](#)). At 43 GHz almost no absorption is observable anymore, enabling us to peer through the absorbing structure. Individual features in both jets have been found to move with a mean apparent speed of $v/c = \beta \leq 0.23$ ([Vermeulen et al. 2003](#); [Böck 2012](#); [Lister et al. 2019](#)).

Several multi-frequency radio observations of NGC 1052 found H_2O maser emission which coincide with the surrounding torus ([Claussen et al. 1998](#); [Kameno et al. 2005](#); [Sawada-Satoh et al. 2008](#)). In addition, several absorption lines had been detected (HI, OH, HCO^+ , HCN, CO) (see e.g., [van Gorkom et al. 1986a](#); [Omar et al. 2002](#); [Liszt & Lucas 2004](#); [Impellizzeri et al. 2008](#); [Sawada-Satoh et al. 2016](#))).

A GMVA observation from October 2004 detected the twin-jets at this frequency for the first time (compare bottom of [Fig. 1.5](#), [Baczko et al. \(2016a\)](#)). Due to the low declination of NGC 1052 of -8° and the predominance of East-West baselines the synthesized beam is very elliptical and therefore, the central feature as well as the jets are transversally unresolved. The GMVA image reveal two faint plasma streams with a compact, unresolved feature in between, which has about 70% of the total flux density. It is interpreted as blended emission from both jet cores. Hence, the central engine is suspected to reside at its location. Assuming basic synchrotron theory, this sets boundaries to the strength of the magnetic field at $1 R_{\text{S}}$ as $200 \text{ G} < B < 8 \times 10^4 \text{ G}$ (compare [Fig. 1.5](#) upper panel).

1.3. Motivation of the herein presented work

Our understanding of active galactic nuclei (AGN) and their jets has improved largely since the first detections of emission-line nuclei in the beginning of the twentieth century. In the scope of the AGN unified scheme ([Antonucci 1993](#); [Urry & Padovani 1995](#)) peculiarities observed for different types of AGN can be explained, assuming intrinsic symmetry between jet and counter-jet. However, to understand the physics driving AGN jets it is crucial to address the

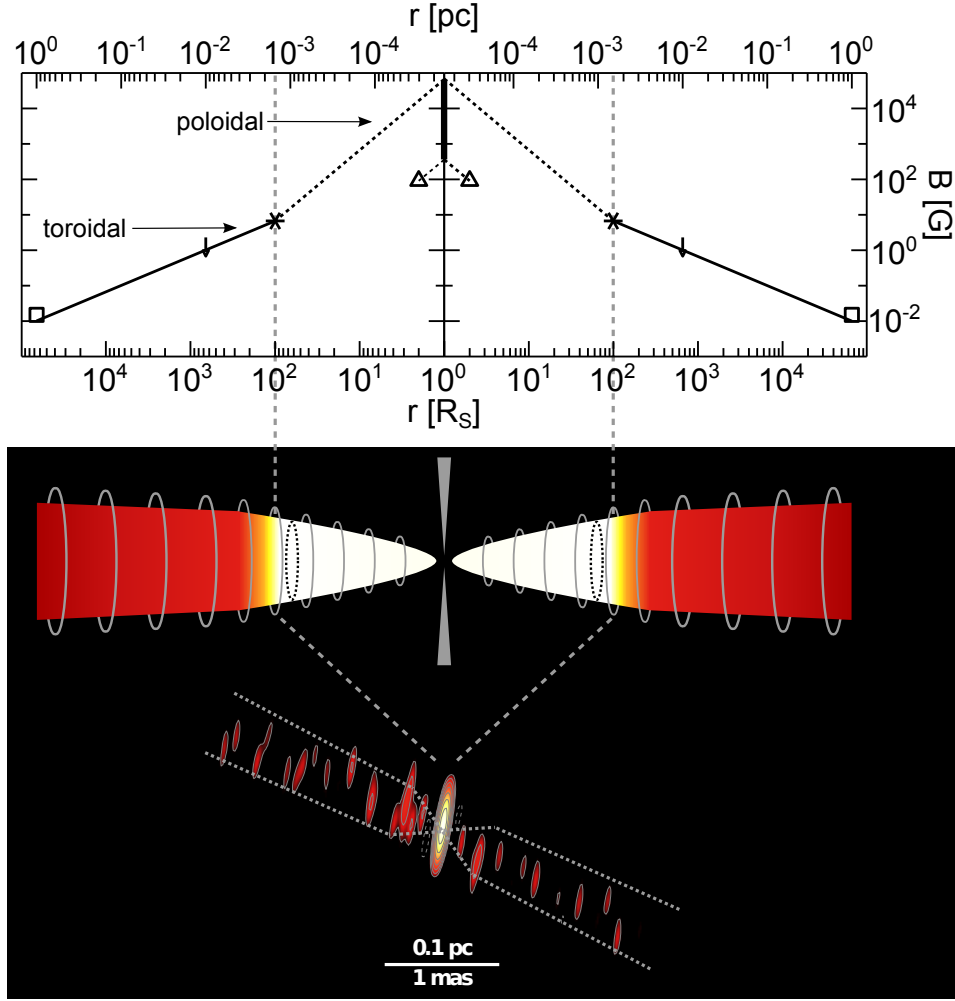


Figure 1.5.: (Top) Estimate of the magnetic field. Asterisk and triangle give the magnetic field derived from synchrotron cooling, based on the most conservative and the lowest possible size estimate of the central region, respectively. Assuming a change from toroidal to poloidal field configuration, the strength of the magnetic field is extrapolated inwards to $1 R_S$ and outwards to 1 pc. (Middle) Sketch of the jet-launching region. (Bottom) Naturally weighted image of NGC 1052 at 86 GHz (Baczko et al. 2016a).

nature of the central, powering region. For that the highest resolution, as achieved by mm-VLBI, is decisive. A big effort to image this region is made in the scope of the event horizon telescope (EHT), focusing on two main sources, Sgr A* and M 87. While Sgr A* does not reveal clear evidence for jets, M 87 is dominated by a kpc-scale jet emission.

Most studies on radio-loud AGN were conducted on blazars. Being largely affected by Doppler boosting, these only reveal one jet. It is difficult to investigate the innermost jet-forming region in this class of sources, especially it is impossible to study the symmetry-paradigm of AGN jets. There are only very few sources that can be used to derive physical properties that connect the central supermassive black hole and the jets. The linear scale has

to be small enough to reach the regions of jet formation. In addition the location of the central engine has to be known with high accuracy. One possibility is to focus on radio galaxies. The large inclination angle of their jets implies that Doppler boosting is nearly negligible and both jets are observable. However, this also means that radio galaxies are in general fainter, which is why mm-VLBI studies have been focused so far on very few well known objects.

Three of the radio galaxies in which tests for jet formation models could be performed through mm-VLBI are the nearby sources M 87, Cyg A, and 3C 84. The jet bases in M 87 and Cyg A were found to be prominently limb-brightened. Whereas the size of the M 87 jet base was derived to be $\sim 5 R_S$ at 86 GHz (Kim et al. 2018), Boccardi et al. (2016) found a minimum transverse width of $\sim (227 \pm 98) R_S$ in Cygnus A. These results suggest the existence of an outer jet sheath anchored to the accretion disc, more extended in Cygnus A than in M87. Several observations of 3C 84 show as well a limb-brightening structure with an almost cylindrical jet profile down to a few hundred gravitational radii (r_g) from the core (Giovannini et al. 2018; Kim et al. 2019). The jet has a wide opening angle similar to Cyg A. Based on RadioAstron observations at 22 GHz Giovannini et al. (2018) measured the transversal jet width of 3C 84 at a distance of $350 r_g$ to be $\gtrsim 250 r_g$.

NGC 1052 is another source in that row. It fulfills the requirements mentioned above. Given that the angle of the jets to the line of sight is close to 90° in the case of NGC 1052, the location of the central engine can directly be derived by addressing it from both sides. Observations with the GMVA have shown, that the jets can be detected at 86 GHz under favourable observational circumstances. It shows pronounced absorption effects due to the surrounding torus, enabling us to study the impact of a dense distribution of matter on the jets themselves as well as on the observed structure. Giving its close distance small linear scales can be tested to reach the area of jet formation with mm observations. Hence, within this thesis I will investigate the region of jet formation and collimation on the basis of multi-frequency and multi-epoch observations of NGC 1052.

2 | Theory

In this chapter I shortly introduce theoretical models and concepts which are needed throughout the herein presented work. The derivations in this chapter are mainly based on [Pacholczyk \(1970\)](#) and [Rybicki & Lightman \(1979\)](#) in terms of emission processes and [Burk & Graham-Smith \(2009\)](#) and [Taylor et al. \(1999\)](#) for basics of radio astronomy.

2.1. Synchrotron radiation

In this section I will shortly introduce the concept of synchrotron radiation and present mathematical concepts which will come in handy later in the description of the results and discussion. A deeper understanding can be found in (e.g., [Pacholczyk 1970](#)) or [Türler et al. \(1999\)](#).

As was shown in the previous chapter, AGN jets consist of charged particles accelerated in strong magnetic fields and moving at relativistic speeds. In the easiest case electrons can be assumed. These particles will describe a circular motion due to the Lorentz force, leading to an acceleration and hence Synchrotron radiation. Due to relativistic effects the radiation is beamed into a cone with opening angle γ^{-1} , where γ is the Lorentz factor of the electron $\gamma = (1 - \beta_e^2)^{-1/2}$. The spectrum of a single electron will peak at the critical frequency:

$$\nu_c = \frac{\gamma^2 e B}{2\pi m_e c}, \quad (2.1.1)$$

where m_e is the electron mass, c the speed of light, e the electron charge and B the magnetic field.

Assuming a random pitch angle distribution, the emitted power for an electron is:

$$P = \frac{4}{3} c \sigma_T U_B \beta^2 \gamma^2, \quad (2.1.2)$$

where γ is the Lorentz factor and β the ratio of the speed of the radiating electrons to the speed of light, σ_T the Thomson cross section, and $U_B = B^2/8\pi$ the energy density of the magnetic field.

The energy loss of the electron can further be expressed as the change of its Lorentz factor:

$$\left(\frac{d\gamma}{dt} \right) = -\frac{4}{3} \sigma_T \frac{u_B}{m_e \cdot c} \gamma^2 \beta^2. \quad (2.1.3)$$

By integration of this equation, the synchrotron cooling can be derived. It depends on the

energy and radiation rate of the electron for a given Lorentz factor.

$$t_c = \frac{3}{4} \frac{m_e c}{\gamma \sigma_T U_B \beta^2} \approx \frac{25}{B^2 \gamma} \text{yr}. \quad (2.1.4)$$

A result of this equation is that the lifetime of the electron strongly depends on its energy and on the magnetic field strength. For a strong magnetic field and high electron energy the lifetime is much shorter than for a relatively low magnetic field. Therefore, cooling is faster at higher energies resulting in a steep spectrum.

We can assume a power law distribution of electrons, $N(E) = K E^{-s}$, where s is the spectral slope and K the normalization coefficient. The superposition of the particle distribution results in a power-law spectrum $S_\nu \propto \nu^{+\alpha}$ with the optically thin spectral index $\alpha_{\text{thin}} = -(s-1)/2$ and the optically thick spectral index $\alpha_{\text{thick}} = 2.5$. The spectrum shows a turnover frequency ν_m at the transition from the optically thin to the optically thick regime. At ν_m the opacity of the synchrotron radiation is $\tau(\nu_m) = 1$. At high frequencies the spectrum is optically thin. Below the turn-over frequency *synchrotron self-absorption* (SSA) takes place and one expects a dependence of $S_\nu \propto \nu^{5/2}$.

The whole spectrum can be described including both, the optical thick and the optical thin part (Türler et al. 1999):

$$S_\nu = S_m \left(\frac{\nu}{\nu_m} \right)^{\alpha_{\text{thick}}} \frac{1 - \exp(-\tau_m (\nu/\nu_m)^{\alpha_{\text{thin}} - \alpha_{\text{thick}}})}{1 - \exp(-\tau_m)}, \quad (2.1.5)$$

where $\tau_m = 3/2 \left(\sqrt{1 - \frac{8\alpha_{\text{thin}}}{3\alpha_{\text{thick}}}} - 1 \right)$ is the optical depth and S_m the flux density at the turnover. An example spectrum is shown in Fig. 2.1.

However, numerical simulations as well as observations draw a more complex spectrum that is not easily describable by a power law, but shows several breakpoints and cutoffs.

2.2. Brightness temperature

A term commonly used in radio astronomy is the so called brightness temperature T_b . It is a hypothetical temperature a source with a specific intensity I_ν would have assuming black-body radiation. Therefore it can be derived from the Planck formula:

$$u_\nu d\nu = \frac{2h\nu^3}{c^2} \frac{1}{e^{h\nu/k_B T} - 1} d\nu, \quad (2.2.1)$$

where u_ν is the power per unit area per unit frequency interval and h the Planck constant. At radio wavelengths the Rayleigh-Jeans approximation can be assumed, leading to:

$$I_\nu(T) = \frac{2\nu^2}{c^2} k_B T. \quad (2.2.2)$$

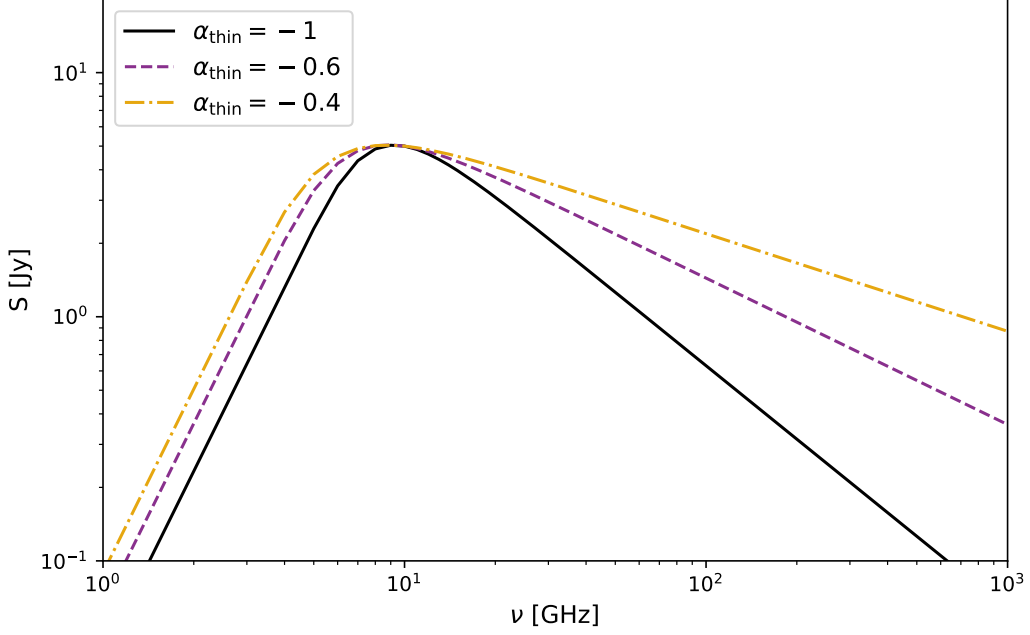


Figure 2.1.: Synchrotron spectrum assuming the turnover at $\nu_m = 10$ GHz, $S_\nu = 5$ Jy and three different values for the optically thin spectral index as noted in the figure legend. The optically thick spectral index is assumed to be $\alpha_{\text{thick}} = 2.5$

Using $I_\nu = S_\nu / \Omega$ with the flux density S_ν and the solid angle of the source Ω it follows for the brightness temperature:

$$T_b = \frac{\lambda^2}{2k_B} \frac{S_\nu}{\Omega}. \quad (2.2.3)$$

Following e.g., [Kovalev et al. \(2005\)](#) it can be defined as

$$T_b = \frac{2 \ln 2}{\pi k_b} \frac{S_{\text{tot}} \lambda^2 (1+z)}{\theta_{\text{FWHM}}^2}, \quad (2.2.4)$$

where S_{core} is the total flux density, z is the redshift, and θ_{FWHM} is the full-width-half maximum (FWHM) of a circular Gaussian parametrising the emission.

Obviously the radiation from AGN jets cannot be assumed to be of thermal nature, still the concept of temperatures is commonly applied. Typical values for the cores of AGN on milli-arcsecond scales are of the order $T_B \sim 10^{10} - 10^{12}$ K (see e.g., [Kovalev et al. 2005](#)) and even exceeding 10^{13} K from space-based observations (see e.g., [Kovalev et al. 2016](#)).

2.3. Relativistic effects in AGN

2.3.1. Beaming and superluminal motion

The outflows that can be observed in extragalactic jets are moving at relativistic speeds. That leads to the conclusion that the orientation of the jet to the line of sight has an effect on the apparent motion. The further the viewing angle is away from 90 degrees, the faster the jet appears to move.

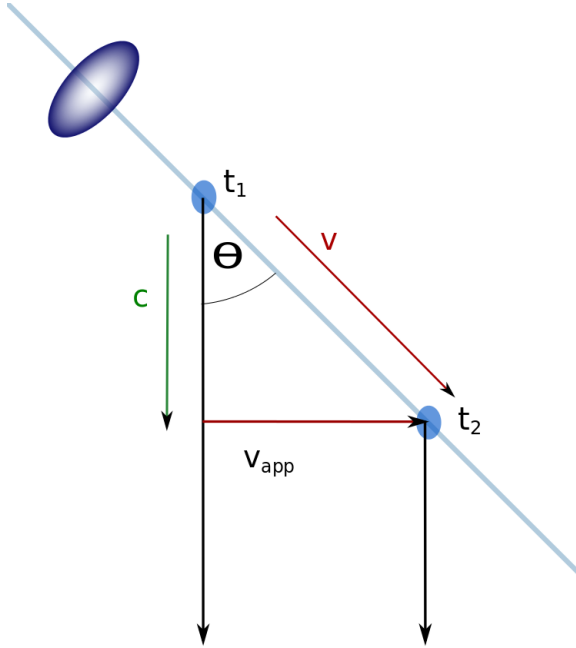


Figure 2.2: Superluminal motion: Seen is a *blob* travelling at speed v close to c , that emits light in instants t_1 and t_2 . Due to the small angle to the line of sight apparent speeds faster than c are observed.

This has basically two effects. The first one due to relativistic motion is shown in Fig. 2.2 and is called *superluminal motion*. The outmoving material, seen in regions of enhanced emission, defined as features in the jet, *blobs* or *components*, travel with the velocity v . Due to the inclination angle θ the apparent velocity v_{app} (in that case that of the proceeding jet) gets higher as:

$$v_{\text{app}} = \frac{\Delta s}{\Delta t} = \frac{v \sin \theta}{1 - \beta \cos \theta}. \quad (2.3.1)$$

The second effect is the so called *relativistic boosting*. As an emitting particle travels at relativistic speeds its emission gets boosted into the direction of movement. Additionally to that its frequency gets shifted due to Doppler boosting.

The observed frequency can be derived by applying a Lorentz transformation to the first component of the wave factor k , as seen in Eq. 2.3.2

$$k_{\text{em}}^{(0)} = \gamma \left(k_{\text{obs}}^{(0)} - \frac{v}{c} k_{\text{obs}}^{(1)} \right), \quad (2.3.2)$$

where $\gamma = (1 - \beta^2)^{-1/2}$.

2. Theory

Substituting $k^{(0)} = \omega/c$ and $k_{\text{obs}}^{(1)} = \cos(\theta) \omega_{\text{obs}}/c$, the observed frequency can be expressed in terms of the emitting frequency ν_{em} , its viewing angle θ and velocity relative to the observer in units of speed of light $\beta = v/c$:

$$\nu_{\text{obs}} = \nu_{\text{em}} \frac{\sqrt{1 - \beta^2}}{(1 - \beta \cos \theta)}. \quad (2.3.3)$$

Based on Eq. 2.3.3 the Doppler factor is defined as

$$D = \frac{\nu_{\text{obs}}}{\nu_{\text{em}}} = \frac{1}{\gamma(1 - \beta \cos \theta)}. \quad (2.3.4)$$

The spectrum can be approximated by a power law. In Eq. 2.3.5 the spectral index α defined through $S_\nu \propto \nu^\alpha$ was used. Finally we can use the Lorentz invariance of the flux density $S_\nu \propto \nu^{-3}$ to compare the flux densities of the approaching and the receding jet, called counter jet:

$$S(\nu_{\text{obs}}) = D^{3-\alpha} S(\nu_{\text{em}}). \quad (2.3.5)$$

For the case of a continuous jet the factor gets $2 - \alpha$. These equations show that the observed flux density depends on the angle to the line of sight of the jet. The smaller the angle θ the larger becomes the Doppler factor and with that the difference between emitted and observed flux density. As the intensity of the approaching jet increases, that of the receding one decreases and in the extreme case only one jet can be observed.

An estimate on the angle of the jets to the line of sight θ_{LOS} can be derived from their flux-density ratio. Assuming that both jets are intrinsically symmetric and evolve with an angle of 180° between the two jet axes, i.e.,

$$R = \frac{S_{\text{approaching}}}{S_{\text{receding}}} = \left(\frac{1 + \beta \cos \theta_{\text{LOS}}}{1 - \beta \cos \theta_{\text{LOS}}} \right)^{2-\alpha}. \quad (2.3.6)$$

In this case, β is the intrinsic jet speed and α the spectral index. A value of $\alpha = -1$ is adopted for the optically thin spectral index (see Fig. 2.1).

In addition, the angle of both jets to the line of sight can be derived with knowledge of their intrinsic (β) and apparent (β_{app}) speeds for approaching and receding jets as follows:

$$\beta_{\text{app,approaching/receding}} = \frac{\beta \sin \theta_{\text{LOS}}}{1 \mp \beta \cos \theta_{\text{LOS}}}. \quad (2.3.7)$$

Both equations can be combined to derive the allowed parameter space for the intrinsic velocity β and the angle of the jets to the line of sight θ_{LOS} by using measurements of the velocity and flux density ratio in a jet.

2.4. Very Long Baseline Interferometry

In this section I give a short introduction on the basics of radio interferometry and the peculiarities which need to be taken into account during data reduction. This section is based on standard literature as [Burk & Graham-Smith \(2009\)](#); [Wilson et al. \(2009\)](#); [Thompson et al. \(2017\)](#), and selected lectures summarized in [Taylor et al. \(1999\)](#).

Radio astronomy started with the discovery of extraterrestrial radio emission by [Jansky \(1933\)](#). With the exception of optical astronomy, radiation at radio wavelengths is the only other frequency window that penetrates the earth atmosphere without being largely affected. Figure 2.3 visualizes the atmospheric opacity depending on the observed wavelength. This fact enables us to build large radio telescopes on ground. Present telescope receivers are able

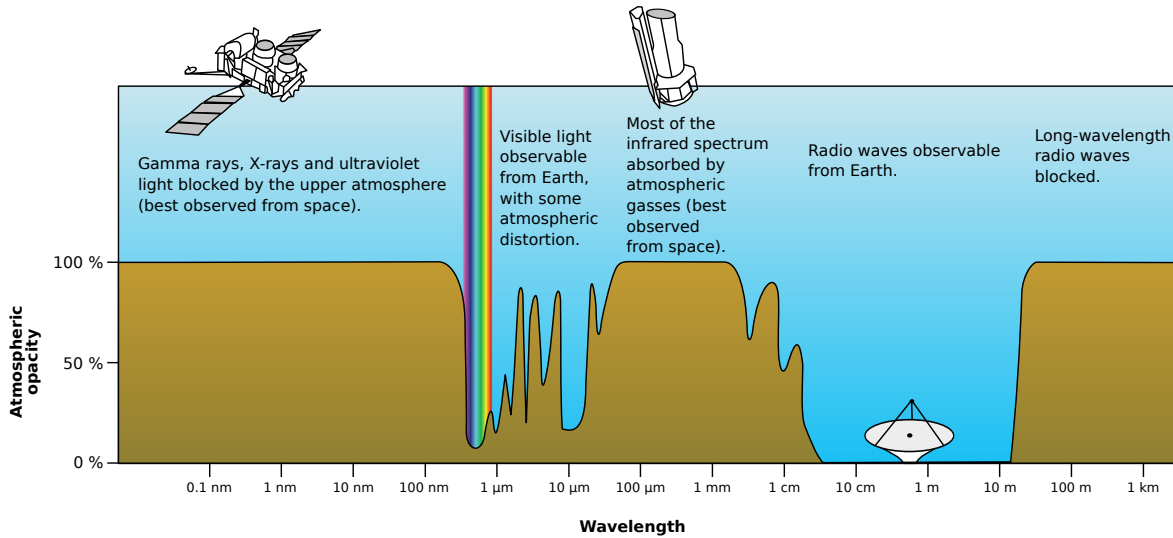


Figure 2.3.: Atmospheric opacity depending on observed wavelengths of radiation (Copyright NASA).

to observe over a wide band of radio frequencies, from a few MHz up to several hundreds of GHz. But there are a few limitations to what is observable from ground. At frequencies below 20 MHz (about 15 m) the emission gets reflected by the ionosphere, whereas above 30 GHz (about 1 cm) there are several absorption processes within the atmosphere. In addition, the atmosphere starts to be a radio emitter itself at higher frequencies. An example is the water vapor line at 22 GHz. The difficulties of high-frequency observations are overcome by building telescopes at high altitudes as for example the Atacama Large Millimeter/submillimeter Array (ALMA), located at 5 km above sea level in the Atacama Desert in Chile. An additional problem is human-made: our technology uses many devices, which are strong radio emitters. This results in so-called *radio frequency interference* (RFI), an additional noise term with a high intensity compared to weak signals from astronomical objects. To enable radio observations there are protected frequency bands dedicated to radio astronomy in which it is generally prohibited to transmit.

Another milestone in radio astronomy was the development of aperture synthesis ([Ryle & Hewish 1960](#)). For their pioneering research in radio-astronomy Martin Ryle and Antony

Hewish have been awarded with the Nobel prize in 1974. Through this technique it is possible to connect individual radio telescopes in order to enlarge the aperture beyond the dish diameter up to the size of the Earth with the technique of very long baseline interferometry (VLBI) and even beyond by the addition of space based telescopes.

Michelson interferometry is a way to overcome the resolution limit of a single radio telescope. Resolution of an optical interferometer is described by the Rayleigh criterion as $\sin \theta \propto \frac{\lambda}{D}$, with the resolution θ , the wavelength λ and the aperture diameter D . With respect to other observing windows, as optical or X-ray, radio emission has long wavelengths resulting in a lower resolution of radio telescopes. Hence, to obtain angular resolutions comparable to higher frequency wavebands, larger dishes are needed. For example a human eye which is sensitive for optical light has a resolution of $1'$ if assuming a size of the pupil of 2 mm. To obtain the same resolution at a radio wavelength of 4 cm a dish of 140 m has to be build, which is even larger than the Effelsberg telescope. But there is a limit to what is possible to construct. The larger the dish of the telescope gets, the more difficult it is to obtain a nearly perfectly smooth surface, which is crucial to gain high sensitivity. The largest radio telescope up to now is FAST with a dish diameter of 500 m, and an illuminated aperture of 300 m, located in China. It is not possible to build steerable telescopes that size. Therefore, to observe different regions of the sky, the receiver cabin has to be moved accordingly. However, depending on the pointing distance from the zenith the effective illuminated area of the telescope shrinks and it is not possible to cover an area of the sky as large as with a steerable telescope.

2.4.1. Measuring radio signals

Radio telescopes directly measure the electromagnetic radiation field. In the most simple case of long wavelengths this is done by a dipole antenna. For example the Low Frequency Array (LOFAR) observes the low-frequency band with an array of dipole antennas. To increase the sensitivity at higher frequencies, large parabolic dishes are build, which focus the emission onto the so called *feed horn*. It acts as waveguide to the receiver in which the signal is further processed and is typically build in a way to detect both polarizations of the radiation field. The feed horn is the first component of the telescope acting as frequency filter, depending on its form and length. An example picture showing two waveguides located in the primary focus of a VLA antenna is shown in Fig. 2.4.

As astronomical radio signals are very weak an amplification is required. In addition down-converting to an intermediate frequency is done (IF, 150 – 400 MHz). This ensures that all further processing of the original signal does not interfere with the incoming astronomical radio signal. In addition, by sticking to a standard IF for different receivers the same electronic devices can be used in the back end for further processing of the signal.

2.4.2. The basics of radio interferometry

As mentioned earlier, there is a limit on the size of a radio telescope. This can be overcome by using a Michelson interferometer with antennas as interferometric elements. Namely, with a technique called radio interferometry, in which a synthesised aperture is build up out of a



Figure 2.4.: A picture of two waveguides horn feeds connected to the receiver in the primary focus of a VLA antenna.

number of individual telescopes, forming in the case of VLBI a telescope up to the size of the earth.

The theoretical construct behind radio interferometry is the so called van Citter-Zernike theorem ([van Cittert 1934](#); [Zernike 1938](#)), that applies to any source that is spatially incoherent. It can be shortly described as: *The spatial autocorrelation function is equal to the Fourier-transformation of the source brightness distribution*. Hence, by measuring the spatial correlation function, the brightness distribution of an astronomical source can be reconstructed.

An interferometer measures the complex visibility function $V_V(\mathbf{b})$ ¹, which is linked to the true brightness distribution $I_V(\mathbf{s})$, integrated over the solid angle $d\Omega$ of the source, for a given frequency via a Fourier transformation:

$$V_V(\mathbf{b}) = \iint I_V(\mathbf{s}) e^{-2\pi i \mathbf{v} \mathbf{b} \mathbf{s} / c} d\Omega, \quad (2.4.1)$$

with the baseline vector \mathbf{b} , the unit vector \mathbf{s} pointing towards the source and \mathbf{s}_0 towards the phase tracking center within the source. The signal at the second telescope is delayed by the geometrical time delay $\tau_g = \mathbf{b} \cdot \mathbf{s} / c$.

A radio interferometer is typically built up by several telescopes, for example, the dedicated Very Long Baseline Array (VLBA) in the USA consists out of ten 25 m telescopes. A convenient way of expressing the baseline vectors for all possible combination of antennas is to place them in a coordinate system (u, v, w) measured in wavelengths, with $\mathbf{w} = \mathbf{s}_0$. The uv -plane is always perpendicular to the source direction. In this coordinate system the source

¹bold face denotes a vector

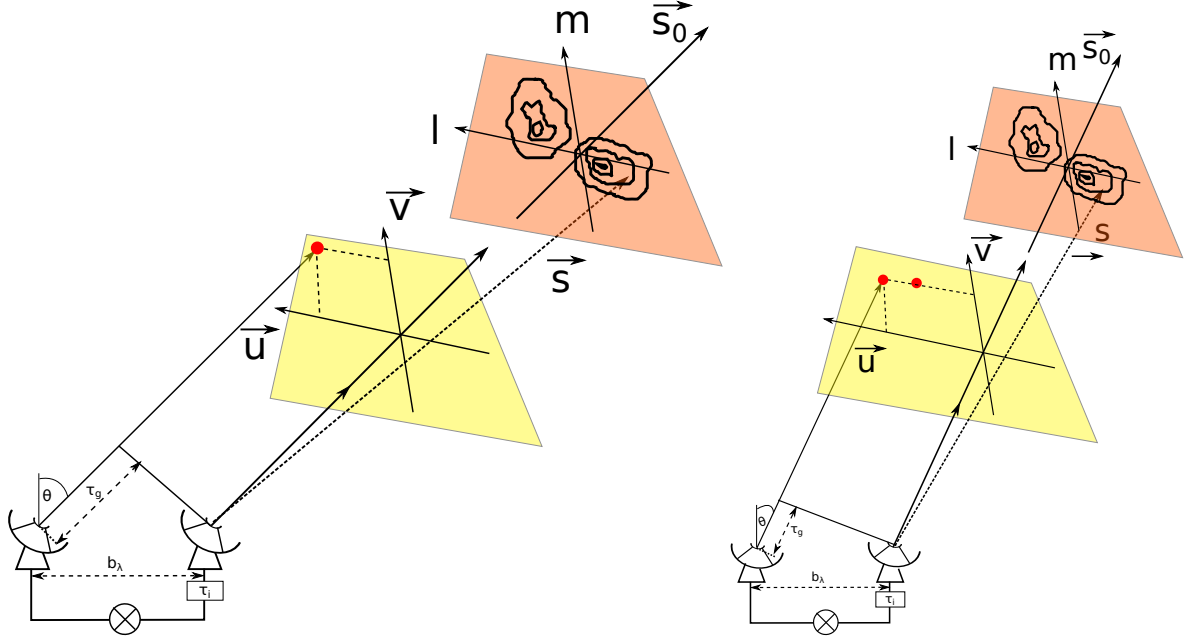


Figure 2.5.: A sketch of a basic two-element interferometer at time t_1 (left) and t_2 (right). The source brightness distribution, which spans in the lm -plane, is connected to the visibility measured in the uv -plane. As the earth moves, the uv -plane is filled (red dots).

brightness distribution is measured in the (l, m, n) plane, which are the direction cosines of \vec{s} , which leads to $d\Omega = dl \, dm / \sqrt{1 - l^2 - m^2}$. The connection between a two-element interferometer (one baseline), the source, and both planes is sketched in Fig 2.5. Typically the equation can be simplified by assuming $w \equiv 0$, resulting in:

$$V_V(u, v, w = 0) = \iint \frac{I_V(l, m)}{\sqrt{1 - l^2 - m^2}} e^{-2\pi i(ul + vm)} dl \, dm . \quad (2.4.2)$$

The visibility function is the complex representation of the correlator output, which is a multiplication, followed by averaging of the power output at both telescopes of one baseline. For the most simple case of a monochromatic point source the cross-correlation of both signals is equal to:

$$r_{ij} = v_i v_j \cos(2\pi \nu \tau_g) , \quad (2.4.3)$$

where v_i/v_j are the voltages at both telescopes. This equation represents the interferometer *fringe pattern*, with the fringe amplitude $v_i v_j$. The definition of fringes in radio interferometry is oriented on the description from optics regarding a Michelson interferometer. The correlator output can be related to the visibility as:

$$dr = A_0 |V| \cos(2\pi \nu \tau_g - \phi_V) d\nu , \quad (2.4.4)$$

with the response at the beam center A_0 and the complex visibility defined as $V \equiv |V| \exp(i\phi_V)$.

In reality measurements are not perfect. There are several things to consider, for example the finite bandwidth $\Delta\nu$. This results in the so called *bandwidth smearing* when averaging over a larger bandwidth. It leads to a modulation of the fringe pattern by a *sinc* function as $\text{sinc}(\pi\Delta\nu\tau_g)$ and therefore reduces the response of the interferometer, if $\tau_g \neq 0$. A larger geometric delay will thus result in a stronger smearing. Even under perfect circumstances the smearing will have a large effect on extended source structure far away from the source center, as the delay is only corrected for the phase tracking center. A large bandwidth will increase the sensitivity of the telescope, but enlarges the bandwidth smearing. To overcome this problem, the band is typically divided into several sub-bands, which are averaged individually.

In the ideal case the interferometer covers the whole uv -plane and hence the source brightness distribution can be reconstructed perfectly by inverse Fourier transformation. However, the so called uv -coverage will be sparse as there is only a finite number of baselines and time for observation. This leads to the need to introduce a sampling function $S(u, v) = \sum_k \delta(u - u_k, v - v_k)$, being 1 only where data is taken. Eq. 2.4.2 can be simplified in case of a parabolic antenna with a small primary beam, that leads to $\sqrt{1 - l^2 - m^2} \approx 1$. Adding the modification given by $S(u, v)$ this leads to the so called *dirty image*:

$$I_V^D(l, m) = \iint S(u, v) V_V(u, v) e^{2\pi i(ul+vm)} du dv. \quad (2.4.5)$$

The *dirty image* is the convolution of the *true brightness distribution* I_V with the *synthesized beam* or *dirty beam*, that is:

$$B(l, m) = \iint S(u, v) e^{2\pi i(ul+vm)} du dv. \quad (2.4.6)$$

2.4.3. VLBI calibration

After correlation the visibilities need to be corrected for several effects, namely, inaccurate positions, corruptions through the atmosphere, or differences in the electronic systems which had not been accounted for. Therefore, the measured visibility \tilde{V} is not equal to the true visibility V . This requires a set of calibration routines after the correlation stage. The relationship between both visibilities can be described as:

$$\tilde{V}_{ij}(t) = G_{ij}(t) V_{ij}(t) + \varepsilon_{ij}(t) + \eta_{ij}(t), \quad (2.4.7)$$

with the observation time t , the baseline-based complex gain $G_{ij}(t)$, the baseline-based complex offset $\varepsilon_{ij}(t)$, and the stochastic complex noise $\eta_{ij}(t)$.

The main aim of calibration is to correct for the complex gain. Luckily, it can be assumed that most errors are antenna based, and hence the baseline-based complex gain can be derived by the complex gains of the antenna assuming $G_{ij}(t) V_{ij}(t) = g_i(t) g_j^*(t)$.

Focusing on the correlated phase, all possible errors can be summarized as:

$$\phi_{\text{corr}} = \phi_V(t, \nu) + \phi_{\text{inst}}(t, \nu) + \phi_{\text{geom}}(t, \nu) + \phi_{\text{atm}}(t, \nu) + \phi_{\text{iono}}(t, \nu). \quad (2.4.8)$$

ϕ_V is the true visibility phase, ϕ_{inst} the sum of all residual instrumental phase errors, ϕ_{geom} the residual error due to imperfect calculation of source and antenna position, and ϕ_{atm} and ϕ_{iono} are the residual errors due to different path length of the signal in atmosphere and ionosphere at the single antennas.

To correct for all these error terms the correlated data will pass a whole series of single correcting algorithms. The corrections that must be applied depend on the observational task. For example it depends on the observed frequency whether the different constituents of the atmosphere have a big impact on the correlated visibility phase or amplitude.

At present there are two main programs to calibrate interferometric radio data: 1) the Astronomical Imaging Processing System (AIPS, Greisen (1990)) and 2) CASA. The latter is still under development and not all procedures needed for calibration are yet present. Hence, the standard program for calibrating VLBI data is AIPS. In the following I will shortly describe the main procedures required to obtain a sufficiently calibrated data set.

Fringe-Fitting

Following Cotton (1995) there is a time dependent relationship between interferometer phase $\phi_{t,v}$ and the delay:

$$\phi_{t,v} = 2\pi\nu\tau_t. \quad (2.4.9)$$

As mentioned earlier the phase of the correlator output is only corrected for the delay tracking center, resulting in an residual delay term for the extended source structure. In addition the models assumed during correlation may not be perfect or do not assume peculiarities of individual telescopes. To estimate the error terms affecting the phase a technique called *fringe-fitting* is commonly applied, which solves for residual phase slopes in frequency and time. Differentiating and estimating the first order expansion of this equation leads to

$$\Delta\phi_{v,t} = \phi_0 + \left(\frac{\partial\phi}{\partial\nu}\Delta\nu + \frac{\partial\phi}{\partial t}\Delta t \right), \quad (2.4.10)$$

with the phase error ϕ_0 at the reference time and frequency, the delay $\frac{\partial\phi}{\partial\nu}$ and the rate or delay rate $\frac{\partial\phi}{\partial t}$. Once delay and rate are derived, their values can be subtracted from the visibility and the phase will be flattened over the frequency band.

As described in more detail in Cotton (1995), there exist several algorithms for fringe fitting, whereas most algorithms make use of the fast Fourier-transformation (FFT). Typically there are two stages of fringe fitting: 1) solving for the so called *instrumental delay* over frequency, which introduces phase offsets between sub-bands and 2) applying a *global fringe fit* to solve for any time dependent delay and rate residuals as well as for the fringe phase for the whole observation. For both steps, commonly antenna-based corrections are derived with respect to a single reference antenna. A more deep explanation of the individual procedures can be found in the AIPS *cookbook*².

²<http://www.aips.nrao.edu/cook.html>

2.4.4. Amplitude calibration

The visibility amplitude after the correlation is in units of cross-correlation coefficients. Hence, one task of the amplitude calibration is to convert these into the observed flux density S_v (energy per units of surface and frequency, normally expressed in Jansky, $1 \text{ Jy} = 10^{-23} \frac{\text{erg}}{\text{cm}^2 \text{sHz}}$). This is achieved by using the system equivalent flux densities (SEFD) for both antennas:

$$\text{SEFD} = \frac{2k_B T_{\text{sys}}}{A_{\text{eff}}}, \quad (2.4.11)$$

where A_{eff} is the effective area of the antenna and T_{sys} the *system temperature*, which is equivalent to the noise power in the receiving system. It includes not only the signal of the source T_A , also called *antenna temperature*, but in addition instrumental and atmospheric noise.

The flux density of the source is connected to the antenna temperature as:

$$S_v = \frac{2k_B T_A}{A_{\text{eff}}}. \quad (2.4.12)$$

Combining both equations, a conversion factor from Kelvin to Jansky for a baseline $i - j$ can be derived as:

$$S_{ij}^{\text{Jy}} = \frac{S^x}{y} \frac{\sqrt{\text{SEFD}_i \cdot \text{SEFD}_j}}{2\Delta\nu \Delta\tau}, \quad (2.4.13)$$

where y is a constant correcting for data loss due to digital sampling, $\Delta\nu$ is the bandwidth, and $\Delta\tau$ is the integration time. The antenna related values for T_{sys} and A_{eff} either are delivered together with the correlated data in table or text format.

At high frequencies an additional correction has to be applied, accounting for the atmosphere opacity. The opacity is the integral over the atmospheric absorption coefficient α_{abs} over the height h above the observer.

$$\tau_v = \int_0^\infty \alpha_{\text{abs}}(\nu, h) dh \quad (2.4.14)$$

(see e.g., [Thompson et al. 2017](#)).

To correct for opacity the average temperature of the atmosphere T_{atm} , the receiver noise T_{rec} , and the uncorrected system temperature T_{sys} have to be measured at each station.

$$\tau = \log \left(1 - \frac{T_{\text{sys}} - T_{\text{rec}}}{T_{\text{atm}}} \right). \quad (2.4.15)$$

There are other corrections needed depending on the specific observation. For example, the signal-to-noise ratio (snr) may be improved significantly by fitting a bandpass to the visibility amplitude to filter out instrumental amplitude inaccuracies over the frequency band that are not related to the source.

A detailed description of the calibration process in AIPS for the data discussed in this thesis is given in the respective chapters.

2.4.5. Imaging

After amplitude and phase calibration of the data in AIPS the corrected visibility can be *imaged* to produce a map of the source structure. The aim of imaging is to obtain a map of the brightness distribution of the source. A number of programs is designed to produce a source image, as AIPS, DIFMAP, CASA or more recently EHTIM (Chael et al. 2016, 2018). I will focus on DIFMAP as it was used to produce all maps presented in this thesis.

As was shown in the previous section, the source brightness distribution is connected to the visibility via a Fourier transformation. Hence, the first step of imaging is an inverse Fourier transformation. This returns not the *true brightness distribution* but the *dirty images* as presented in Eq. 2.4.5, which is the convolution of the true brightness distribution I_v with the synthesized beam $B(l, m)$ (see Eq. 2.4.6). The dirty beam is the Fourier transformation of the sampling function, hence is directly affected by the uv -coverage. Therefore, it can be slightly adjusted by introducing a weighting function of the data points. The most used extreme kinds are the *natural weighting*, where all data points have the same weight and therefore the best signal to noise ratio can be reached, and *uniform weighting* that weights $\propto 1/N(k)$ where $N(k)$ is the number of points in a specified area around the k^{th} data point. This results in less weighting of the points near $u = v = 0$. In the second case the highest resolution is reached.

CLEAN – A deconvolution method

The next step is to get rid of the dirty beam by reconstructing the true brightness distribution. This requires a deconvolution algorithm. The most commonly used deconvolution algorithm is CLEAN (Högbom 1974). The basic concept is to fit a smooth distribution of delta-like components (called CLEAN components) to the dirty map to build up a model of the source. From the *dirty beam* a *restoring beam* or *clean beam* is constructed, by fitting a Gaussian to the *dirty beam*, which reproduces the resolution of the image. By multiplying the source model with the restoring beam, the so called *CLEAN image* is obtained. By subtracting the restored model from the dirty image, the *residual map* is derived, showing any sparse emission that may not be modelled correctly. In reality building up a source model is tricky as the dirty image may contain several spurious structures due to gaps in the uv -coverage or errors in the visibility phase. To overcome this problem *cleaning* is typically done in an iterative way:

- 1) Select a rectangle called *clean box* in the dirty map where you trust emission to reside
- 2) Fit one CLEAN component to the peak only inside the clean box
- 3) Subtract the multiplication of the clean component with the clean beam from the dirty map
- 4) Fit the next clean component to the now obtained residual map and subtract the new model consisting now of two components.
- 5) Repeat steps 1 to 4 until no significant emission is left, defined by an individually set noise level
- 6) Define a second clean box and again repeat the steps until a satisfactory model is obtained and no significant emission is found in the residual map.

This process is highly depending on personal experience and therefore should be followed with care.

Self-calibration – Dealing with residual errors

The final CLEAN map will still not represent the best image possible to obtain. Even though a-priori amplitude and phase calibration was done, there are likely residual errors still in the data. There are several ways to remove these. In DIFMAP the method of *self calibration* is applied (see e.g., [Cornwell & Fomalont 1999](#)). Using the predicted model obtained by deconvolution, the complex gains (compare Eq. 2.4.7) are solved for and the visibility is corrected accordingly.

Assuming the source does not change over time additional constraints on the true visibility can be obtained by including so called *closure quantities* in the process of self-calibration.

The closure phase is the sum of the visibility phase around a closed loop of three baselines, which does not suffer from antenna-based errors. Assuming $\phi_{ij} = \mathbf{b}_{ij} \times \mathbf{s} + \boldsymbol{\psi}_{ij} + \phi_i - \phi_j$ \mathbf{b}_{ij} : baseline vector $\boldsymbol{\psi}_{ij}$: true visibility phase (vectors are set in boldface). Therefore, the sum of three phases in a closed triangle

$$\phi_{123} = \phi_{12} + \phi_{23} + \phi_{31} = \boldsymbol{\psi}_{12} + \boldsymbol{\psi}_{23} + \boldsymbol{\psi}_{31} . \quad (2.4.16)$$

There is a similar idea for the amplitude, called *closure amplitude* based on four antennas, which is defined as:

$$A_{1234} = \frac{|\tilde{V}_{12}| |\tilde{V}_{34}|}{|\tilde{V}_{13}| |\tilde{V}_{24}|} = \frac{|V_{12}| |V_{34}|}{|V_{13}| |V_{24}|} . \quad (2.4.17)$$

For the closure quantities, antenna based errors cancel out. Hence, they add crucial information about the true visibility phase and amplitude and are therefore used as additional information during self-calibration.

Recently there are several developments regarding VLBI imaging. For example it is possible to image a source by directly using only closure quantities in the EHTIM package ([Chael et al. 2016, 2018](#))

3 | Study of the asymmetry in the jet formation in NGC 1052

This chapter is partially published in Astronomy and Astrophysics (Baczko et al. 2019, reproduced with permission ©ESO). The results presented are based on images and model-fits, which are described in more detail in Baczko (2015).

In this chapter I study the morphology and evolution of the twin-jet in NGC 1052 over a period of four years. NGC 1052 was observed with the VLBA over 29 epochs between 2005 March and 2009 April quasi-simultaneously at 22 GHz and 43 GHz. The data were recorded with eight sub-bands with a bandwidth of 8 MHz and data rate of 256 Mbps. The correlation was performed at the National Radio Astronomy Observatory (NRAO) at the Array Operations Center of the VLBA in Socorro, New Mexico, USA.

The standard procedure to reduce VLBI data makes use of the Astronomical Imaging Processing System (AIPS, Greisen 1990) and the imaging software DIFMAP (Shepherd et al. 1994). Notice that the basic data reduction procedure is common for most of the VLBI results presented through this work, therefore I will describe the process in more detail in the first section of this chapter on the basis of the multi-epoch VLBA observations. For the other observations presented in this thesis I will focus on the differences in data reduction as compared to this standard procedure.

3.1. Data reduction

As pointed out in chapter 2, the visibility data which comes out of the correlator, cannot be used to directly produce an image of the source. Even so the recording systems at the telescopes had improved and the correlator models have become more accurate during the last years, there are still several error terms which influence the phase and amplitude of the visibilities which need to be corrected for. This is done in AIPS, which includes several routines (*tasks*) to perform dedicated VLBI analysis. In the following I will shortly summarize the procedures that need to be applied to get a fully calibrated dataset. A more comprehensive introduction can be found in Taylor et al. (1999), or in the AIPS cookbook (Greisen 2011).

In order to calibrate the visibility amplitude as a first step the task ACCOR is used to correct for errors in the sampler thresholds. Afterwards the task APCAL applies the information from gain curves and system temperatures which are measured at all stations to convert correlation coefficients into correlated flux density. In the process of gain calibration the visibility amplitude will change to Jansky¹. In addition APCAL can correct the amplitude for opacity, using

¹Jansky is defined as $\text{Jy} = 10^{-23} \frac{\text{erg}}{\text{cm}^2 \text{sHz}}$

the weather data tables which are provided by the stations.

To correct the visibility phase as a function of frequency several steps are necessary as there are different factors affecting its value. The main procedures which need to be run for all observations are manual phase-cal and global fring fitting. There may be phase jumps between the sub-bands (IF) due to different signal paths through the electronics, or clock offsets. Even so these should not occur anymore for digital systems as the present VLBA backends, it should be checked. For example already adding a non-VLBA telescope to a VLBA observation may introduce additional instrumental phases and delays. In case of the multi-epoch VLBA observation of NGC 1052 this correction was done by making use of pulse signals, which are inserted into the signal paths during the observation. There are several VLBI arrays which do not inject pulse calibration. In these cases the jumps are corrected manually by solving for the additional terms via fring fitting on a short calibrator scan using the task FRING which solves for the residual delay and delay rate in the data. As a final step FRING is used to solve globally for residual delays and rates for each antenna for all baselines to a common reference antenna and for all times. After averaging over frequency within each sub-band, data are exported from AIPS to perform hybrid mapping in DIFMAP.

In the case of VLBA observations dedicated procedures for the array were used for calibration, which are described in more detail in the AIPS cookbook (Greisen 2011).

In DIFMAP images are produced by a deconvolution method called CLEAN (Högbom 1974). As a first step the DIFMAP software is used to flag *bad* data either for individual telescopes or for baselines, to average the data, and to derive correct statistical weights. While *cleaning* a number of delta-functions (further called *clean components*) is fitted iteratively to the visibilities to remove features in the so called *dirty image*, which is a result of the finite sampling of the correlation function as described in chapter 2, until the noise level is reached. As soon as a satisfactory model of *clean components* is obtained the procedure GSCALE in DIFMAP is used, to derive amplitude correction factors for each telescope and IF by applying an amplitude self-calibration over all telescopes. Afterwards the initial *clean model* is deleted and the corrected data is used for further analysis in DIFMAP. Several iterations of the CLEAN algorithm and phase and amplitude self-calibration loops yield the final images. Table 3.1 lists the final 43 GHz image parameters obtained for all epochs of the VLBA observations.

Table 3.1.: Image parameters for all observations at 22 GHz and 43 GHz (natural weighting).

Epoch ¹	VLBA code ²	Frequency ³ [GHz]	RMS ⁴ [$\frac{\text{mJy}}{\text{beam}}$]	S_{peak} ⁵ [$\frac{\text{Jy}}{\text{beam}}$]	S_{tot} ⁶ [Jy]	b_{maj} ⁷ [mas]	b_{min} ⁸ [mas]	PA ⁹ [°]
2005-03-14 †	BR099A	43	1.21	0.33	0.80	0.46	0.20	7.37
		22	8.33	0.27	0.84	0.72	0.30	4.64
2005-04-22 * †	BR009B	43	1.23	0.29	1.64	1.11	0.21	−18.56
		22	0.70	0.53	2.09	2.32	0.36	−18.58
2005-06-06	BR099C	43	0.99	0.41	1.17	0.69	0.20	−16.85
		22	0.68	0.64	2.26	0.96	0.37	−10.34
2005-07-18	BR099D	43	0.75	0.52	1.00	0.52	0.18	−11.36
		22	0.50	0.21	1.08	0.80	0.31	−4.86
2005-08-22	BR099E	43	1.20	0.47	1.51	0.51	0.18	−12.80
		22	0.85	0.58	1.99	0.89	0.32	−9.62

Table 3.1.: Continuation from previous side

Epoch ¹	VLBA code ²	Frequency ³ [GHz]	RMS ⁴ [$\frac{\text{mJy}}{\text{beam}}$]	S_{peak} ⁵ [$\frac{\text{Jy}}{\text{beam}}$]	S_{tot} ⁶ [Jy]	b_{maj} ⁷ [mas]	b_{min} ⁸ [mas]	PA ⁹ [°]
2005-10-07	BR099F	43	1.05	0.48	1.30	0.49	0.19	−8.47
		22	0.75	0.44	1.39	0.86	0.33	−6.25
2005-11-13	BR099G	43	0.68	0.26	0.80	0.50	0.18	−9.88
		22	0.31	0.16	0.95	0.92	0.33	−9.04
2005-12-18 ^{★ †}	BR009H	43	1.02	0.40	0.91	0.64	0.20	−11.64
		22	0.55	0.40	0.94	1.09	0.34	−10.05
2006-01-15	BR099I	43	0.84	0.32	0.78	0.51	0.20	−8.11
		22	2.00	0.29	1.30	0.70	0.26	−7.23
2006-03-06	BR119A	43	0.93	0.40	0.83	0.52	0.20	−8.12
		22	5.58	0.36	1.28	0.65	0.26	−2.84
2006-04-19 [†]	BR119B	43	0.74	0.41	1.04	0.48	0.18	−7.15
		22	1.69	0.19	1.23	0.65	0.25	−4.03
2007-01-14 [†]	BR120A	43	0.41	0.21	0.74	0.61	0.26	10.05
		22	0.30	0.21	0.61	0.86	0.36	−3.54
2007-03-04	BR120B	43	0.35	0.24	0.69	0.41	0.17	−3.73
		22	0.27	0.23	0.67	0.89	0.36	−2.42
2007-05-05	BR120C	43	0.42	0.25	0.49	0.40	0.16	−5.15
		22	0.35	0.26	0.59	0.78	0.31	−5.11
2007-06-17	BR120D	43	0.38	0.30	0.64	0.51	0.17	−8.27
		22	0.32	0.28	0.70	0.93	0.32	−5.73
2007-08-11	BR120E	43	0.44	0.26	0.56	0.53	0.18	−12.30
		22	0.32	0.27	0.63	0.84	0.33	−4.99
2007-10-01 [†]	BR120F	43	0.40	0.29	0.63	0.88	0.49	21.76
		22	0.30	0.29	0.60	1.40	0.39	−16.64
2008-01-11 ^{★ †}	BR120G	43	0.67	0.28	0.66	0.59	0.20	−11.12
		22	0.17	0.22	0.50	0.96	0.34	−5.99
2008-04-04	BR120H	43	0.37	0.21	0.73	0.54	0.19	−11.98
		22	0.19	0.29	0.72	1.22	0.37	−15.58
2008-05-27	BR120I	43	0.77	0.27	0.58	0.48	0.20	−4.82
		22	0.21	0.24	0.64	0.92	0.33	−8.59
2008-05-04	BR130A	43	0.56	0.30	0.70	0.42	0.16	−6.07
		22	0.24	0.25	0.72	0.87	0.31	−8.35
2008-06-16	BR130B	43	0.55	0.27	0.63	0.50	0.21	−2.34
		22	0.24	0.24	0.65	0.86	0.33	−6.65
2008-07-26	BR130C	43	0.70	0.36	0.64	0.47	0.20	−4.37
		22	0.31	0.20	0.52	0.77	0.29	−6.67
2008-09-06	BR130D	43	0.77	0.31	0.69	0.59	0.25	−5.82
		22	0.27	0.16	0.67	0.95	0.32	−10.85
2008-10-27 [†]	BR130E	43	0.47	0.11	0.78	0.44	0.18	−4.77
		22	0.24	0.21	0.95	0.89	0.32	−8.94
2008-12-05 [†]	BR130F	43	0.50	0.22	0.72	0.76	0.32	15.87
		22	0.20	0.17	0.86	0.90	0.33	−7.99

Table 3.1.: Continuation from previous side

Epoch ¹	VLBA code ²	Frequency ³ [GHz]	RMS ⁴ [$\frac{\text{mJy}}{\text{beam}}$]	S_{peak} ⁵ [$\frac{\text{Jy}}{\text{beam}}$]	S_{tot} ⁶ [Jy]	b_{maj} ⁷ [mas]	b_{min} ⁸ [mas]	PA ⁹ [°]
2009-01-18 †	BR130G	43	0.50	0.26	0.69	0.99	0.37	22.77
		22						
2009-03-08	BR130H	43	0.41	0.15	0.64	0.44	0.18	−3.25
		22	0.26	0.18	0.71	0.91	0.34	−4.37
2009-04-16	BR130I	43	0.32	0.16	0.65	0.43	0.16	−7.43
		22	0.21	0.26	0.82	0.90	0.34	−6.9

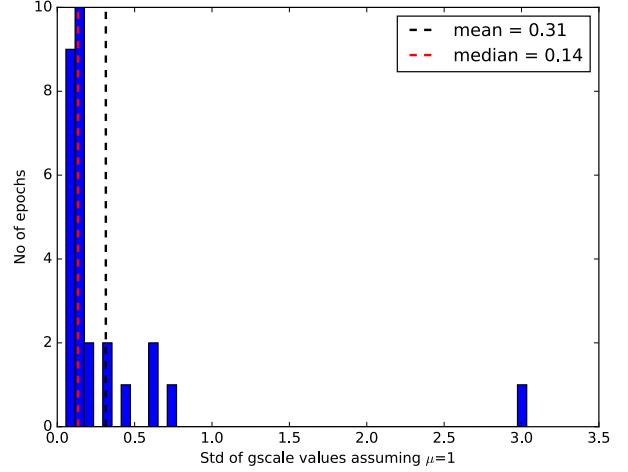
¹ date of VLBA observation, *: excluded in 43 GHz analysis, †: excluded in combined 43 GHz and 22 GHz analysis ² VLBA experiment code ³ frequency ⁴ rms noise level of image. The RMS was derived in ISIS by fitting a Gaussian profile to the distribution of pixel values in the images; the rms corresponds to the sigma of the best-fit profile ⁵ peak flux density ⁶ total flux density ⁷ FWHM major axis of restoring beam ⁸ FWHM minor axis of restoring beam ⁹ PA of major axis of restoring beam

To parameterize the image properties, two-dimensional Gaussian functions were fitted to the visibility data in DIFMAP (Baczko et al. 2019) (in the following the Gaussian functions corresponding to distinct features in the image are called “components”). This was performed independently for each observation until satisfactory models for all epochs were obtained. Hence, the model is stable and reduces the noise in the image as much as possible. The parameters of all model components are listed in the Appendix (Tables A.1 to A.8). The model fitting algorithm solved for the parameters total flux, distance, and major axis to fit the interferometric visibilities. The axial ratio for most jet components was fixed to unity to get the most satisfactory and easy model, whereas it was left as free parameter for a large portion of the core components. The models were iterated, meaning various combinations of number, position, and shape of Gaussian components were tested to find consistency between adjacent epochs.

The uncertainty of amplitude was estimated by comparing the final CLEAN models and the raw data before any self-calibration. In this scope GSCALE correction factors had been obtained using the CLEAN model and the raw data. Based on the whole sample of 43 GHz observations the distribution of GSCALE factors was analysed. I derived the standard deviation of GSCALE values for all IFs and antennas assuming a *true* mean value of unity. The uncertainty of amplitude is then given by the median of the final distribution for all observations. Based on the sample of 43 GHz observations I estimated the uncertainty of amplitude to be 14% (see Fig. 3.1). However, this analysis includes observations that turned out to be very noisy, as well as observations with a much higher data quality. In the case of the latter the uncertainty would be largely overestimated. Therefore, an uncertainty for the amplitude of 10% was assumed, which is a conservative uncertainty for the VLBA (5% are assumed by MOJAVE, Lister et al. (2019), whereas Homan et al. (2002) evaluated typical uncertainties of jet features of 5%-10%).

I assigned uncertainties to the data points as follows: the error bar in the width of each model-fit component m was set to $\sigma_{W_m} = W_m / (S/N)_m$, where $(S/N)_m$ is the signal-to-noise ratio (S/N) of the component peak to the residual noise in the model-fit map, and W_m is the

Figure 3.1: Distribution of overall factors in amplitude correction (GSCALE task in DIFMAP) for all 43 GHz observations. The histogram shows the standard deviation of antenna amplitude correction factors for all IFs from unity for each observation. The uncertainty of amplitude based on statistical analysis is therefore given by the median of the distribution.



full width half maximum (FWHM) of the Gaussian model-fit component (Fomalont 1999). The error on the position of the Gaussian components depends on the remaining noise in the CLEAN and model-fit maps, the size of the components, and the beam axis. Therefore, the positional uncertainty was defined as

$$\delta\theta = \sqrt{\left(\frac{b_{\text{paj}}}{(S/N)_c}\right)^2 + \left(\frac{a_{\text{paj}}}{(S/N)_m}\right)^2}, \quad (3.1.1)$$

where b_{paj} is the beam axis and a_{paj} is the component axis along the jet position angle (PA), which is equal to 64° . $(S/N)_{c/m}$ is the S/N of the image peak to the residual noise in the CLEAN/model-fit map. In the case of very small errors for small component sizes I set a lower boundary to the positional error equal to the beam size divided by 10, following the approach by Lister et al. (2009).

3.2. Results

Three datasets were excluded from the analysis (BR099B, BR099H, and BR120G) due to poor data quality. There are two periods without observations for about half a year. Over these periods the morphology of the source changes significantly and cannot be tracked. The data are divided into three time blocks: “Block 1”: from 2005 to 2006; “Block 2”: during 2007; and “Block 3”: from 2008 to 2009. The individual images, with the Gaussian model fit components plotted on top of the CLEAN images are shown in Figures 3.2 and 3.3.

For component identification, images were aligned on the central bright feature that is observable in almost all epochs. It is located at the image peak, and, therefore, at the image origin. This approach differs from that used by Böck (2012), who aligned the images at 15 GHz, 22 GHz, and 43 GHz on the center of the emission gap that is dominant at frequencies of 22 GHz and below. As there is no indication of strong absorption effects at 43 GHz, the central bright feature is assumed to pinpoint the position of the central SMBH and thus remains constant over time.

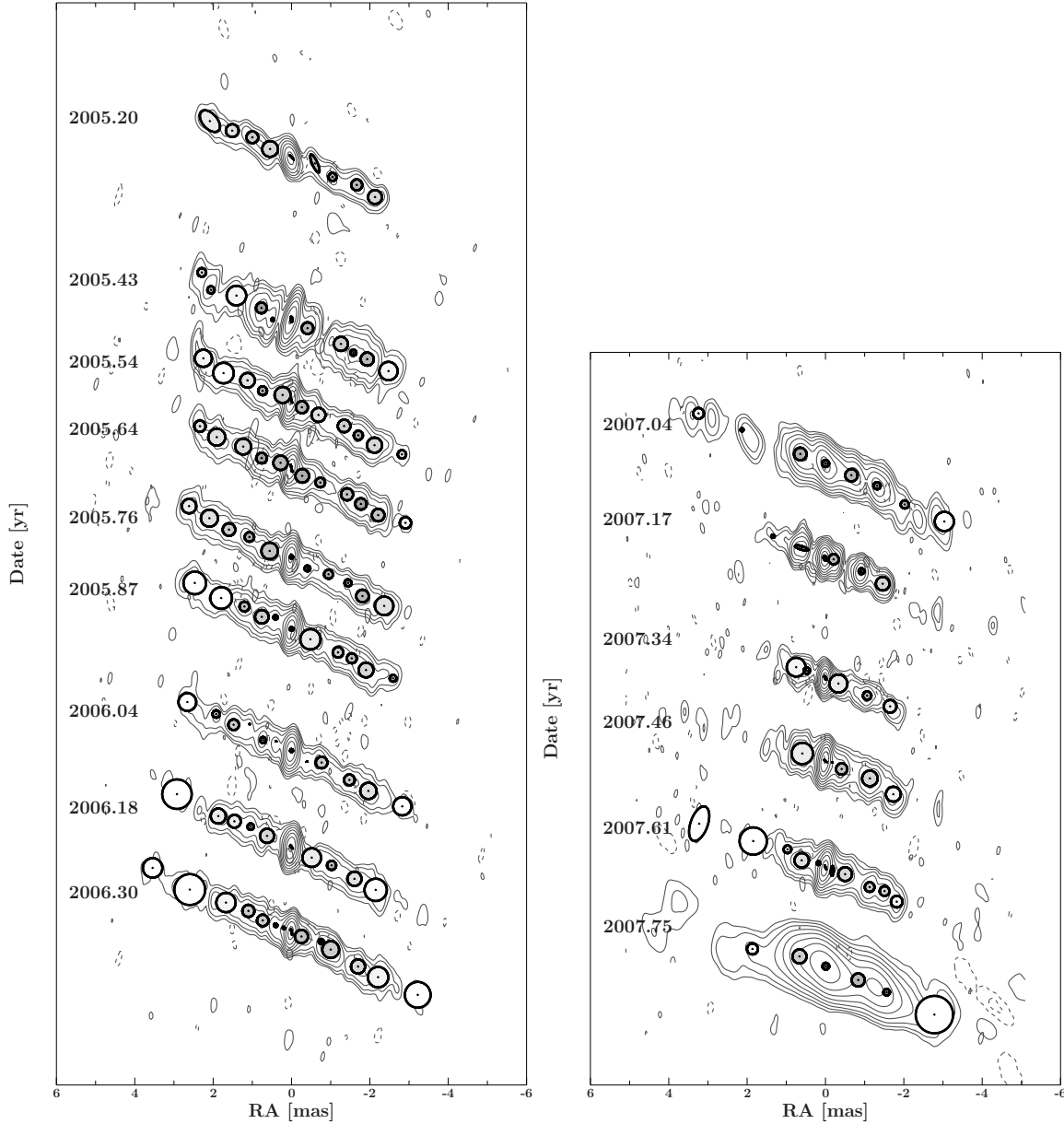


Figure 3.2.: CLEAN contour maps with overplotted model components for the first and second block of NGC 1052 observations at 43 GHz. The date of observation is printed left of each image. The brightness temperatures of the components are represented by a filling factor; brighter components correspond to lower brightness temperatures. The contours start at 3 times the noise level and increase logarithmically by factors of 2.

3.2.1. Image stacking

After aligning all images to the bright central peak, a stacked image was produced by adding all analyzed 43 GHz observations pixel by pixel followed by averaging (see Fig. 3.4) similar to the procedure described in [Pushkarev et al. \(2017\)](#). Both jets are fairly symmetric and have

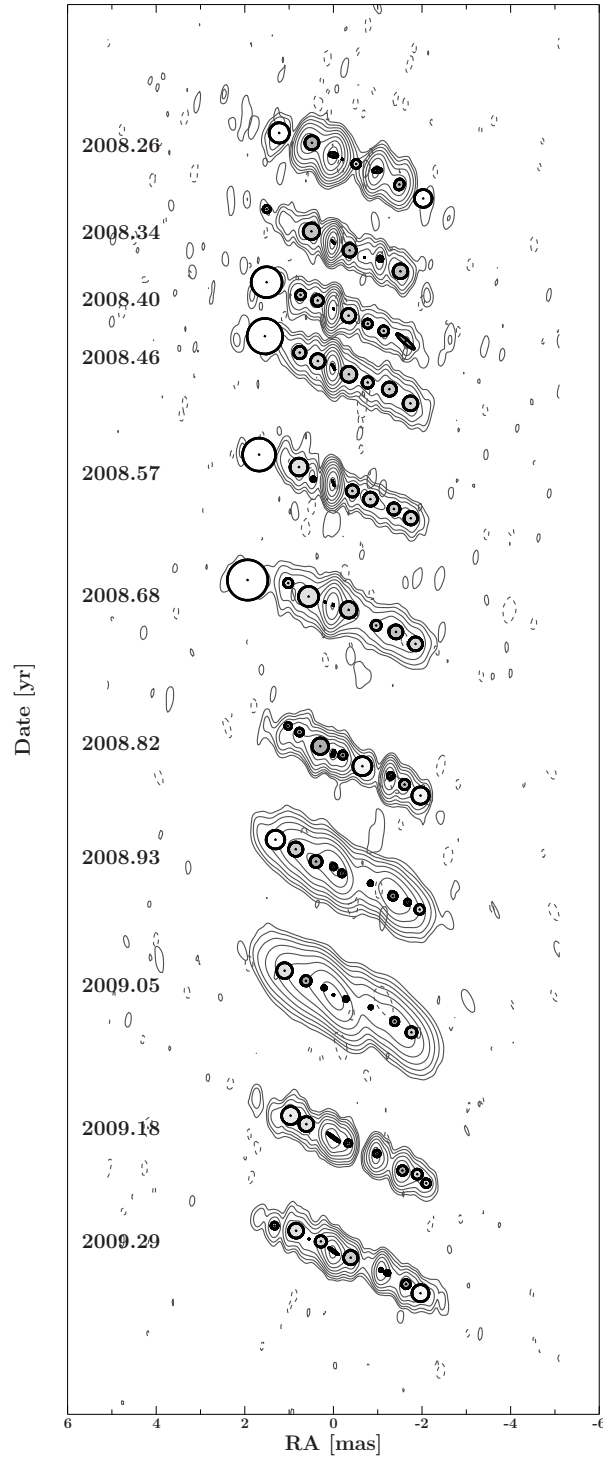


Figure 3.3.: CLEAN contour maps with overplotted model for the third block of NGC 1052 observations at 43 GHz. The date of observation is printed left of each image. The brightness temperatures of the components are represented by a filling factor; brighter components correspond to lower brightness temperatures. The contours start at 3 times the noise level and increase logarithmically by factors of 2.

an extent of around 4 mas at this wavelength. A cut along the jet PA at 64° (from north to east) gives the flux density profile along the jet axes and is illustrated in the lower panel. It forms a plateau from -1 mas to -2 mas along the cut, after which the flux density of the western jet drops off more steeply than the eastern jet.

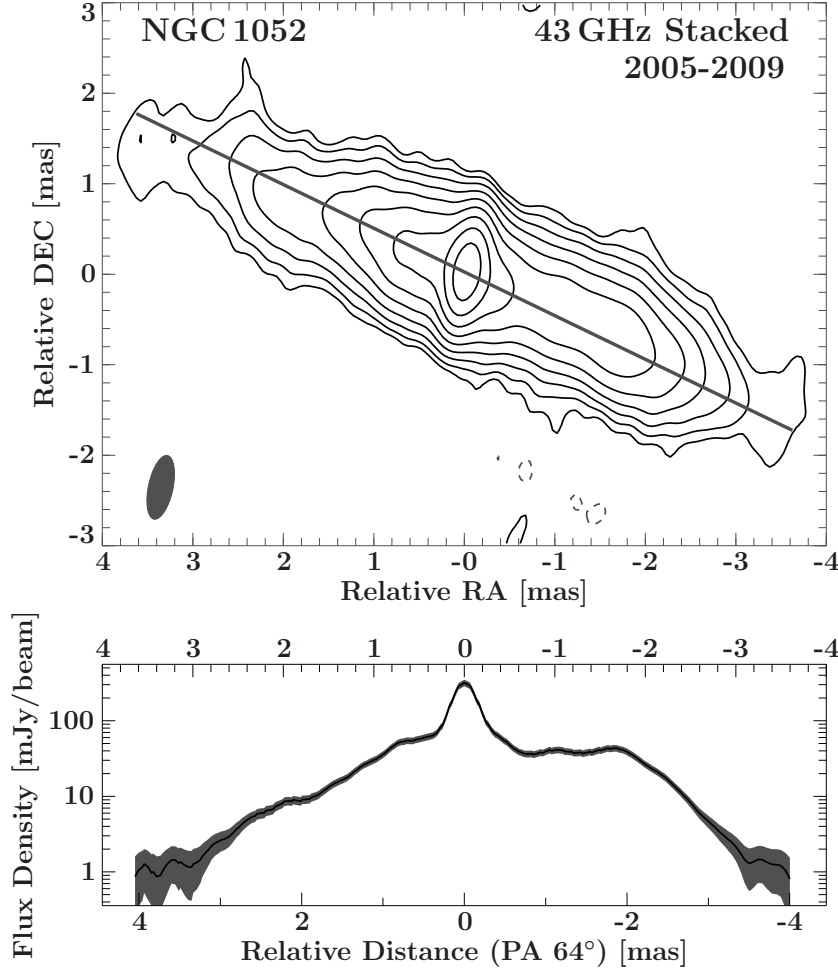


Figure 3.4.: Stacked image for all observations from 2005 to 2009 (*top panel*) and flux density along a cut in the jet direction of 64° (*bottom panel*). This cut is indicated as a line along the jet axis in the contour map. The common beam for the stacked image is shown in the lower, left corner of the *top panel*. For the stacked image, all images are summed up and divided by the number of images. The contours start at 5 times the noise level and increase logarithmically by factors of 2.

3.2.2. Spectral Index maps

To study the spectral index distribution of the twin-jet system between 43 GHz and 22 GHz, 22 GHz simultaneous observations were used (Section 3.2.2). Prior to calculating the spectral indices, the images at both frequencies were aligned (Section 3.2.2) and convolved with a

common beam. Four observations were found to have insufficient image quality for a proper alignment and further five observations did not have a reliable Gaussian model fit at 22 GHz and thus were excluded. After the exclusion of these epochs nineteen epochs remain available for a reliable spectral index analysis.

22 GHz – to 43 GHz alignment

I used optically thin features in both jets to align the images at both frequencies (Kadler et al. 2004b; Fromm et al. 2013). The most suitable feature for the alignment is located at around -2 mas in RA distance to the eastern jet core in the 22 GHz image. Figure 3.5 gives an example of the alignment applied for the beginning, middle, and end of the observational campaign. These three images are a good representation of the typical morphology during the individual time blocks and reveal easy to compare Gaussian model fit components. In case of the 22 GHz images I used the Gaussian model fits produced by Böck (2012), which are distributed similarly to the components at 43 GHz. For the alignment the beam parameters were not changed (see Tab. 3.1 for the individual image parameters at both frequencies).

The alignment of the images sets the central peak in the 43 GHz image around 0.6 mas to the west of the 22 GHz eastern jet peak. For all three examples, the 22 GHz model reveals one Gaussian component at the position of the 43 GHz central component. This is the case for a large percentage of the nineteen epochs used in this work, although the 22 GHz central component is substantially fainter and less well defined than the corresponding 43 GHz component.

The four years of observations reveal a rapidly changing twin-jet system. This makes the results difficult to compare with earlier observations. For example, in a multi-frequency observation in 2000, Sawada-Satoh et al. (2008) identified the brightest feature at 43 GHz with the eastern jet core at 22 GHz. A nearby western component, identified as C4, resides close to the location where the central engine is suspected. Accounting the difference in flux density to the variability of the jets, it may well be identified with the central feature from VLBA images presented in this work.

Spectral analysis

After aligning the images of all epochs, spectral index maps are produced based on the hybrid images. The spectral analysis is based on the assumption that the flux density has a power law dependence of the frequency as $S \propto \nu^{+\alpha}$, with the spectral index α is defined as:

$$\alpha = \frac{\log(S(\nu_1)/S(\nu_2))}{\log(\nu_1/\nu_2)}. \quad (3.2.1)$$

Representative spectral images are shown in the right column of Fig. 3.5 and the common beams for both frequencies used for each map are listed in Tab. 3.2. The spectral index distributions reveal significant absorption in the region of the gap at 22 GHz, reaching spectral indices of $\alpha = 4$ in individual maps. This supports previous results of a free-free absorbing torus covering parts of the western jet (Kameno et al. 2001; Sawada-Satoh et al. 2008) up to 43 GHz (Vermeulen et al. 2003; Kadler et al. 2004b).

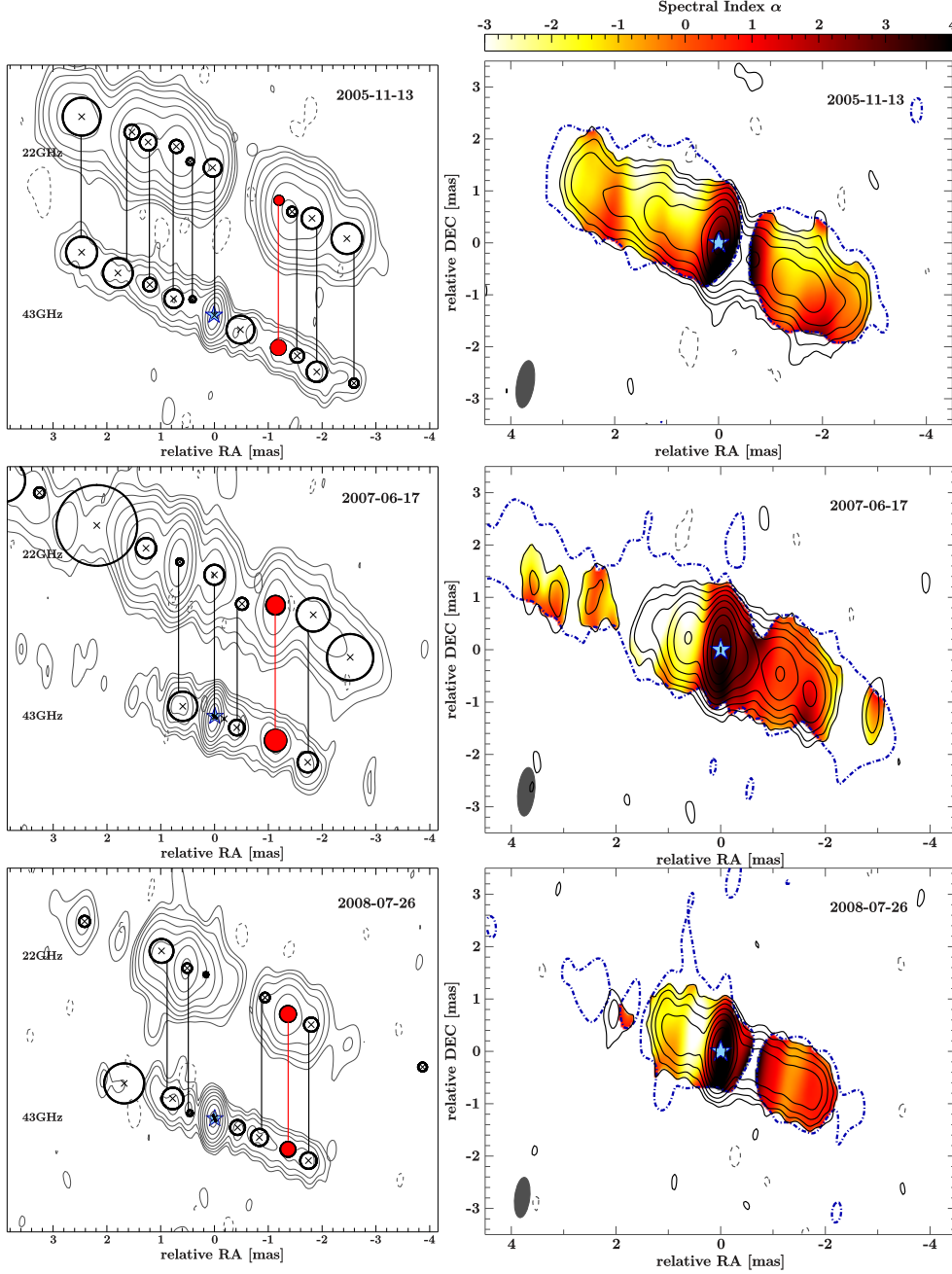


Figure 3.5.: (*Left*) Three examples of the alignment of the 22 GHz and 43 GHz images of NGC 1052 during the observational campaign in 2005–2009. The optically thin feature ~ 2 mas to the west of the 22 GHz jet core was used (highlighted in red) to derive the relative shift between the two frequencies. The Gaussian model components are plotted on top of the contour clean maps. Vertical lines connect the components identified between both frequencies. The contours start at 3 times the noise level and increase logarithmically by factors of 2. The beam parameters for the 6 observations are listed in Tab. 3.1. (*Right*) Resulting spectral index maps between 22 GHz (dotted dashed blue contours) and 43 GHz (black contours) after applying the shifts on optically thin features. The restoring beam for each epoch is plotted in the lower left corner of the maps; the parameters are listed in Tab. 3.2. The blue star indicates the assumed location of the dynamical center.

Figure 3.6 shows a spectral index map derived from one stacked map for all nineteen epochs at both frequencies. Before stacking, the images were restored with a common beam and images were aligned as discussed in the previous section.

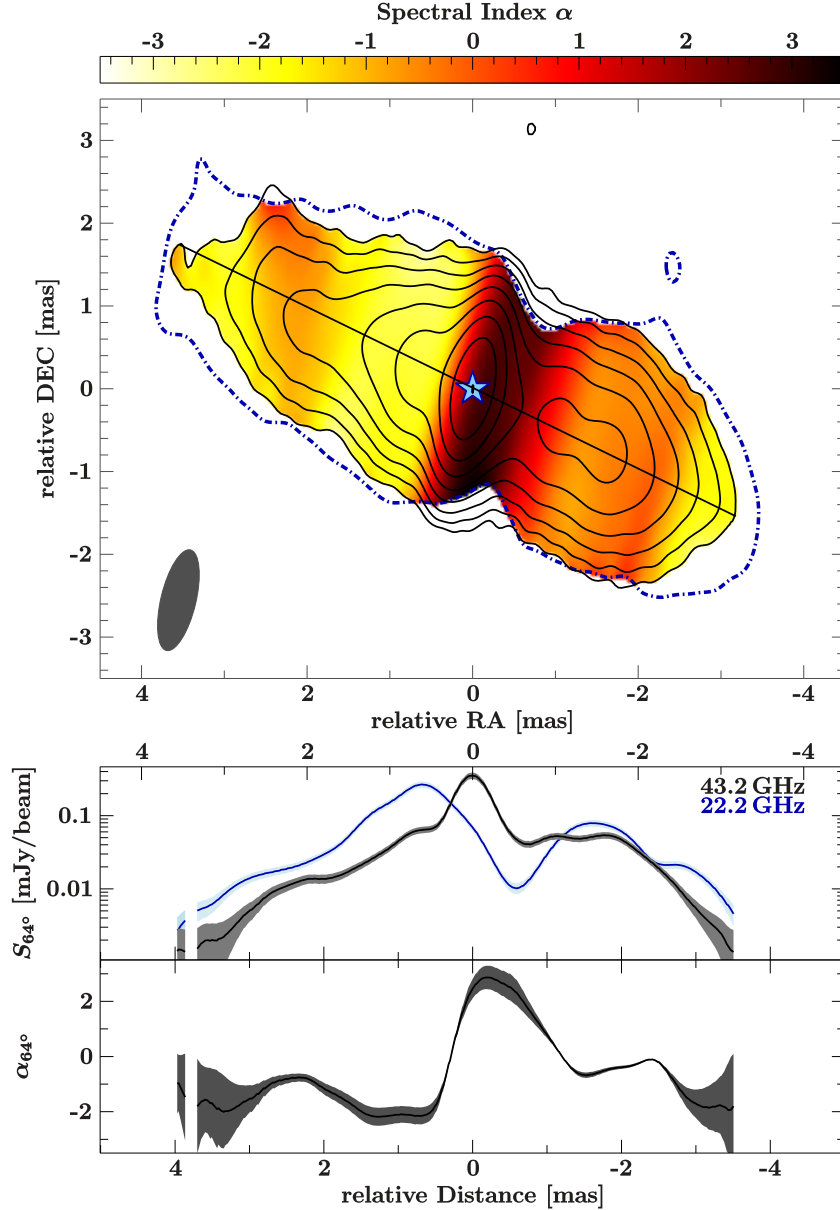


Figure 3.6.: Stacked spectral index map ($S \propto \nu^{+\alpha}$) combining nineteen 22 GHz (blue dash-dotted contour) and 43 GHz (black contours) images between 2005 and 2009. A cut along the direction of the jets is shown in the lower panels, depicting the flux density profile and spectral index along the jet axis (see line in top panel). The blue star indicates the assumed location of the dynamical center. The contours of the 43 GHz map start at 5 times the noise level and increase logarithmically by factors of 2. For the 22 GHz map only one contour at 5 times the noise level is shown.

Table 3.2.: Parameters of the common beam in the spectral index maps shown in Fig. 3.5

Epoch	b_{maj} [mas]	b_{min} [mas]	PA [°]
2005-11-13	0.92	0.33	−9,04
2007-06-17	0.93	0.32	−5.73
2008-07-26	0.77	0.29	−6.67

3.2.3. Flux density evolution

The evolution of the flux density over time is derived from the distribution of positive CLEAN components in the clean images at 43 GHz and 22 GHz. I included nineteen observations in this comparison, analogous to the spectral analysis in Section 3.2.2. The total flux density and ratio of the brighter to fainter jet is shown in Fig. 3.7. Similar to Section 3.2.2 first the shifts between the 22 GHz and 43 GHz images were applied, before excluding CLEAN components up to 0.8 mas distance in east and west to the 43 GHz core at both frequencies to include only the optically thin jet regions. In this way I make sure that only the parts of the jets at both frequencies are included that are, indeed, comparable. All remaining CLEAN components have been summed up for the eastern and western jets. NGC 1052 shows significant variability over

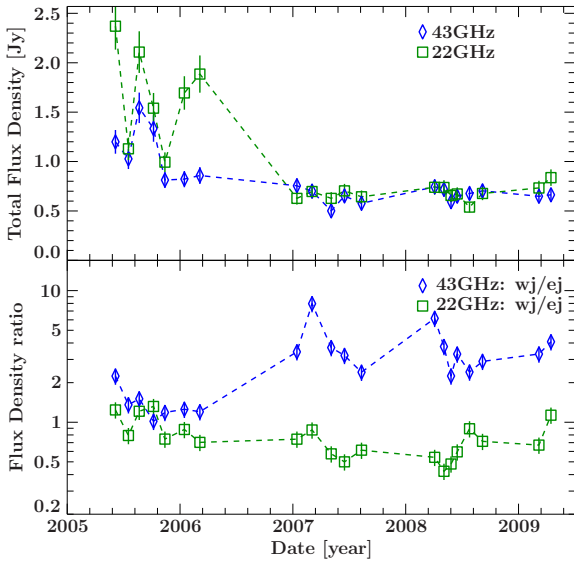


Figure 3.7: (*Top:*) Total flux density of nineteen hybrid maps at 22 GHz (green squares) and 43 GHz (blue diamonds). (*Bottom:*) Flux density ratio of western to eastern jet at 22 GHz (green squares) and 43 GHz (blue diamonds).

the four years of our observations. The total flux density rises to a maximum of 1.6 Jy in 2005 August, declines below 0.8 Jy during 2007 April, and remains at this level for the rest of the observations. The flux density evolution of the core as well as the western and eastern jets follow the trend of the total intensity. In contrast to previous observations in the years 1995-2002, and 2004 (Vermeulen et al. 2003; Kadler et al. 2004b; Baczko et al. 2016a), the western jet is brighter than the eastern jet for the whole period 2005-2009. Because of this deviation I

assume the western jet to approach and the eastern jet to recede for the derivation of viewing angle in Sect. 3.3.2.

3.2.4. Kinematics

I used the Gaussian model components in the twenty-six 43 GHz images to examine the dynamics in both jets. The central peak, observable at all epochs at 43 GHz, was assumed to be the dynamical center of the source. This is a natural choice based on the clear morphology at 43 GHz and 86 GHz (cf. Fig. 4 in Baczko et al. 2016b). In the unlikely case that the 43 GHz core is offset from the dynamical center, it still can be expected that the 43 GHz core does not shift with time. The same holds for the dynamical center and therefore the results obtained in this section are not affected. The Gaussian component fitted to this feature was therefore used to align the images. The Gaussian model components were cross-identified between adjacent observing epochs. This enabled me to apply linear fits to this feature's core distance as a function of time (see Fig. 3.8) to determine the radial proper motion of the feature in the sky. The jet system is rapidly changing, therefore, the three time blocks were analysed separately.

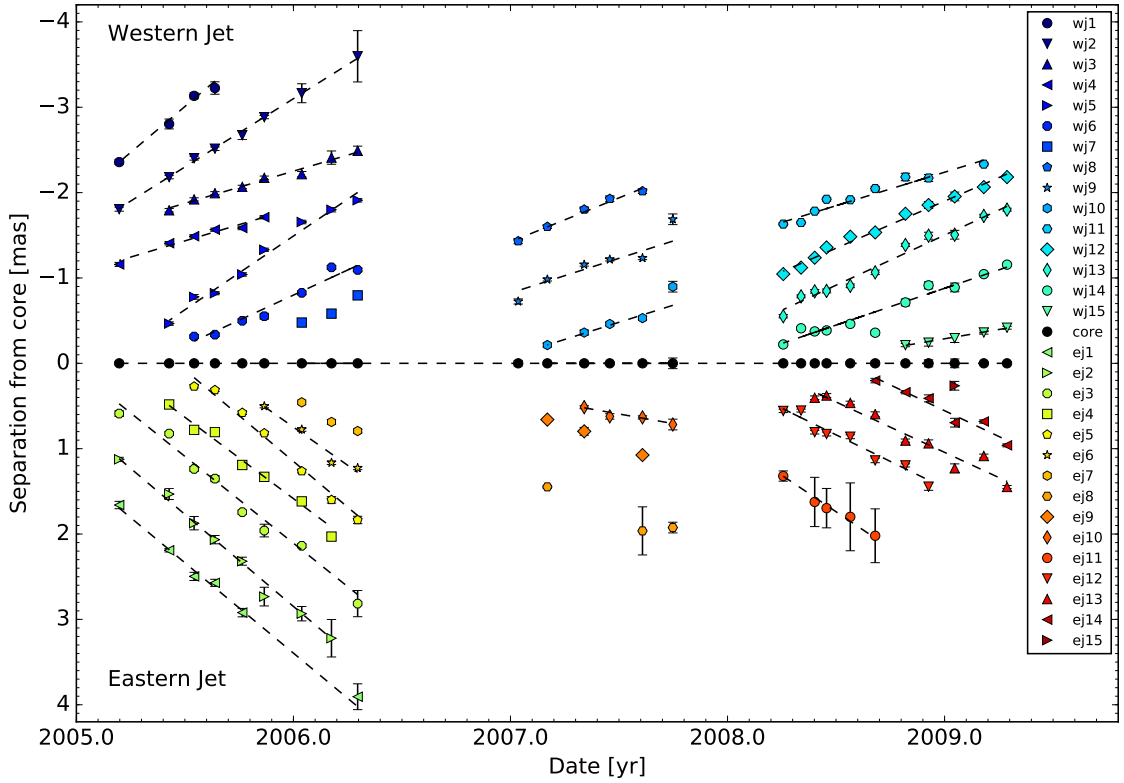


Figure 3.8.: Core separation of individual Gaussian model-fit components over time. The fit to a linear function for each component is indicated by a dashed line (corresponding slopes are listed in Tab. A.9). The eastern jet is plotted in the lower half of the plot, the western jet in the top half of the plot.

Only components found in at least four epochs were taken into account. This results in

only one derived velocity for the eastern jet during block 2, which is ej10. Together with component wj15 its maximum separation from the center is < 1 mas and shows a low velocity compared to the other tracked components. It is difficult to decouple their properties from the core region. As a result, both components are not considered in the following analysis. Therefore, no mean speed was derived for the eastern jet in Block 2.

The overall mean, maximum, and minimum values for each jet and the mean values for each time block and both jets are listed in Tab. 3.3. The uncertainties represent the standard deviation from the mean, assuming an uncertainty on the position of the components as defined in Section 3.1. I derived $\beta_{\text{wj}} = 0.343 \pm 0.037$ and $\beta_{\text{ej}} = 0.529 \pm 0.038$ for the western and eastern jet, respectively.

Table 3.3.: Averaged speeds for the western jet (top) and eastern jet (bottom) for each observational time block and mean, minimum, and maximum for all observations for each jet.

Western jet			Eastern jet		
	$v_{\text{mean}} [\text{mas yr}^{-1}]$	$\beta_{\text{mean}} [c]$		$v_{\text{mean}} [\text{mas yr}^{-1}]$	$\beta_{\text{mean}} [c]$
Block 1	1.361 ± 0.230	0.412 ± 0.069	Block 1	2.025 ± 0.060	0.613 ± 0.018
Block 2	0.882 ± 0.074	0.267 ± 0.023	Block 2	–	–
Block 3	0.981 ± 0.093	0.297 ± 0.028	Block 3	1.336 ± 0.125	0.404 ± 0.038
Mean	1.134 ± 0.122	0.343 ± 0.037	Mean	1.749 ± 0.126	0.529 ± 0.038
Min	0.753 ± 0.048	0.228 ± 0.016	Min	1.181 ± 0.098	0.357 ± 0.030
Max	2.152 ± 0.138	0.651 ± 0.042	Max	2.156 ± 0.055	0.652 ± 0.017

3.2.5. Brightness temperature and opening angle

Following the notation of Kadler et al. (2004b), the brightness temperature gradient (for a discussion of temperatures in radio astronomy please see chapter 2) along the jet axis can be approximated by a power law $T_b \propto r^s$ with the power-law index $s = d + n + b(1 - \alpha_s)$, where α_s is the spectral index and assuming that the magnetic field B , the electron density N , and the jet diameter D are described by power laws as $B \propto r^b$, $N \propto r^n$, and $D \propto r^d$.

Orthogonal distance regression fits were applied to the brightness temperature and component size of the Gaussian model components with distance from the core. Given the straightness of the jets and the good agreement of jet width with model components, the size of the model components is assumed to represent the width of the jets. In order to avoid confusion from the core region, all components closer than 0.2 mas to the core were excluded. There are a few components with unphysical delta-like sizes leading to a very high brightness temperature, which exceed the inverse Compton limit. These had been excluded as well from the analysis since they may be mathematically correct, but are unphysical. Uncertainties were assigned as discussed in Section 3.1.

As seen in Fig. 3.9, the brightness temperatures, and jet diameter do not show a simple power-law-like behaviour. However, trends in the gradients s and d for the brightness temperature and the opening angle can be observed, respectively. When fit with a single power law from 0.2 mas to 4 mas the following index values for the eastern jet: $s_{\text{ej}} = -0.97 \pm 0.15$ and

$d_{\text{ej}} = 0.03 \pm 0.09$ were derived. The western jet shows a break in the T_b distribution and jet diameter. In the outer part, the slopes are steeper than in the inner part. Applying two power laws (red lines in Fig. 3.9) from 0.2 mas to 0.9 mas and from 0.9 mas to 4.0 mas results in the parameters listed in Tab. 3.4, suggesting a conical expansion in the outer part for the western jet.

There are several components with small sizes that do not seem to be a good representation of the width of the jets, but rather maybe due to local substructures within the jets (see Fig. 3.2 and 3.3). All model-fit components with sizes below 0.15 mas were excluded (gray diamonds in Fig. 3.9) and power laws were fit to both regions (0.2 to 0.9 mas and 0.9 to 4 mas) for both jets (blue lines in Fig. 3.9). The power-law indices are listed in the bottom part of Tab. 3.4.

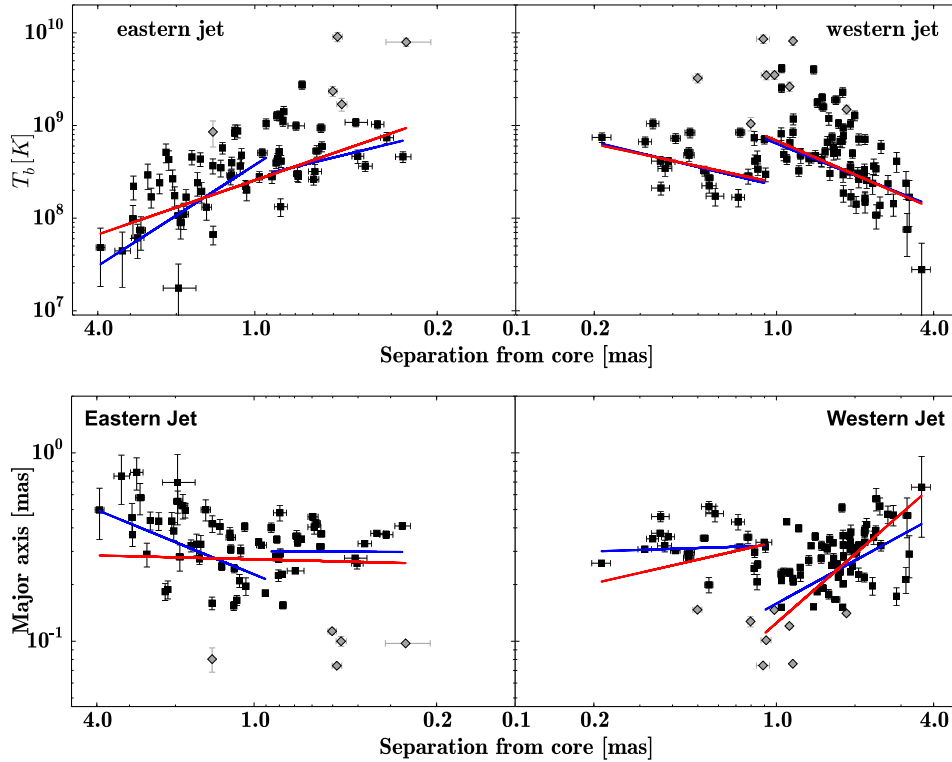


Figure 3.9.: Brightness temperature (Top) and component major axis (Bottom) as functions of the core distance for both jets. Power laws are fitted ($T_b \propto r^s$; $D \propto r^d$) and the indices are printed in Tab. 3.4. Two cases are distinguished: including all data points (red lines) and excluding the gray diamonds, corresponding to circular Gaussian fits whose major axes are smaller than 0.15 mas in size (blue lines). These data points do not seem to be a good representation of the width of the jets, but rather owing to substructures within the jets.

Table 3.4.: Power-law indices for brightness temperature ($T_b \propto r^s$) and jet diameter ($D \propto r^d$) of both jets. Orthogonal distance regression fits had been applied to the different regions as shown in Fig. 3.9.

Fit to all data points				
Region [mas]	s_{wj}	s_{ej}	d_{wj}	d_{ej}
0.2 to 4.0	–	-0.97 ± 0.15	–	0.03 ± 0.09
0.2 to 0.9	-0.60 ± 0.40	–	0.32 ± 0.19	–
0.9 to 4.0	-1.22 ± 0.29	–	1.22 ± 0.16	–
Fit to robust data points				
0.2 to 0.9	-0.68 ± 0.34	-0.68 ± 0.37	0.05 ± 0.07	0.01 ± 0.10
0.9 to 4.0	-1.13 ± 0.27	-1.81 ± 0.39	0.76 ± 0.14	0.57 ± 0.20

3.3. Discussion

3.3.1. Torus

The stacked spectral index map (see Section 3.2.2) reveals an absorbing structure near the base of the two jets. The absorber covers a region of about 0.4 mas (0.04 pc) to the east and 0.8 mas (0.08 pc) to the west from the 43 GHz image peak. The spectral index α in this region exceeds the theoretical upper limit for synchrotron self-absorption of 2.5. The 43 GHz core is very close to the peak of the absorbing structure and therefore no significant offset from the dynamic center is expected. Furthermore, both jets show a relatively steep spectrum and have a mean spectral index around -1 , which further decreases to a minimum of ~ -2 . This is in agreement with the values reported by Kadler et al. (2004b) of around -1 in both jets, which suggests that the outer jets are optically thin. It is possible to produce images at both frequencies that show no gap in the emission using the stacked image. This gives a more continuous measurement of the geometry of the absorbing medium than possible in previous works (see, e.g., Kellermann et al. 1999; Kameno et al. 2001; Vermeulen et al. 2003; Kadler et al. 2004b).

Kamenno et al. (2001) derived the distribution of the free-free absorption (FFA) opacity due to the torus and found a peak opacity at 1 GHz of $\tau_{\text{f},1\text{GHz}} = 300$ in the nucleus. The FFA opacity coefficients derived by Sawada-Satoh et al. (2008) are consistent with this, but show a higher mean optical depth in the center of $\tau_{\text{f},1\text{GHz}} = 1000$. Given a frequency dependence of the optical depth as $\tau_{\text{f}} \propto \nu^{-2.1}$ the free-free opacity at 43 GHz can be estimated to $\tau_{\text{f},43\text{GHz}} = 0.11$ for assuming $\tau_{\text{f},1\text{GHz}} = 300$ and to $\tau_{\text{f},43\text{GHz}} = 0.37$ for assuming $\tau_{\text{f},1\text{GHz}} = 1000$. The observed flux density at 43 GHz ($S_{\text{abs}}(43\text{GHz})$) is typically around 300 mJy for the core region. It is connected to the intrinsic flux density ($S_{\text{int}}(\nu)$) and τ_{f} by $S_{\text{abs}}(\nu) = S_{\text{int}}(\nu) e^{-\tau_{\text{f}}}$. For $S_{\text{abs}}(43\text{GHz}) = 300\text{ mJy}$ $S_{\text{int}}(43\text{GHz}) = 335\text{ mJy}$ and $S_{\text{int}}(43\text{GHz}) = 434\text{ mJy}$ are obtained.

Based on these assumptions this region cannot be assumed to be optically thin. However, there are very few epochs in which jet components are close enough to the central core to be affected by absorption (for example for epochs BR130F or BR130E, compare Tab. A.7). These epochs reveal strongly correlated Gaussian model parameters in the innermost jet re-

gions including the core. Therefore, these observations are already not optimal to analyse the innermost region. For all other observations the central component is still the brightest when accounting for absorption and is therefore still the most likely position of the core.

The location of the cut in the power laws in the western jet, as seen in Fig. 3.9, is consistent with the outer edge of the absorbing torus. If some absorption at 43 GHz is assumed, this would result in a reduction of the flux density of the western jet in this region, which would satisfactorily explain the brightness temperature distribution (cf. Kadler et al. 2004a). If the drop in the brightness temperature distribution is only due to the absorption, interpolating the outer gradient inward should give us the real brightness temperatures close to the central region. This results in higher values for the western jet. In addition, the asymmetry observed from 2007 on is even more pronounced.

In comparison, Kadler et al. (2004b) derived power-law index values s between -3.8 ± 0.3 and -4.1 ± 0.8 for the eastern jet at frequencies of 5, 8.4, 22, and 43 GHz. The brightness temperature distribution of the western jet could not be approximated by a simple power law. The fits were consistent for all frequencies but were performed only for components farther away than 2.5 mas from the center. Kadler et al. (2004b) analyzed only one epoch per frequency, whereas this analysis includes twenty-six epochs at 43 GHz, resulting in a more robust statistics. Adding the derived values by Kadler et al. (2004b) to this analysis, the absolute value of the T_b power-law index increases with increasing distance from the core.

In the numerical simulations of Fromm et al. (2018) initially symmetric jets are assumed. However, asymmetries between the jet and counter-jet appear owing to the delicate interplay between absorption and orientation of the jet-torus system and the properties of the observing array.

In the case of overpressured jets embedded in a decreasing pressure ambient medium several recollimation shocks can be formed. The observed signature of a recollimation shock can be described by a stationary local flux density maximum, in contrast to traveling shocks where the local increase in flux density is advected with the plasma. The local increase in pressure and density at the recollimation shocks decreases with distance from the jet nozzle and thus the observed emission signatures of standing recollimation shocks diminish with distance down the jet. Therefore, the strongest recollimation shocks in each jet, which would appear as stationary flux density maxima, should be located to the jet nozzle.

However, depending on the torus properties, the observing frequency and orientation of the jet-torus system these features can be hidden behind the obscuring torus. The obscuring torus becomes optically thinner at higher frequencies offering us a glimpse into the innermost regions of the central engine. As a consequence the local flux density maxima associated with the recollimation shocks may become visible (see Fig. 14 in Fromm et al. 2018). If NGC 1052 is assumed to have a viewing angle $\vartheta \neq 90$, larger absorption is expected along the line of sight to result in less flux in one of the jets (i.e., in the counter-jet). Also large spectral index values (~ 3) can be obtained between the jet and counter-jet owing to the contribution of the FFA in the torus (see Fig. 16 in Fromm et al. 2018). To test whether the jets are initially symmetric or asymmetric, detailed simulations and modeling tailored to NGC 1052 have to be performed.

3.3.2. Jet properties

Morphology

Comparing the first epoch at 43 GHz in 2005 and the 86 GHz image from October 2004 (Baczko et al. 2016b), both images reveal one central bright feature and two fainter, symmetrically evolving jets. Component identification was attempted between both frequency images. However, there are several difficulties that prevent a robust result: 1) There is a gap of five months between the 86 GHz observation and the first 43 GHz observation. Based on this study, the morphology of the source might change significantly during this time. 2) By extrapolating the western jet component locations to the time of the 86 GHz observation, several crossing paths are found. Therefore, it is not clear where the components were located in October 2004. 3) Extrapolating the components in epoch BR099A backward only gives information about the inner 1 mas of the eastern jet, which is not sufficient to compare with the observation at 86 GHz. 4) The quality of the 86 GHz data is not good enough to make a reliable association. For this, a model fit degrading the weights of the long-baseline data (tapering) should be considered, since the S/N in the full-resolution image at 3.5 mm is not sufficient.

As seen in Figures 3.2 and 3.3, there are remarkable differences between the first observational block and the following two. Therefore, stacked images for each block have been produced (compare Fig. 3.10). In Block 1 NGC 1052 shows a symmetric morphology, whereas in Block 2 the jets become asymmetric while the source gets more compact. The extent of the western jet is about 1 mas smaller than in Block 1. The eastern jet becomes less prominent in blocks 2 and 3. It shows only diffuse emission beyond 2 mas. The fits to the jet diameter indicate strict deviations from a conical expansion in the inner 1 mas (corresponding to 0.1 pc) of both jets. At the point of the change in the power-law index, there is a break in the distribution, resulting in smaller major axes at around 1 mas, indicating a possible re-collimation of the jets.

Speed

There is a clear trend toward higher velocities in the eastern jet in comparison to the western jet (see Tab. A.9). For time Block 1 the basic kinematic model was previously presented in Baczko et al. (2016b). The western jet in Block 1 shows a wide spread of velocities. In contrast to that the component velocities in the eastern jet are very similar and have deviations of less than $0.1c$ from the mean value. For Block 2 and Block 3 the western jet is more stable, revealing comparable speeds for all tracked components. However, the overall evolution in both jets show that, besides the clear trend toward higher velocities in the eastern jet, there are significant deviations from the mean speed.

The measured apparent velocities at 15 GHz from Lister et al. (2013) are compared with the values at 43 GHz in Fig. 3.11. The components at 43 GHz have significantly different values than those at 15 GHz with a tendency of higher velocities at higher frequency. As discussed in the previous sections, a circumnuclear torus covers large parts of the western jet, thus FFA results in an obscuration of the inner part at lower frequencies (Kameno et al. 2001; Vermeulen et al. 2003; Kadler et al. 2004b). Its impact at 43 GHz is already small enough so that we to

3. Study of the asymmetry in the jet formation in NGC 1052

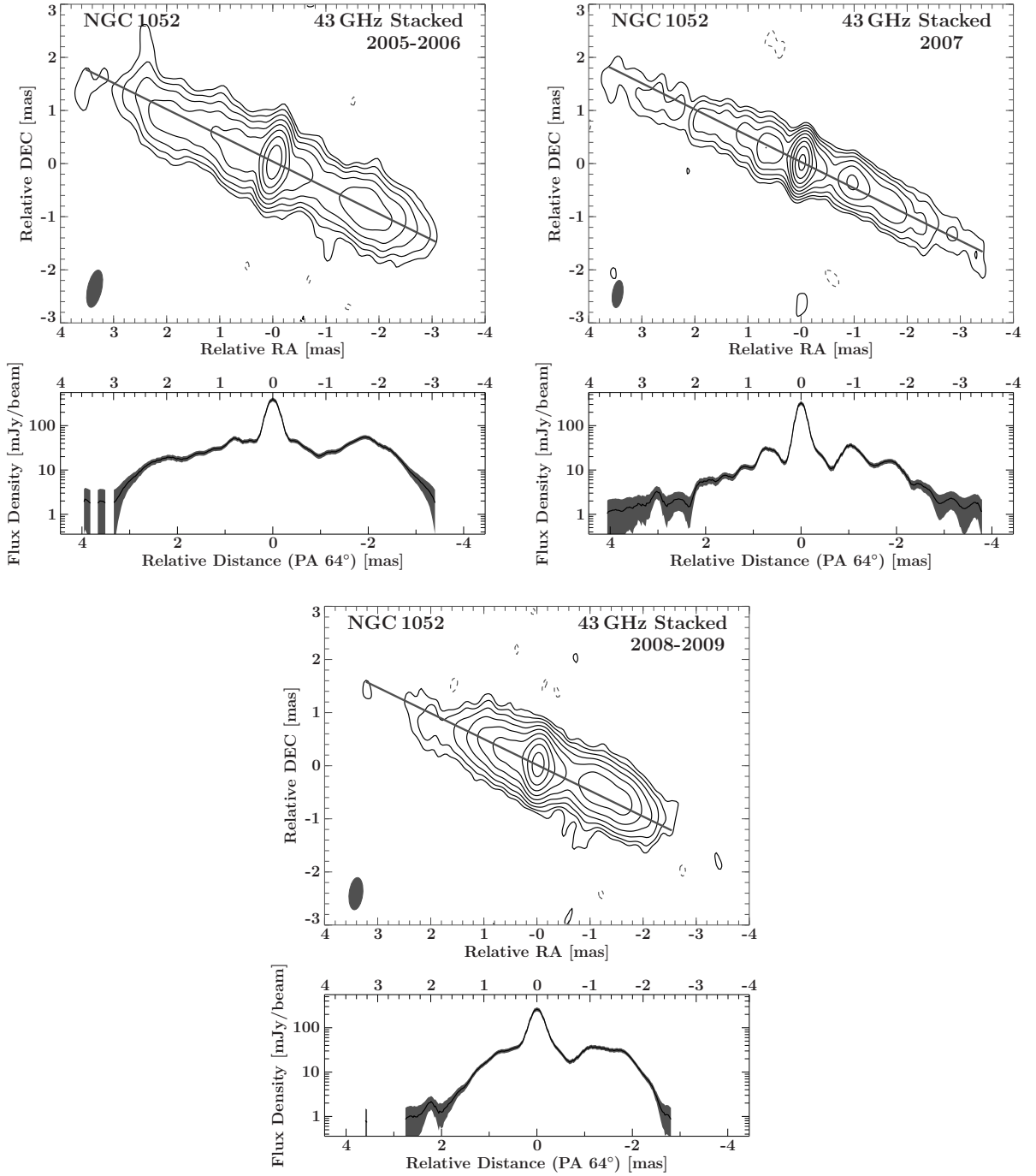


Figure 3.10.: Stacked images with the flux densities along the PA of the jet (for the observations from 2005 - 2006, 2007, and 2008 - 2009). The cut along the PA is shown in the (*bottom panels*), and is indicated in the (*top panels*) as a line along the jet axis. The common beam for the stacked maps is shown in the bottom left corner of the (*top panels*). For the stacked images the maps have been summed up and divided by the number of images. The contours start at 3 times the noise level and increase logarithmically by factors of 2.

peer through this absorbing structure. If the jet has transversal velocity structure, it is likely that a faster moving layer of the jets at 43 GHz is observed as compared to lower frequencies. The slower moving layer of the jet, as observable at 15 GHz, may very well be invisible at 43 GHz owing to less energetic particles that are not emitting at 43 GHz.

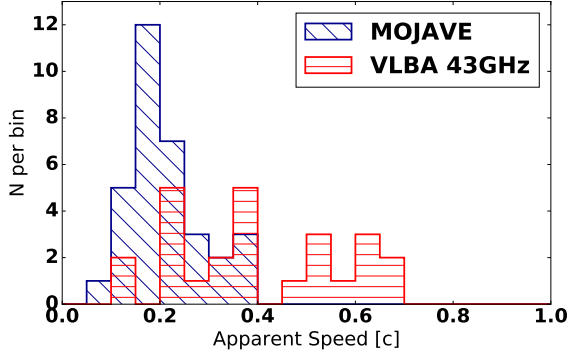


Figure 3.11: Histogram of the apparent velocity of the jet components for this work at 43 GHz (red), and [Lister et al. \(2013\)](#) (blue, MOJAVE) at 15 GHz. The bin size is 0.05 c.

Viewing angle

As described in Chapter 2 the values for velocity and flux density ratios can be used to derive the allowed parameter space for the intrinsic velocity β and the angle of the jets to the line of sight θ_{LOS} (see Sect. 2.3.1). However, the flux-density ratios presented in Sect. 3.2.3, based on the clean-components, excluded a large fraction of the jets in the central region due to better comparison with the images at 22 GHz. To account for the whole source structure at 43 GHz the jet-to-counter-jet ratios derived based on the model-fit components (see Fig. 3.13) were used for the following analysis.

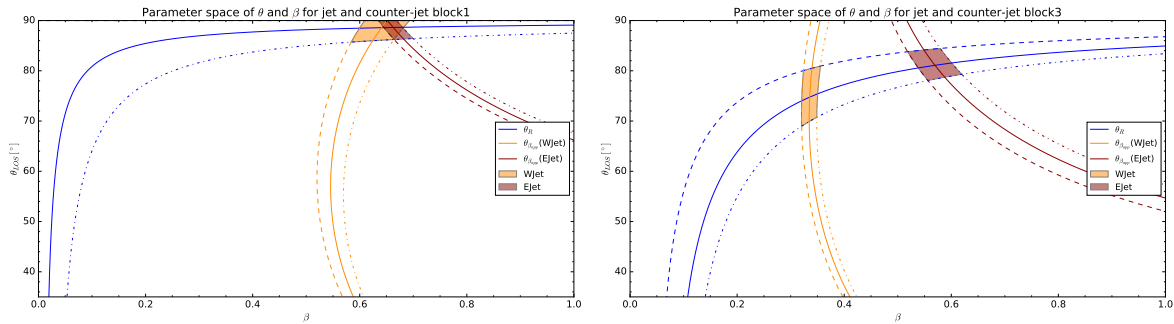


Figure 3.12.: Angle of the jets to the line of sight θ_{LOS} as a function of the intrinsic jet velocity β , constrained by the western-to-eastern jet ratio R (blue) and the apparent maximum velocities for eastern jet (red) and western jet (orange) for observational blocks 1 and 3. The allowed parameter space for θ_{LOS} and β for eastern and western jet is highlighted by the red/orange-shaded region, respectively. The dashed and dash-dotted lines indicate the uncertainty range. There is no common parameter space for both jets and both blocks. The assumption of intrinsic symmetry is therefore contradictory to the results.

As discussed in the previous sections, there are differences in velocity between both jets and the various time blocks. In addition the western jet is consistently brighter than the eastern jet at 43 GHz. This result is contradictory to earlier studies, which showed the eastern jet to be brighter (Kellermann et al. 1999; Vermeulen et al. 2003; Kadler et al. 2004a). There is a change in the jet-to-counter-jet ratio over the span of four years from around $R = 1.1$ up to $R = 2.5$ (see Fig. 3.13c). For the first observational block, the ratio remains at a similar level of around $R = 1.1$; in this period the morphology of the jets appears to be symmetric. In the second observational block (2007) the jets become increasingly asymmetric with a mean ratio of about $R = 1.9$.

Based on these results there is evidence that the jets are not symmetric. However, equations 2.3.6 and 2.3.7 can be used to test this assumption. If symmetry holds, it should be possible to obtain a common region in the parameter space for θ_{LOS} and β that holds for all observations. The eastern jet in observational Block 2 is very short and reveals only very few tracked components, therefore blocks 1 and 3 are compared. In Eq. 2.3.7 the maximum speeds found during the appropriate blocks are used. Based on the herein discussed 43GHz observations and the morphology outside the central region, the western jet is assumed to be the approaching jet and the eastern jet to be the receding jet. As shown in Fig. 3.12 a common region in the parameter space for θ_{LOS} and β is found in Block 1. In Block 3 the velocities depart from each other and cannot be compatible, so it is not possible to combine eastern and western jet assuming intrinsic symmetry.

The assumption that both jets are intrinsically identical in terms of velocity, viewing angle, and an overall symmetric evolution was implicit in the study of the parameter space. However, there is no combination of β and θ_{LOS} that is consistent for both blocks and jets. This contradicts the assumption of symmetry and therefore at least one equality constraint must be lifted.

3.3.3. Source geometry

The observed asymmetries may originate both from asymmetries in the physical nature of the jets themselves or the environment into which they propagate. Assuming the drop in T_b in the inner part of the western jet is due to the absorbing structure, the interpolation of the outer gradient results in higher brightness temperatures close to the central engine compared to the eastern jet. This is most likely explained by a higher brightness of the western jet, thus requiring a larger jet internal energy and/or magnetic flux. For example, this can be achieved by a more energetic ejection producing larger particle internal energy and/or magnetic flux. This would favor an internal asymmetry in the jets. On the other hand, even if assuming the same energy flux is injected at the nozzle of both jets, there can also be disturbances further downstream, resulting in different energy conversion and leading to a possible higher emissivity of the western jet. Given the large scales on which the jets are interacting with the interstellar medium it is most likely that this environment is not identical for both jets. In particular, stronger dissipation or increased mass loading by, for example, stellar winds, can lead to a brighter and slower flow (see, e.g., Bowman et al. 1996; Perucho et al. 2014).

Combining the results from the kinematic analysis at 43 GHz with previous studies at lower

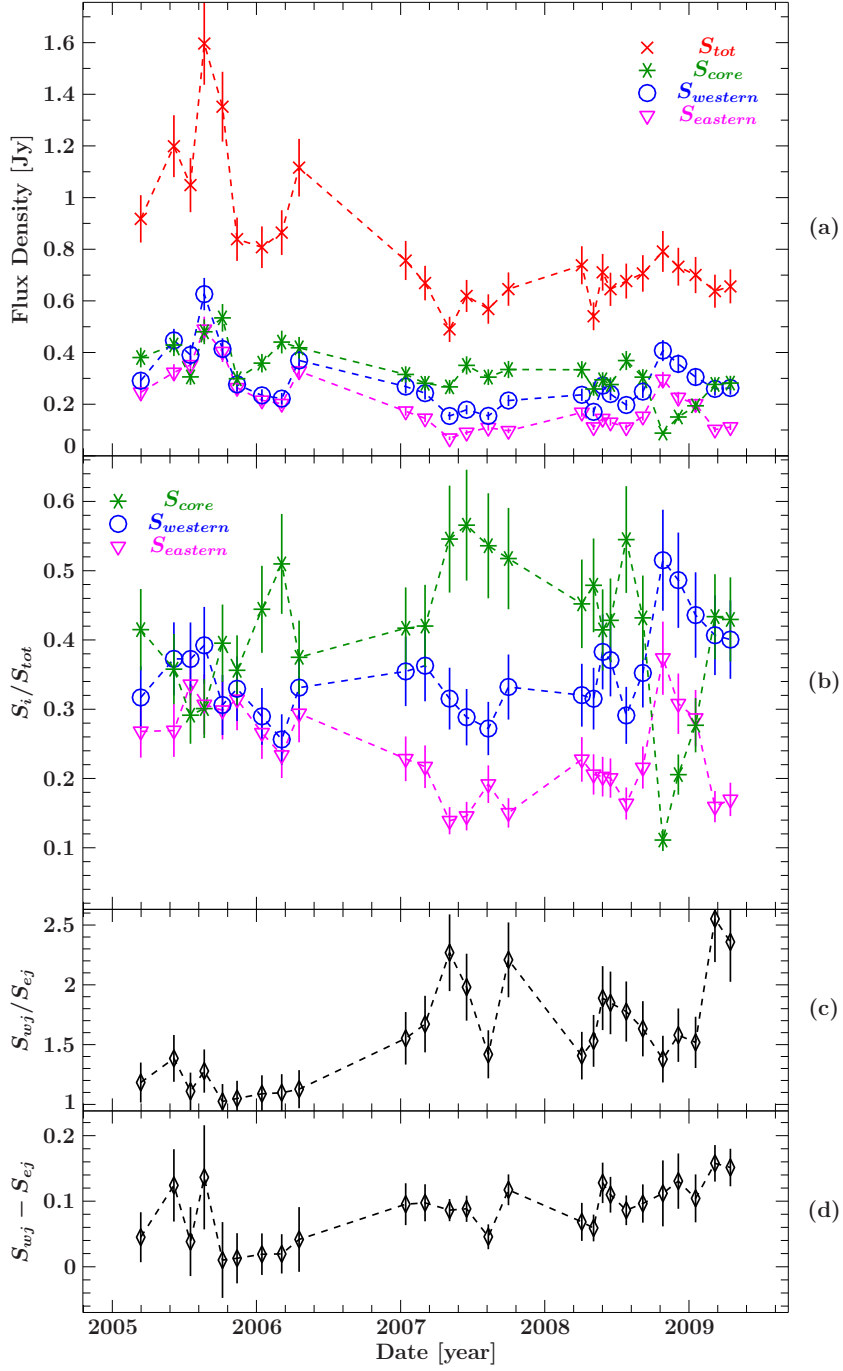


Figure 3.13.: (a) Light curve at 43 GHz of the total flux density (red), core flux density (green), western jet flux density (blue), and eastern jet flux density (pink); (b) fractional intensities (relative to total) of the core component (green), western jet (blue), and eastern jet (pink); (c) ratio of the western to eastern jet flux densities; and (d) absolute difference of the flux density of the western and eastern jet.

frequencies (see, e.g., Vermeulen et al. 2003) further constrains on the jet properties and formation can be made. The particles emitting at 43 GHz are assumed to be accelerated from regions of the accretion disk, which are closer to the SMBH. Finally, most likely an inner layer of the jet is observed. This would lead to a faster moving inner layer and a slower outer layer, which is not emitting at 43 GHz.

The physical conditions are getting more extreme when coming closer to the central engine. If the direct surrounding of the central SMBH has a larger impact at 43 GHz, this would explain the different behavior of the source at this frequency in comparison to lower frequencies. The energy conversion processes are more violent and disturbances can happen on shorter timescales.

Precession or asymmetric jet production?

As discussed in Sect. 3.3.2 the results do not fit into a simple picture in which the same intrinsic conditions can be assumed in both jets. There are two main possibilities capable of explaining this. First, jets are not intrinsically identical. Second, if β does not change, the flux density ratio only depends on θ_{LOS} . This would result in a change of θ_{LOS} over the four years of observation, implying a precessing jet.

The galactic X-ray binary SS 433 is an example of an precessing jet. The jet precession occurs within a cone of half-opening angle of 19.85° with respect to the angle to our line of sight of 79° with a period of 162 days (Margon & Anderson 1989). As larger scale counterparts to SS 433, radio galaxies have been observed to reveal helical motions as well. In particular, a considerable amount of quasars have S-shaped jets (for example 3C 273 Perley & Meisenheimer 2017 or 3C 345 Matveyenko & Sivakou 2013). There are several mechanisms leading to a precessing jet. One often discussed scenario is the Bardeen-Petterson effect, which is due to a misalignment of the angular momentum of the accretion disk and rotating central black hole (Bardeen & Petterson 1975). Based on this approach jet precession has been successfully described in several blazars (see, e.g., Liu & Melia 2002; Caproni et al. 2004). Typically very long precession periods are observed.

There is evidence for a recent merger event in NGC 1052 about 1-2 Gyrs ago (van Gorkom et al. 1986b; Pierce et al. 2005). Therefore, another likely explanation is a binary black hole, where the companion exerts a torque and therefore results in a precession of the accretion disk, resulting in shorter periods of precession.

There are many studies concerning jet precession (see for example Mohan et al. (2016); Machalski et al. (2016); Rozgonyi & Frey (2016) and references therein). Examples are 1308+226 with an orbital period of $\simeq 8.5$ yr in case of a binary black hole model (Britzen et al. 2017), 2MASXJ12032061+1319316 with a precession period of 0.95×10^5 yr (Rubinur et al. 2017), and M 81 with a period of 7.27 yr (Martí-Vidal et al. 2011). As well as the blazar OJ 287, showing outburst on an interval of about 12 years, which is consistent with a binary black hole model (Valtonen et al. 2008; Britzen et al. 2018).

If the jets are initially asymmetric the question arises as to which mechanism is able to produce this behavior. One possible physical scenario is connected to the magnetic field structure in the surrounding disk that is accreted by the black hole. Assuming there are several small-scale magnetic field loops with alternating polarity (Parfrey et al. 2015; Contopoulos et al.

2018).

For example assuming a magnetic field configuration in the disk consisting of four magnetic field loops: two loops in the northern hemisphere of the disk and two in the southern hemisphere with alternating polarity. Here we assume the disk being oriented along in the East-West plane, which is about 90° rotated to the orientation expected for NGC 1052. In this picture the jets are oriented to the North and the South. During the accretion of the innermost loops, the magnetic field opens up because of the differential rotation and leads to a poloidal magnetic field with different polarity in the northern and southern hemisphere (see, e.g., Fig. 1 in [Parfrey et al. 2015](#)).

Furthermore assuming that the polarity in the northern jet is different from the accreted polarity in the northern hemisphere of the accretion disk, the ongoing accretion pushes magnetic field lines of different polarity closer and closer together. This leads to a reconnection event and disrupts or turns off the northern jet for some time until it is established again. On the other hand there is no difference in the polarity in the southern hemisphere, i.e., the southern jet and the accreted loop have the same polarity. Therefore no reconnection event occurs that disturbs the jet. The situation is flipped in the accretion of the next magnetic loop pair, i.e., the northern jet is unperturbed while the southern jet is disrupted. Within such a scenario asymmetric jets with varying outflow can be produced.

A detailed study of the magnetic field in the region of the central engine in NGC 1052 could shed light on whether this could be an explanation for the observed asymmetry. Until now, it was only possible to derive estimates on the mean magnetic field in the central region (compare Sect. 5). However, there is no linear polarization data that would allow to infer the geometry of the magnetic field in NGC 1052. Future millimetre-VLBI observations may be able to trace changes in the source magnetic field.

Even without detailed knowledge of the magnetic field geometry in NGC 1052 this study favors an asymmetric jet production. Subtracting the influence of the absorbing torus higher flux density values are expected for the western jet close to the central engine as compared to the eastern jet. On the other hand there is a clear trend toward higher velocities in the eastern jet. These observations fit very well into a picture in which the western jet carries a larger internal energy and/or magnetic flux than the eastern jet, thus becoming brighter at these scales. Simultaneous multi-frequency observations will allow for studying in detail absorption mechanisms, external and internal, along both jets, thus probing the local magnetic field distribution.

3.4. Using evolutionary algorithms to model relativistic jets

My results from the multi-epoch data at 22 GHz and 43 GHz were used as input to model relativistic jets using evolutionary algorithms. Here, I will shortly describe the setup of the simulations and our results, published in [Fromm et al. \(2019\)](#).

The dynamics of the jets in NGC 1052 are modelled using relativistic hydro-dynamical (RHD) simulations and their radiative signature is obtained via special relativistic radiative transfer (SRRT) calculations. To compare the observed images with the numerical models we computed synthetic images taking into account a realistic array configuration (here the VLBA), the sparse sampling of the brightness distribution, as well as the image reconstruction algorithms.

VLBI images consist of several discrete emission features and artefacts due to the imaging process, which is difficult to model with numerical simulations. To overcome this problem, we used the stacked VLBA images at 22 GHz and 43 GHz to constrain parameters of the simulation as average jet structure and reliable jet features. Stacked images have the advantage of a more continuous jet emission, which is easier to compare with steady-state jet simulations.

3.4.1. Simulation setup

We performed 2D axisymmetric RHD simulations of jets within a decreasing pressure ambient medium (details on the numerical setup can be found in [Fromm et al. 2018](#)). Within our studies we investigated two different initial conditions at the jet nozzle: pressure-matched (PM) and over-pressured (OP) jets. In the case of PM jets there is a transversal match between the pressure in the jet and the ambient pressure. This setup leads together with the decreasing pressure in the ambient medium to a nearly featureless conical jet. On the other hand in OP jets, the pressure in the jet is larger than in the ambient medium, which leads to a pinching jet and the formation of recollimation shocks.

As soon as a steady state is reached, a torus is added (modelled as described in [Fromm et al. \(2018\)](#)), which acts as an absorber of the non-thermal emission. Figure 3.14 shows the 2D rest-mass density distribution for the PM and the OP jet. Both jets propagate east- and westwards and the torus is oriented in North-South direction. The lower panels give a cut along the jet axes, revealing a continuously decreasing distribution in case of the PM jet and the formation of shocks for the OP jet model, seen as local maxima at $r = 15 R_j$ and $r = 40 R_j$.

Since the special relativistic hydro-dynamical (SRHD) simulations do not include the non-thermal particles responsible for the observed synchrotron emission, we reconstruct their properties from the evolved thermal ones (these are the ones included in the simulations).

The simulations are meant to be compared to real VLBI images and spectra over several radio frequencies (from 1.4 GHz up to 230 GHz), hence, the jets span over various scales. Whereas the innermost jet formation and collimation region is revealed at high frequencies, low-frequency images test areas which are a few tenth of mas (corresponding to a few parsecs) away from the central engine. To cover all relevant areas with enough numerical resolution and still stay computational reasonable, adaptive non-linear grids are used, which have a high resolution at the jet apex and enough resolution further out.

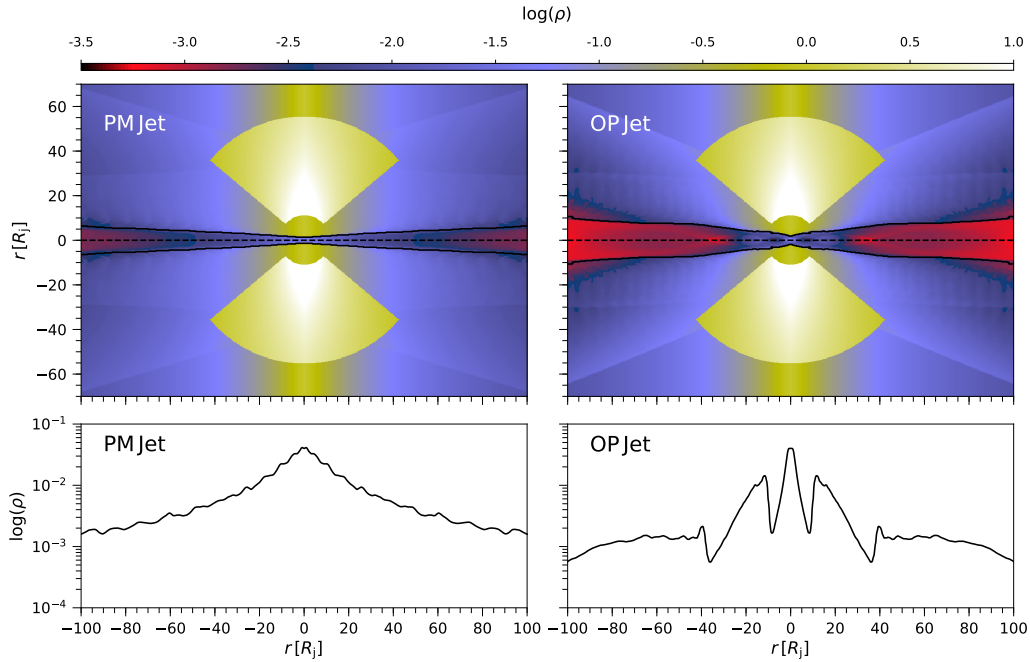


Figure 3.14.: Rest-mass density distribution for PM (left) and OP (right) jet. *Top:* Torus towards North and South and jets emanating east- and westwards. *Bottom:* Density profile along the jet axis (marked by a dashed line in the upper panels).

Finally, synthetic observations are calculated from the emission simulation to obtain an image which is comparable to typical VLBI images. Meaning, the brightness distribution is sampled with the projected baselines of the VLBA, followed by hybrid imaging in DIFMAP.

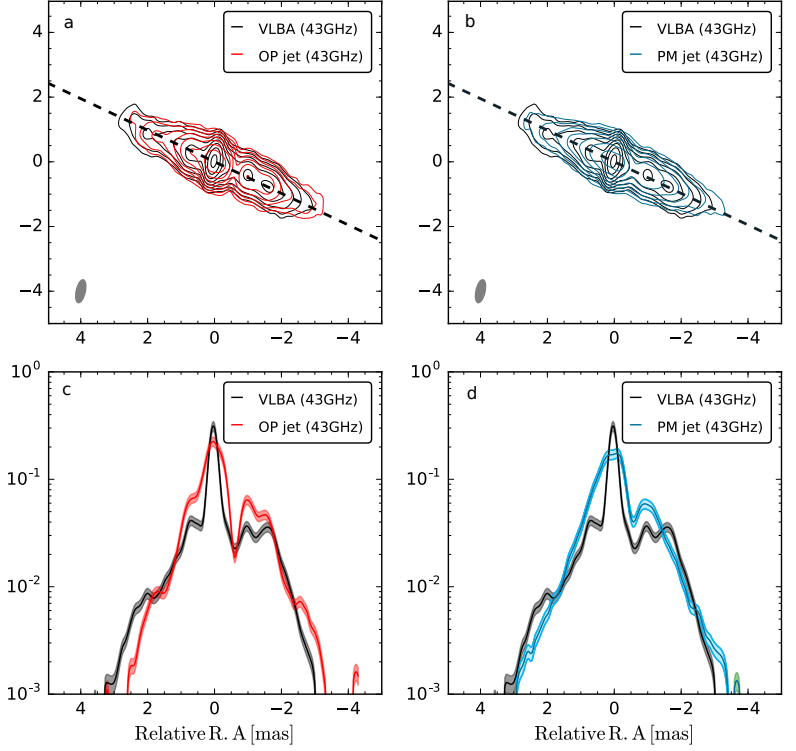
The final synthetic maps not only are compared to the true VLBA stacked images in the end, but properties of the observations are used to guide the optimisation process during the simulation. Among other things, the number of local flux density maxima along the jet and the properties of the emission gap from VLBA observations are used. For the optimisation a generic algorithm and particle optimisation is used (for further details on the optimisation see [Fromm et al. 2019](#); [Engelbrecht 2007](#)).

3.4.2. Results from the the simulations

As already suggested before, the PM jet is continuously decreasing, whereas the OP jet produces recollimations shocks, seen as features with enhanced brightness (compare Fig. 3.14). Figure 3.15 plots the resulting contour maps from stacked VLBA images and simulated images as well as cuts along the jet axis. The OP profile along the jet axis reveals a plateau-like feature similar to the 43 GHz VLBA stacked image at ± 2 mas. The emission gap is nicely reproduced, decreasing with increasing frequency (see Fig. 3.16).

To improve the simulations, a refined SRHD model for the OP jet is simulated by re-running the optimisation procedure using the values found in the previous run. A random scatter was

Figure 3.15: The upper panels (a and b) show 43 GHz contour maps for the stacked VLBA image (black) and the simulated image (red for OP jets and blue for PM jets). The beam is plotted in the lower left corner. The contours start at 1 mJy and increase by factors of 2. Panels c and d give the flux density profile along the jet stream line (black dashed line in upper panels). Based on Figure 6 in [Fromm et al. \(2019\)](#).



added to the initial position in order to avoid a bias. The local flux density maximum at 2 mas is fitted more consistently with the observations for the refined model. The OP jet models the VLBA images more consistently. However, with the current observations it is difficult to distinguish between both models.

Hence, the simulation results are extended to 86 GHz GMVA and 22 GHz RadioAstron observations. Both approaches have the advantage of an increased resolution. Additionally, the models at 86 GHz are not affected by external absorption and allow a direct view onto the innermost region around the central engine. For both approaches, synthetic images were produced by reconstruction using the maximum entropy method (MEM) provided by the EHTim package. The results for both, RadioAstron and GMVA are shown in Fig 3.17.

In case of the RadioAstron image the emission gap is as pronounced as for typical VLBA maps. There are no features to distinguish between both jet models. The GMVA maps, on the other hand, reveal clear differences between OP and PM jets. While peering through the absorbing structure, the impact of both models on the innermost region can be studied. In the PM model the flux density falls continuously towards the East and the West of the central brightness maximum. Only the OP model reveals a local flux density maximum at ± 0.5 mas, which can be identified with components at ± 0.4 mas, reported in [Baczko et al. \(2016a\)](#).

Finally there are several features that are well reproduced. For example, the extent of the torus, the location of the emission gap and the distribution of the flux density and spectral index. Based on the values obtained from the optimisation the calculated number density of $0.7\text{--}1.0 \times 10^{22} \text{ cm}^{-2}$ in the torus is consistent with values reported by, e.g., [Kadler et al. \(2004b\)](#). However, both models are not able to reproduce the faster decrease of the flux density in the western jet. A possible explanation for this deviation are asymmetries in the ambient

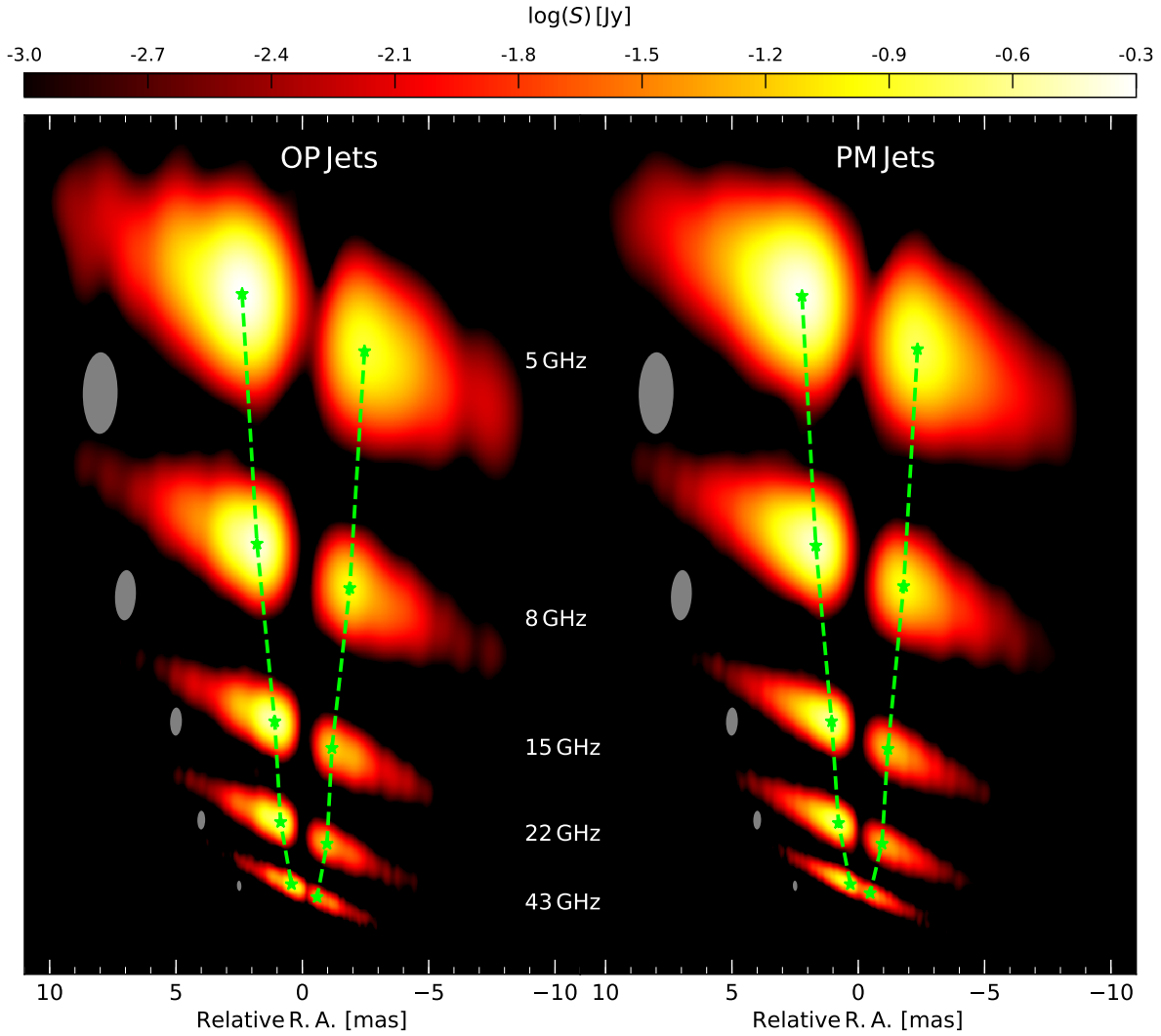


Figure 3.16.: Synthetic VLBA images from 5 GHz to 43 GHz computed in [Fromm et al. \(2019\)](#). On the left the OP jet model is shown and on the right the PM jet model. The convolved beams are plotted left beside the images. The intensity of the images start at 1 mJy. Images had been aligned on the center of the emission gap. The position of the core, the flux density maximum, is marked by a green star in each map. Over the frequency the locations of the stars are connected by dashed lines. Based on Figure 10 in [Fromm et al. \(2019\)](#).

medium and/or the jet launching.

The conclusions from the simulations can be summarized as follows: the jets in NGC 1052 are best modelled by a slightly over-pressured jet in a decreasing-pressure ambient medium. This is best visible in the case of synthetic 86 GHz maps as observed with the GMVA.

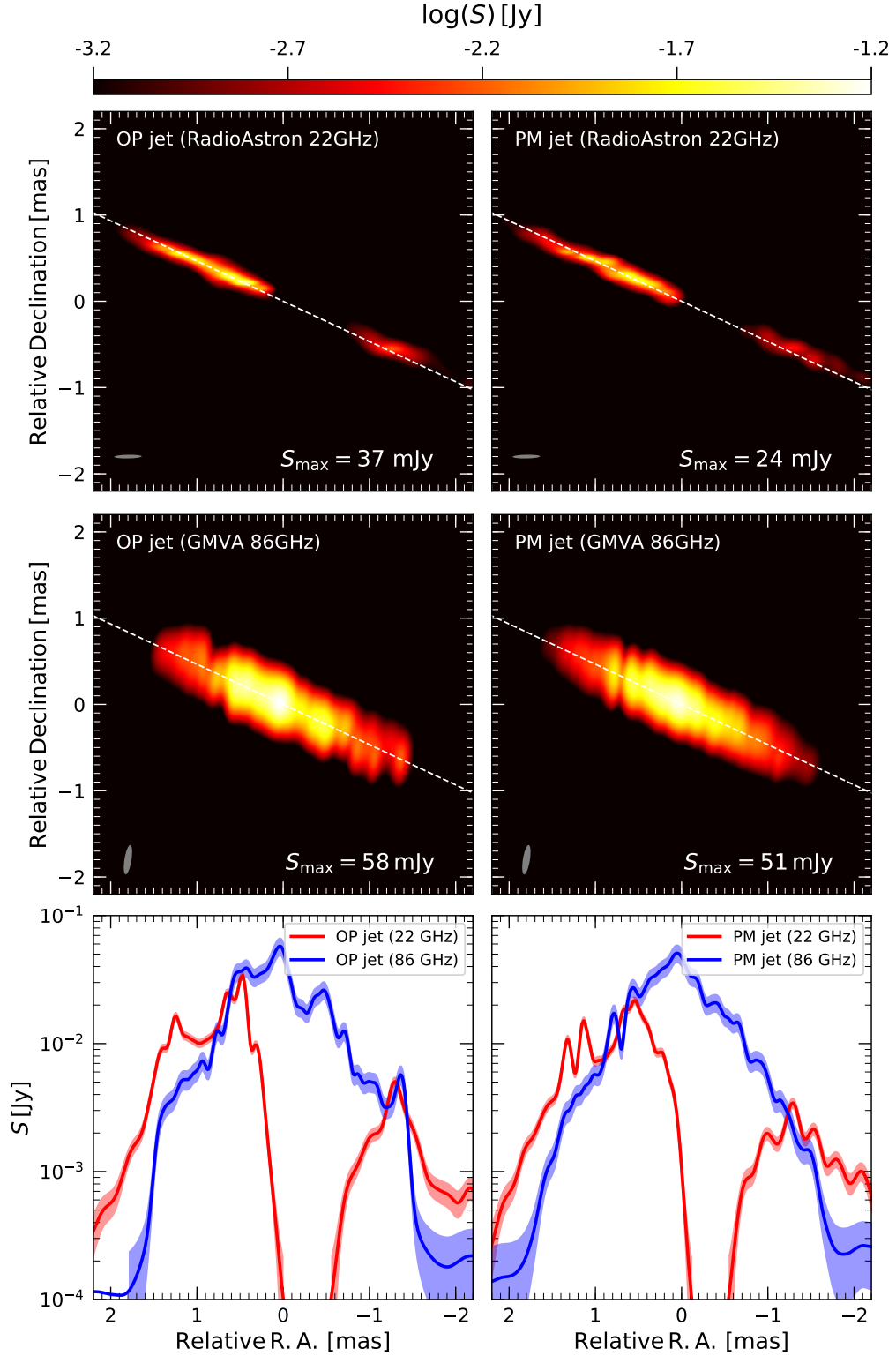


Figure 3.17.: Synthetic images as seen by RadioAstron at 22 GHz (*top panels*) and by the GMVA at 86 GHz (*middle panels*) for OP (*left*) and PM jet (*right*). The beam is plotted in the lower left corner of each map. The *lower panels* show the flux density along the dashed line in the upper panels corresponding to the jet axis. This figure is based on Fig. 13 and 15 in [Fromm et al. \(2019\)](#).

3.5. Conclusions

In this chapter I present a detailed VLBI analysis of NGC 1052 involving twenty-nine epochs from 2005 to 2009 at 22 GHz and 43 GHz.

1. In early 2007 the morphology of the source changes from symmetric to asymmetric with the western jet becoming brighter. Moreover, the flux density ratio of the western to eastern jets varies between $R = 1.1$ and $R = 2.5$.
2. A kinematic analysis of the evolution of the various jet components results in mean apparent jet velocities of $\beta_{\text{wj}} = 0.343 \pm 0.037$ and $\beta_{\text{ej}} = 0.529 \pm 0.038$ for the western and eastern jets, respectively. Compared to previous estimates at lower frequencies (Vermeulen et al. 2003; Lister et al. 2013) the apparent jet speeds derived in this work are faster, especially for the western jet.
3. Besides the extended jet emission, one central bright emission region is present in all observed epochs. Based on the kinematic analysis this central feature is likely the dynamic center of the system.
4. Combining the flux density evolution and kinematics, the parameter space of the intrinsic velocity and viewing angle was explored. There was no consistent parameters for all observations, which points toward asymmetric jet production.
5. I analyzed the spectral properties of the source morphology between 22 GHz and 43 GHz. It reveals an optically thick region to the west of the brightest jet feature at 22 GHz with a diameter of around 1.5 mas (0.15 pc). The absorption seems to be caused by a torus around the central engine which is perpendicular to the twin-jet system. Both jets are optically thin with spectral indices $\alpha \leq -1$.
6. Power laws were fit to the distribution of brightness temperatures and jet diameter as a function of the separation from the center. The expansion is similar for both jets, leading to a well-collimated structure, which evolves starting at around 1 mas, with a power-law index of $d = 0.65$.
7. The brightness temperature values in the western jet drop at 1 mas separation to the center. This is well explained by a reduction of the flux density owing to absorption in the torus.
8. A faster inner layer is proposed that is fed from a region closer to the central engine, as observed at 43 GHz, and a slower moving outer layer, which has particles that come further outward from the accretion disk, as observed at lower frequencies.
9. These observations fit very well into a picture in which the western jet carries a larger internal energy and/or magnetic flux than the eastern jet, thus becoming brighter at these scales.

10. The stacked 22 GHz and 43 GHz images had been used for modelling relativistic jets using evolutionary algorithms (Fromm et al. 2019). It was shown, that the jets are best modelled by a slightly over-pressured jet in a decreasing-pressure ambient medium.

Further studies at 43 GHz are needed to test the observed asymmetry on longer timescales. As an observation at 86 GHz resulted in a similar morphology (Baczko et al. 2016b), simultaneous observations up to the highest achievable radio frequencies would allow to perform the core-shift analysis and spectral index measurements up to even higher frequencies. This will result in a more complete picture of the twin-jet system in NGC 1052 and would give the chance to test current jet formation models.

4 | Multi-frequency observations of NGC 1052

To investigate deeper the source asymmetry of NGC 1052 as described in chapter 3, additional frequencies were used. This includes observations at six frequency bands between 1.5 GHz and 43 GHz with the VLBA, at 86 GHz with the GMVA, and at 22 GHz with a global array including RadioAstron.

This chapter is organized as follows: 1) Discussion of data reduction of the RadioAstron and multi-frequency VLBA observations. 2) Results from the multi-frequency VLBA observations. 3) Outcome of the RadioAstron observations. 4) Comparison of the RadioAstron and multi-frequency VLBA observations. Additional figures and tables are moved in the appendix B to enhance readability.

4.1. Data reduction

4.1.1. Multi-frequency VLBA observations of NGC 1052

NGC 1052 was observed with the VLBA on April 4, 2017 at 1.5, 5.0, 8.4, 15, 22, and 43 GHz. The data were recorded with the Roach Digital Backend (RDBE) at dual polarization with eight sub-bands per polarization with a bandwidth of 32 MHz and a data rate of 2 Gbps. The correlation was performed at the National Radio Astronomy Observatory (NRAO) at the Array Operation Center of the VLBA in Socorro, NM, USA.

For data reduction the standard procedure described in Sect. 3.1 was applied with small alterations. For all six observations the improvement resulting from opacity fitting was checked and finally applied to the data. However, the fitting turned out to only have a significant impact at higher frequencies starting at 22 GHz. Therefore, it would be valid to neglect opacity corrections for lower frequencies. The correction factors derived by the AIPS task APCAL revealed a few unphysical values from corrupted T_{sys} data. These were removed by applying a smoothing function in AIPS. The fringe fitting calibrator source 3C 454.3 was used to correct for the bandpass shape over the frequency bands, excluding the outer channels in each sub-band (IF). After solving for residual delays and rates, the final cross-correlation spectra revealed persistent slopes and jumps over IFs for a subset of antennas. This was corrected by an additional manual phase-cal. The science target NGC 1052 shows a lot of structure, therefore the standard phase-calibration may not work perfectly as it assumes a point-like source while fringe fitting. To overcome this problem, a preliminary map of NGC 1052 for all frequencies was produced in DIFMAP using the calibrated data. The resulting clean model was then used as input model for FRING while repeating the fringe fitting procedure for NGC 1052.

Figure 4.1 visualizes the difference of the calibrated visibility phase before imaging in DIFMAP when using the standard calibration procedure, or when using the preliminary CLEAN model as input model for FRING in case of the C-band data. Shown is the visibility phase versus uv -distance projected along a jet position angle of 64° . The data were averaged over 20 s, but no self-calibration or flagging was applied. Hence, the visibility phase is already better calibrated before the imaging process and there was no need to use the procedure *startmod* in DIFMAP. With the standard settings *startmod* applies a self-calibration assuming a point source starting model with a flux density of 1 Jy at the phase center. Obviously, this kind of model is not the best choice in case of structured sources as NGC 1052. If applying *startmod* to the final data, a visibility phase according to the left plot in Fig. 4.1 would result.

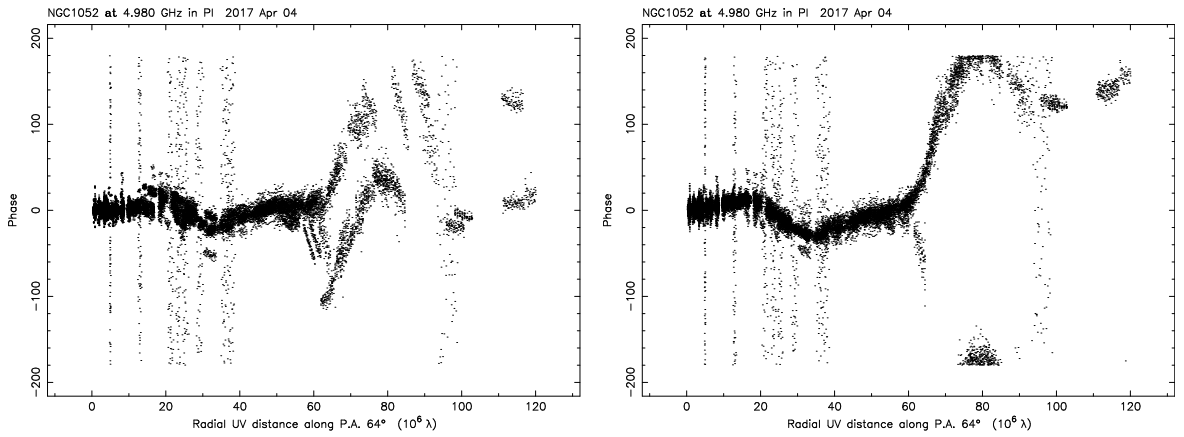


Figure 4.1.: Raw visibility phase versus uv -distance projected along a jet position angle of 64° for the VLBA C-Band observation without any self-calibration applied, averaged over 20 s. (*Left:*) standard calibration procedure; (*Right:*) Using the preliminary map of NGC 1052 as input clean model for FRING.

Afterwards the CLEAN algorithm in DIFMAP was used for imaging the final calibrated data of NGC 1052 (Compare Fig. 4.2). The observing plan (schedule) was designed to obtain images with similar noise level to be compared in the best possible way. The parameters of the naturally weighted maps are listed in Table 4.1. The noise levels are between 0.54 and 1.20 m Jy beam $^{-1}$ and therefore the scheduling strategy was successful. The final images (compare Fig. 4.2) are similar regarding the quality (with a dynamic range between 2030:1 and 6010:1) and therefore easy to compare. Based on the discussion in Sect. 3.1, uncertainties on the obtained fluxes of 10% were assumed.

Analogously to Sect 3.1, the source structure of NGC 1052 was parameterized by 2D circular Gaussian components in DIFMAP fitted to the interferometric visibilities. Only one feature was fitted with an elliptical Gaussian component in the western jet at 5 GHz. Uncertainties of model-fit components were estimated as described in Sect. 3.1.

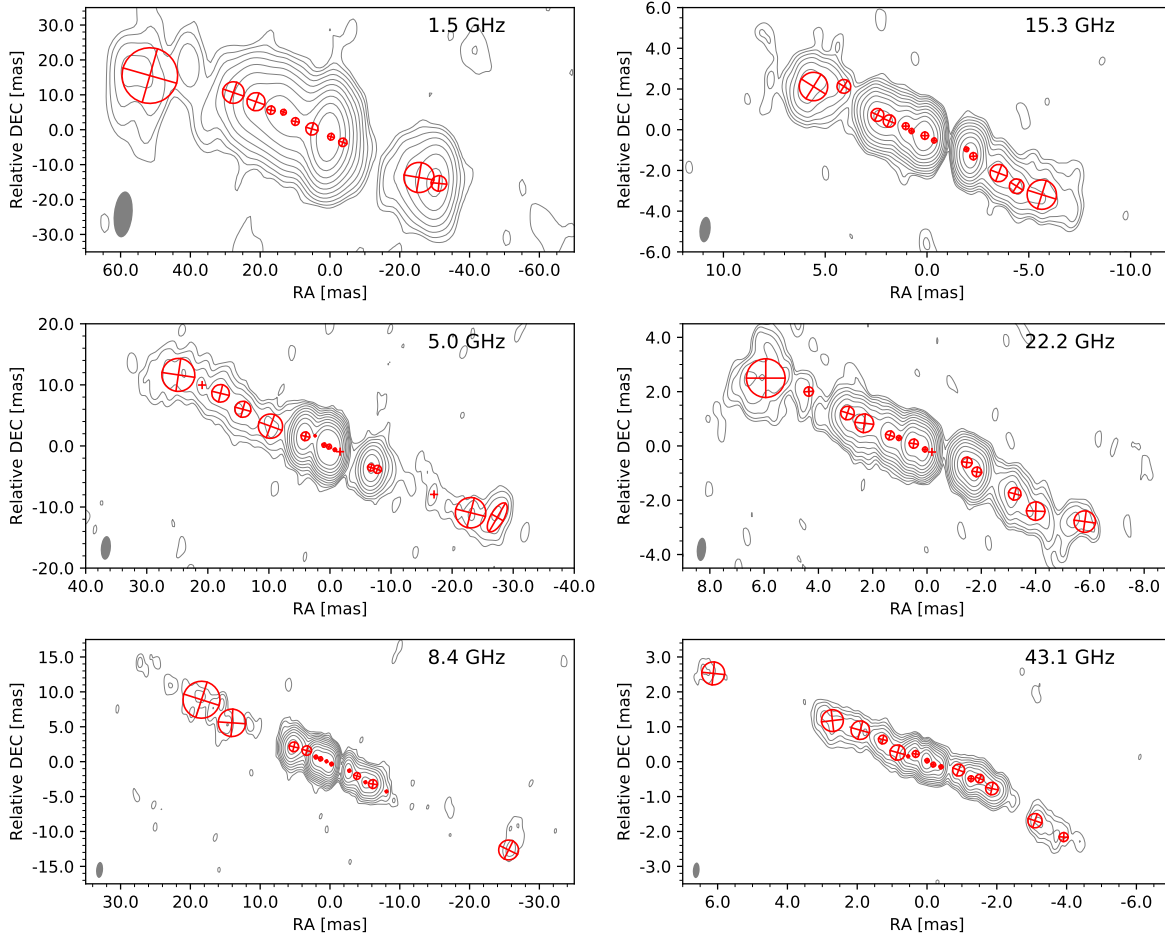


Figure 4.2.: Final clean images at all six frequencies (see image parameters in Tab. 4.1) with Gaussian model components plotted on top. The contours start at 4, 4, 4, 3, 2, and 3 times the noise level for L, C, X, U, K, and Q band, respectively and increase logarithmically by factors of 2. Parameters from the Gaussian model fitting are listed in Tab. B.1.

4.1.2. RadioAstron observation of NGC 1052

Correlation

In contrast to the VLBA observations discussed in the previous sections, the correlation of the RadioAstron experiment was done at the DiFX software correlator in Bonn¹. I carried out large parts of the correlation under the supervision and guidance of Dr. Gabriele Bruni (at this time responsible for RadioAstron correlation at MPIfR). In the following I will shortly describe the peculiarities of this correlation process.

The observation was performed with RadioAstron and a large ground array consisting of antennas from the VLBA, VLA, EVN, and LBA on November 5, 2016 at 22 GHz. The Sardinia radio telescope was able to join the observation, what added a high-sensitivity dish to the array.

¹<https://www.mpifr-bonn.mpg.de/771785/DiFX-CORRELATOR>

Table 4.1.: Image parameters for all analyzed VLBA observations from April 4, 2017 with natural weighting.

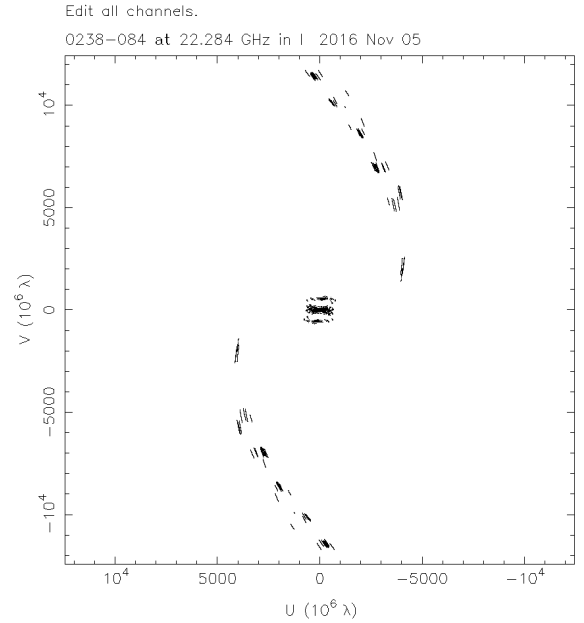
Band	Frequency [GHz]	RMS ¹ [$\frac{\text{mJy}}{\text{beam}}$]	S_{peak} ² [$\frac{\text{Jy}}{\text{beam}}$]	S_{tot} ³ [Jy]	b_{maj} ⁴ [mas]	b_{min} ⁵ [mas]	PA ⁶ [°]	DR ⁷
L	1.5	0.073	0.320	0.615	13.22	5.37	−5.85	2030:1
C	5.0	0.054	0.458	1.036	3.89	1.65	−4.99	6010:1
X	8.4	0.067	0.336	1.121	2.30	0.99	−4.95	5210:1
U	15.3	0.063	0.238	0.824	1.26	0.55	−6.32	4920:1
K	22.2	0.081	0.171	0.802	0.86	0.34	−4.95	2230:1
Q	43.1	0.096	0.144	0.588	0.45	0.19	−4.37	3630:1

¹ Root-mean-square noise level of image ² Peak flux density

³ Total recovered flux density ^{4,5,6} Major, minor axes and major axis position angle of the restoring beam ⁷ Dynamic range: ratio between the map peak and the rms inside a CLEAN window far away from the source structure

The final set of telescopes was very heterogeneous. The individual telescopes had different frequency setups, therefore so called zoom-bands had to be used in order to combine all telescopes during correlation and resulted in a different frequency coverage for different antennas (and their baselines). This was the case for VLBA, VLA, and LBA.

Figure 4.3: Full (u, v) coverage of the RadioAstron observation of NGC 1052 at 22 GHz. The most distant (u, v) points are baselines including RadioAstron, with the shortest and longest baselines are equal to 4 and 11 earth diameters, respectively. There were no fringes detected to RadioAstron.



The standard fringe fitting software for a RadioAstron experiment at correlation stage is FOURFIT (Haystack Observatory processing software HOPS²), which fits for delay and delay rate, as well as multi-band delay. The last one is not needed for a typical VLBI experiment.

²<https://www.haystack.mit.edu/tech/vlbi/hops.html>

The process of fringe finding at correlation stage is very similar to that during calibration in AIPS. If possible a scan of a strong calibrator source is used to correct for all antennas, switching reference antennas if needed. For this experiment the sources 4C+28.07 (0234+285) and 3C 454.3 (2251+158) were used. An example output plot of FOURFIT for the baseline ATCA-Hobart is presented in Fig. B.7. After all ground telescopes had been solved for delays and rates, and corrected accordingly, no fringes to RadioAstron were found. Additional attempts by using PIMA (Petrov et al. 2011) also did not lead to a significant fringe detection. There are two main reasons that can explain the non-detection of RadioAstron baselines: 1) There is a large gap of ~ 4 earth diameter between ground-ground and ground-space baselines which reduces the SNR of possible fringes and 2) As is seen at other 22 GHz images, NGC 1052 has a complex extended structure with a size of up to 20 mas. The typical fringe finding procedures expect a point-like structure and have difficulties in deriving delays and rates for complex sources as NGC 1052. Even after including the ground-array structural information of the source in the fringe search, this was unsuccessful (see below). The final correlator output therefore includes RadioAstron without any correction applied and twenty-nine antennas on ground. The (u, v) -coverage after correlation and before any further calibration or flagging is shown in Fig. 4.3.

Calibration and Imaging

The standard procedure to calibrate an experiment including RadioAstron is to first process the whole ground array and to search afterwards for fringes to the orbiting antenna having the advantage of an *aligned* (equivalent to *phased*) ground array. The calibration of this dataset was challenging due to several peculiarities, as shown below. To ease the calibration and to be able to test different approaches, I wrote a set of Python scripts to automate VLBI calibration in AIPS as much as possible. AIPS is written in FORTRAN and new tasks would be needed, which can be avoided by using external python scripts, for which the Python interface to AIPS called PARSELTONGUE (Kettenis et al. 2006) is used. It allows to combine already existing tasks with additional, external programs. For more information, see Appendix C.1.

As mentioned above, the experiment includes several different frequency setups and bandwidths shown in the cross-correlation spectrum for several baselines: Figure 4.4 shows six example spectra of uncalibrated visibility phase and amplitude over the eight frequency bands. Baselines including LBA antennas have only four sub-bands (IFs), whereas baselines between European and VLBA antennas cover all eight sub-bands. As a result the calibration has to be planned with care sequentially, in order to not lose parts of the visibility data by applying non existing sub-band solutions to observed sub-bands. For example calibrating Effelsberg with reference to Ceduna would delete half of the sub-bands for other baselines to Effelsberg as Ceduna only has visibility data for IFs 1 to 4. As a result, manual phase calibration to align offsets between the individual IFs was done in several steps.

To improve the phase-calibration, the same procedure was followed as for the VLBA multi-frequency observations. After initial calibration a rough map of the data was produced to serve as input model for an additional round of FRING for the target source NGC 1052. As a last step, the finally calibrated ground-array and the rough map was used to attempt fringe detection to the still uncorrected RadioAstron. However, also at this stage no fringes were detected.

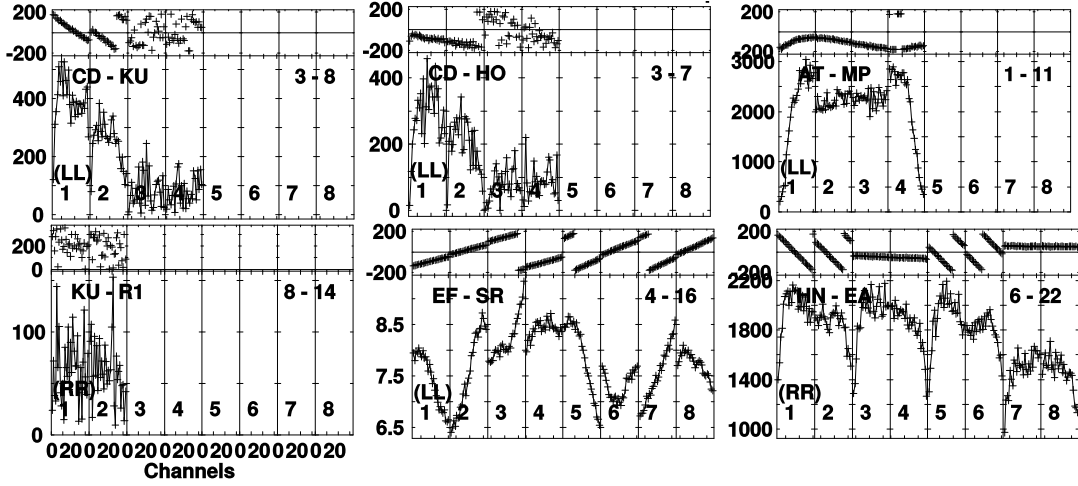


Figure 4.4.: Selected cross-spectra (visibility phase (top) and amplitude (bottom)) as a function of frequency channel (width of) for the eight available subbands of RadioAstron observation of NGC 1052 prior to calibration, produced by the task POSSM in AIPS. Baselines including CD: Ceduna, KU: KVN Ulsan, HO: Hobart, AT: ATCA, MP: Mopra, R1: RadioAstron, EF: Effelsberg, SR: Sardinia, HN: Hancock, EA: VLA. The plot shows different scans.

The use of zoom-bands during correlation resulted in offsets in the visibility amplitude for baselines to LBA antennas (see for example baseline upper left panel in Fig. 4.4). In addition there are untypical slopes and offsets for visibility amplitudes for some baselines and time ranges (e.g. Fig. 4.4 bottom middle panel). To correct the bandpass shape the task BPASS was used.

After global fringe fitting there remained offsets between IFs for a few baselines and scans only for individual sources. The observation was spanning about 17 hrs and it turned out, that the offsets between IFs were not stable over the whole observation. This offset was corrected for by additional manual fringe fitting for single IFs for each affected source, baseline and scan range individually at the end of the calibration. Finally, the data were split and read out into DIFMAP for hybrid imaging.

The changes of the visibility amplitude over the eight sub-bands as well as not perfectly calibrated values for a subset of antennas due to insufficient system temperature T_{sys} information required a few alterations with respect to the standard imaging procedure as described for VLBA observations. I assumed the VLBA to have the most accurate estimation of amplitudes. Therefore as first step a VLBA-only clean image was produced in DIFMAP. The final model was used to correct the amplitudes of the individual telescopes by using GSCALE in DIFMAP, which applies an amplitude self-calibration. The calibration of the amplitudes for all problematic telescopes had been done in several steps. For each step only a subset of telescopes were corrected, a new CLEAN model was created at each step, which then served as input model for amplitude self-calibration of the next subset of telescopes. The final natural weighted clean map is shown in Fig. 4.5. Thanks to the large ground array it is the highest resolution image at 22 GHz of NGC 1052 until now with a dynamic range of 3630:1, which is improved compared to the VLBA only 22 GHz image presented in Sect. 4.1. The inclusion of Southern stations

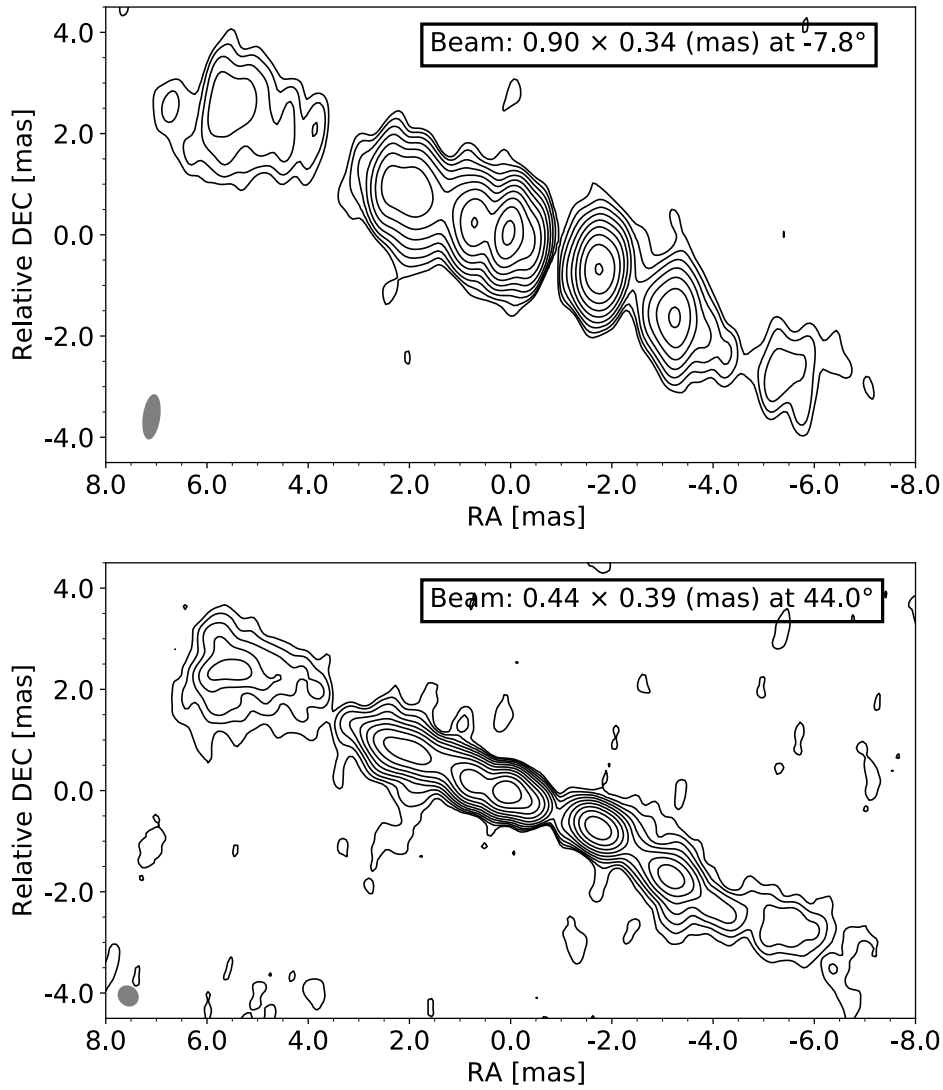


Figure 4.5.: Naturally weighted CLEAN contour map of RadioAstron observation of NGC 1052 at 22 GHz in November 2016. Contour lines for both images begin at four times the noise level and increase logarithmically by factors of 2. Upper map based on VLBA and VLA visibilities (dynamic range of 2250:1), lower map includes all successfully calibrated data (dynamic range of 3630:1). The improvement of resolution by adding Southern telescopes is visualized.

enhanced the North-South resolution with a nearly circular beam of 0.443×0.392 (mas) at a position angle of 44° . All parameters of the final CLEAN map as well as a CLEAN map based only on VLBA and VLA are listed in Tab. 4.2. As mentioned above, I tried to correct for the large offsets of the amplitudes from different telescopes by adjusting the visibility amplitude of the whole array based on a VLBA only map. Still, there is a difference in the total flux density between the VLBA+VLA image (607 mJy) and the image including the whole array (423 mJy). Hence, the visibility amplitude of this observation still has a large uncertainty.

On the other hand, the image fidelity of the final RadioAstron ground array image is with a dynamic range of 3630:1 improved in comparison to the VLBA only image from April 2017 (2230:1).

Table 4.2.: Image parameters for RadioAstron observations from November 5, 2016 at 22 GHz with natural weighting for array including VLBA+VLA and the full ground-array.

Array	Frequency [GHz]	RMS ¹ [$\frac{\text{mJy}}{\text{beam}}$]	S_{peak} ² [$\frac{\text{Jy}}{\text{beam}}$]	S_{tot} ³ [Jy]	b_{maj} ⁴ [mas]	b_{min} ⁵ [mas]	PA ⁶ [°]	DR ⁷
VLBA+VLA	22	0.082	0.158	0.607	0.90	0.34	−8	2250:1
full ground	22	0.035	0.106	0.423	0.44	0.39	44	3630:1

¹ Root-mean-square noise level of image ² Peak flux density ³ Total recovered flux density

^{4,5,6} Major, minor axes and major axis position angle of the restoring beam ⁷ Dynamic range: ratio between the map peak and the rms inside a CLEAN window far away from the source structure

4.2. Results of the multi-frequency VLBA observation of NGC 1052

4.2.1. Image alignment

In order to compare all images pixel-wise and to be sure that the same regions are taken into account for continuum spectral studies, these have to be aligned. There are two basic approaches to follow: 1) a 2D-cross-correlation of the optically thin regions of the images; 2) aligning on Gaussian model-fit components. The innermost region of an AGN jet is typically optically thick and most likely not the same region is observable at each frequency. Therefore, an optically thin region has to be used for the alignment procedure. From previous studies of NGC 1052 an optically thick structure is to be expected around the central region, covering the innermost areas around the central engine and resulting in an emission gap between both jets. The size of the gap is frequency dependent. Therefore, only areas in the images can be used that do not suffer from these absorptions. When aligning based on model-fit components, only optically thin features should be taken into account. In the case of the 2D-cross-correlation a mask has to be applied to the image in order to exclude the areas which are not optically thin.

In order to align the images I wrote a small python script (making use of the SCIKIT and EHTIM packages [van der Walt et al. 2014](#); [Chael et al. 2016, 2018](#)). More information on the scripts can be found in appendix C.2. A 2D cross-correlation in Fourier space was done pair-wise with adjacent frequencies. This works as long as both images have the same beam size, pixel scale, and map size. The best result is achieved by restoring both images with the largest map size and smallest pixel scale (in order to not loose any information) and the larger beam size (to not over-resolve the images). Therefore, the pixel parameters of the higher frequency image and the beam parameters of the lower frequency image were used for each alignment step. To not align on noise structures and to improve the sensitivity of the cross-correlation to recovered jet structure I used as input images the convolution of CLEAN model components

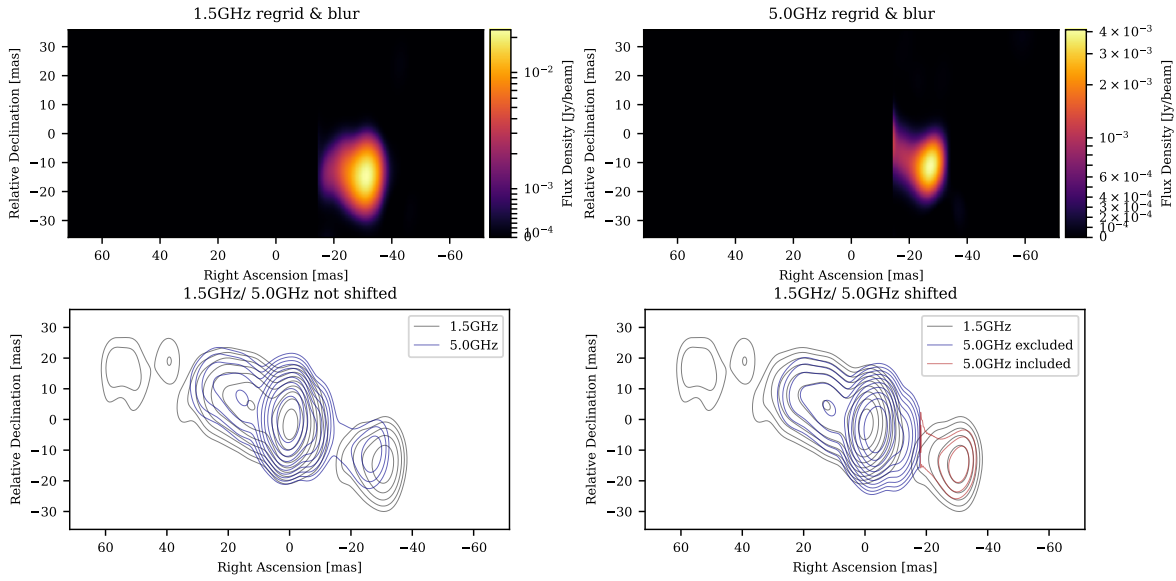


Figure 4.6.: (Top) images of the CLEAN model convolved with CLEAN beam, with a mask applied for 1.5 GHz (left) and 5 GHz (right). Including the eastern jet emission resulted in an unphysical small shift. Hence a mask was used to cut out the whole eastern jet and to only account for the emission of the western jet for the alignment. (Bottom) Contour maps without (left) and with applied shift (right). The red contours illustrate the region of the 5 GHz image used for the cross-correlation.

and the CLEAN beam. Several masking approaches have been tested, excluding differently shaped areas of both images. The best results were obtained by excluding an elliptical region with the position angle of the beam and the center shifted slightly towards the western jet. The alignment of the 1.5 GHz and 5 GHz images using this mask was not satisfactory, but a mask leaving only the area to the right of -20 mas in RA, hence the western jet, resulted in a trustworthy alignment. The final shifts are listed in Tab. 4.3.

Table 4.3.: Shifts of frequency pairs resulting from 2D cross correlation on optically thin regions.

ν_{low} [GHz]	ν_{high} [GHz]	RA [mas]	DEC [mas]
1.5	5.0	3.847	3.310
5.0	8.4	1.075	0.787
8.4	15	0.364	-0.014
15	22	0.352	0.336
22	43	0.046	0.129

Figures 4.6 and 4.7 (and B.1 to B.3) visualize the alignment procedure for each frequency pair. The upper two figures show the images in color-scale with the masks applied. In the lower left figure the contours of both maps are plotted before aligning and in the lower right

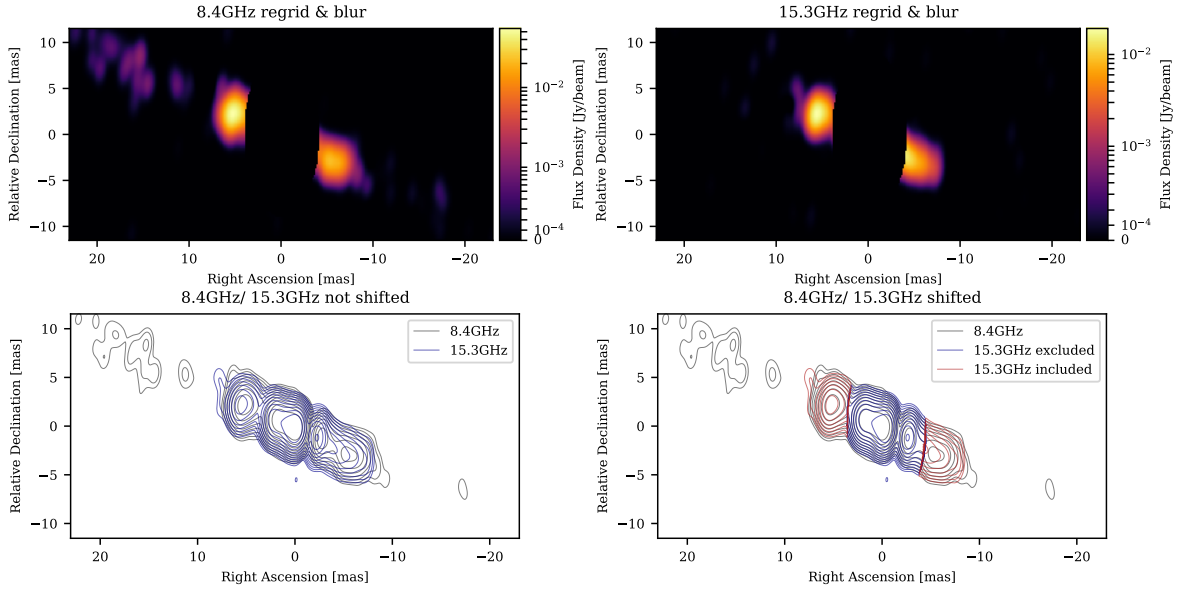


Figure 4.7.: (Top) images of the CLEAN model convolved with CLEAN beam with a mask applied for 8.4 GHz (left) and 15 GHz (right). An elliptical mask with position angle equal to that of the beam was applied to both images before cross-correlation. The mask was shifted slightly towards the western jet to exclude regions affected by free-free absorption. (Bottom) Contour maps without (left) and with applied shift (right). The red contours illustrate the region of the 15 GHz image used for the cross-correlation.

figure after aligning. The derived shifts were then applied to align all images and model-fit components with respect to the 43 GHz image (compare Fig. 4.8).

4.2.2. Component identification

After all images have been aligned, the model-fit components had been cross-identified over all frequencies and connected with a straight line in Fig. 4.8.

The labels have been chosen accordingly to previous multi-frequency observations of NGC 1052 (see e.g., [Kameno et al. 2001](#); [Kadler et al. 2004b](#); [Sawada-Satoh et al. 2008](#)). Components in the eastern jet are labelled with an ‘A’. The western jet component at 1.5 GHz is labelled ‘D’. At 5 GHz a new component gets visible, called ‘C’. The last western jet feature observable at 8.4 GHz and higher frequencies has the label ‘B’. The labels include a number which increases as going upstream of the jet, that is, by chronological order of appearance in a putative kinematic study. Parameter values of the individual components can be found in Tab. B.1.

Comparing the location of component D1 with the location of component D reported in [Sawada-Satoh et al. \(2008\)](#) and [Kadler et al. \(2004b\)](#) leads to an estimated speed of 0.08 pc yr^{-1} . This fits well with the velocities of outer components derived by [Vermeulen et al. \(2003\)](#) at 15 GHz.

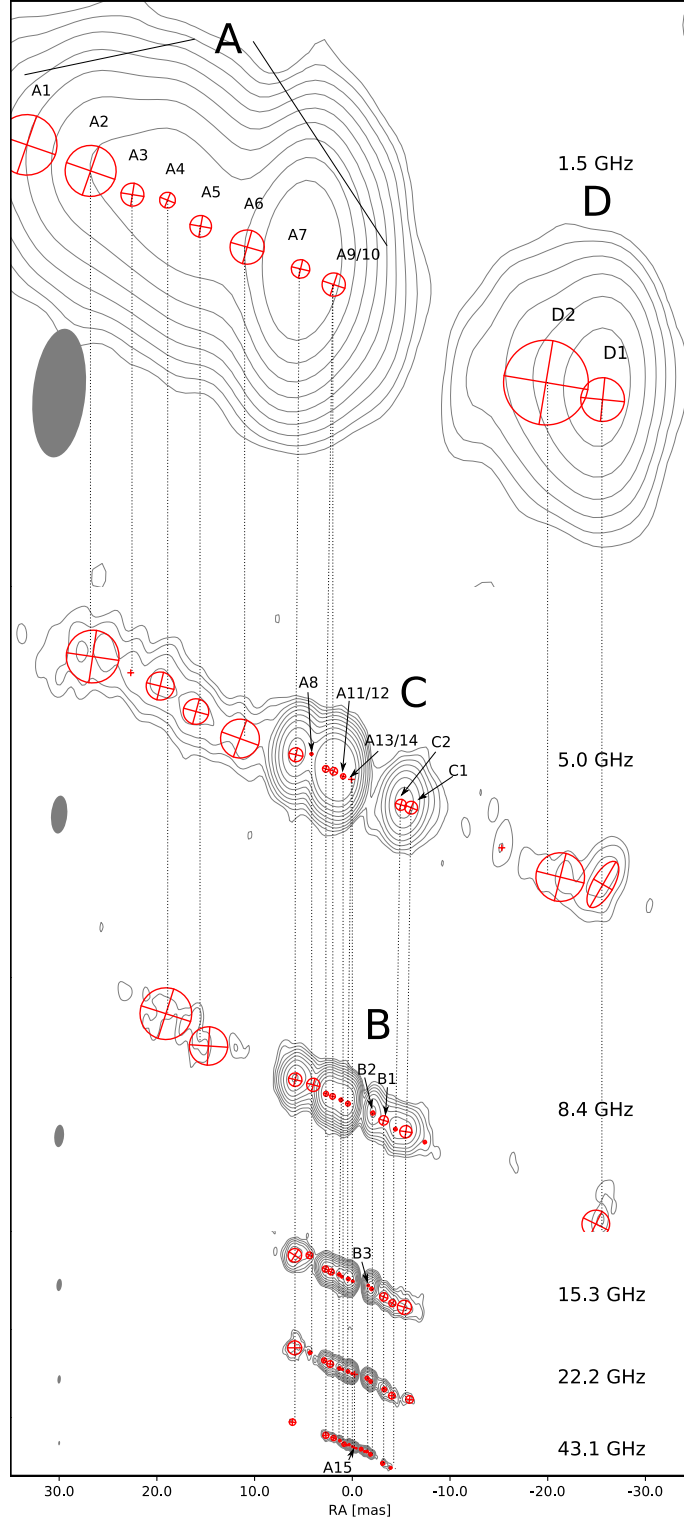


Figure 4.8.: Contour maps of images at all frequencies with Gaussian model components plotted on top, shifted with respect to the 43 GHz image based on the alignment described in Sect. 4.2.1, by a 2D-cross-correlation. Gaussian components which have been identified over frequency are connected by black lines and have names assigned as ‘A’ for the eastern jet, ‘B’, ‘C’ and ‘D’ for the western jet from inside to outside.

4.2.3. Spectral analysis

The continuum spectral behaviour of the source can be studied with multi-frequency images. In addition to a proper alignment, the individual images have to be convolved with the same beam and re-gridded to the same grid size. The maps were modified according to Sect. 4.2.1, regarding map-size, pixel-size, and convolved beam. Analogue to Sect. 3.2.2 the distribution of the spectral index α is plotted for adjacent frequency pairs of the clean images in Fig. 4.9.

The distribution of α is expected to be smooth with only a small transversal gradient and to decrease towards the outer regions of the jets. Hence, a visual inspection of the spectral index map is a possibility to check the performance of the alignment. For all five maps the distribution of α is very smooth and has close to no gradient in the transversal jet direction. Therefore, the alignment based on 2D-cross-correlation is a good choice and will be used for further analysis. Similar to the results presented in Sect. 3.2.2 the spectral-index maps reveal significant absorption in the region of the emission gap where the spectral indices reach up to $\alpha = 5$. The optically thin jet emission for all maps has an index of around -1 , consistent to previous observations (Kameno et al. 2001; Kadler et al. 2004b; Sawada-Satoh et al. 2008) and the values presented in Sect. 3.2.2.

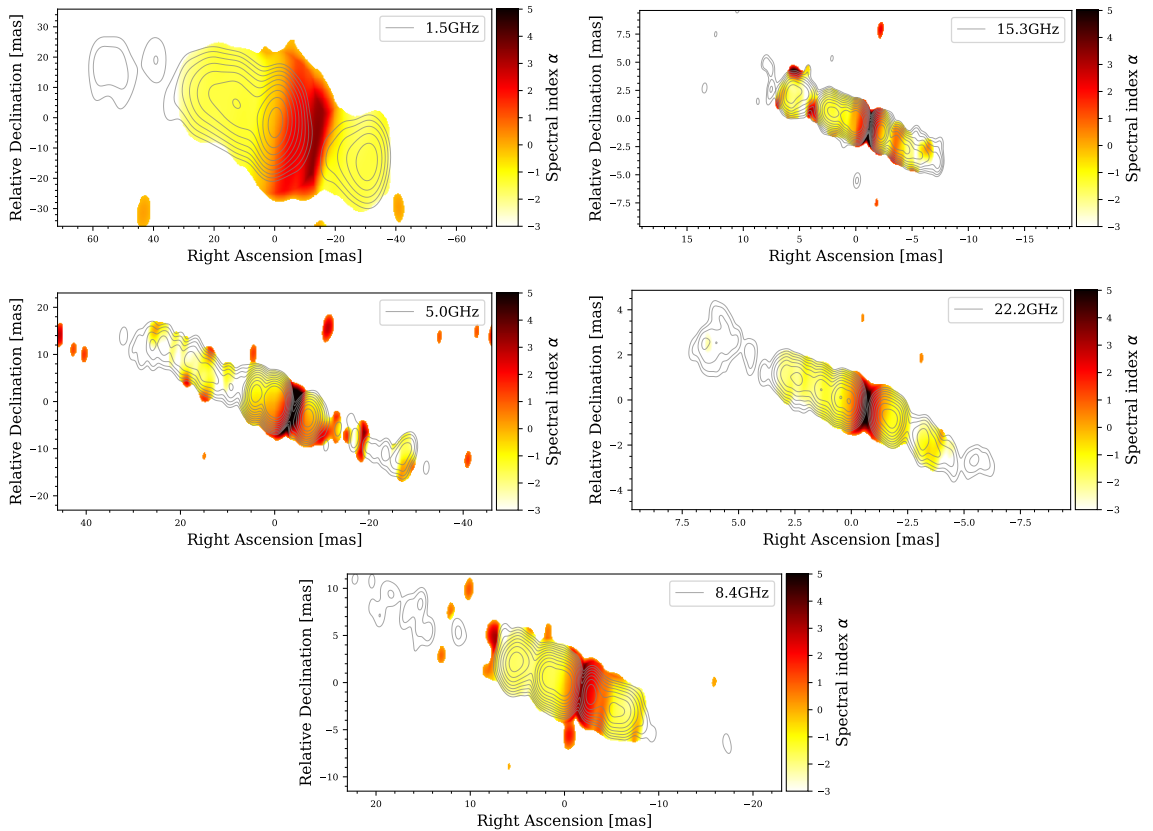


Figure 4.9.: Spectral index maps. (Left Top to bottom:) 1.5 GHz to 5.0 GHz, 5.0 GHz to 8.4 GHz, 8.4 GHz to 15 GHz;(Right Top to bottom: 15 GHz to 22 GHz, 22 GHz to 43 GHz. The contours in the maps correspond to the lower frequency of the pair.

Spectral behavior for individual regions

The model-fit components can be used to derive spectra of the whole source, eastern and western jet, and the components themselves. To obtain the total flux density for the individual regions the flux-densities of all model-fit components of the dedicated region had been summed up. The statistical uncertainties are derived from the individual uncertainty of the components flux-density and are only visible in Fig. 4.10 if the symbol size is exceeded. Components A are accounted for the eastern jet, components B, C and D are added up for the western jet. Also components in the dedicated regions which are only observed at one frequency were added to the total flux density of the individual region they are located in.

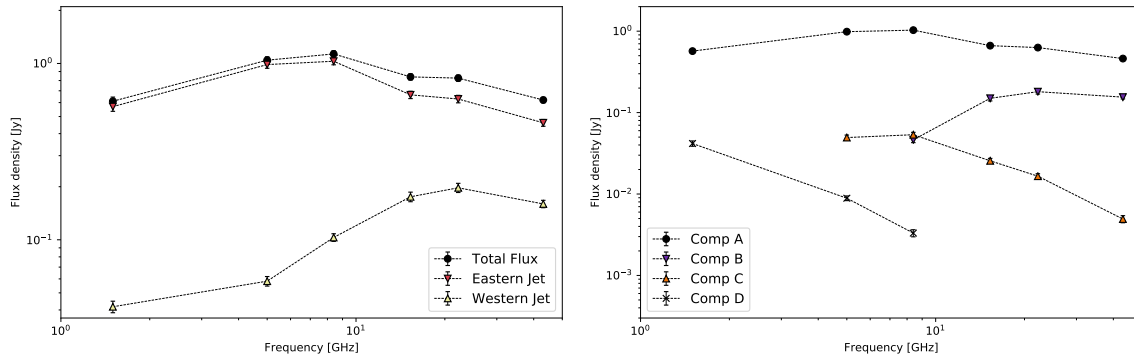


Figure 4.10.: Jet radio spectra (*Left:*) Flux density as a function of Frequency (Eastern jet, Western jet, and total). (*Right:*) Flux density for Regions A, B, C and D as a function of Frequency. Uncertainties were derived by error propagation assuming 10% amplitude uncertainty (see Sect.4.1), and are not plotted in case of being smaller than the marker size.

The individual spectrum over all frequencies for individual regions contains information about the emission and absorption properties for these regions. The source spectrum is relatively flat with a peak around 8 GHz (cf. Fig. 4.10 left). The evolution with frequency for the eastern jet traces the overall evolution. A different picture is drawn by the western jet. A large portion of the emission is absorbed at lower frequencies, resulting in a much higher peak frequency between 22 GHz and 43 GHz. In agreement with previous observations (Kadler et al. 2004b; Kamenno et al. 2001) the eastern jet is stronger than the western jet. Hence, the most likely explanation is that the eastern jet is approaching and the western jet receding.

Comparing the spectra of the four jet regions A, B, C, and D with Kadler et al. (2004b) the results look very similar, even though the observations differ by nearly 20 years. The inverted spectrum of component B can only be explained by external absorption and is therefore in agreement with previous studies of NGC 1052 (Sawada-Satoh et al. 2008; Vermeulen et al. 2003; Kadler et al. 2004b; Kamenno et al. 2001).

The jet-to-counterjet flux ratio is derived from the model fitted flux densities. Figure 4.11 shows the ratio as a function of frequency. Similar to the ratios reported in chapter 3 it is ~ 3 at 43 GHz for this observation. Being relatively stable until 15 GHz it shows a large increase at lower frequencies. At 5 GHz the jet is a factor of ~ 17 brighter than the counter-jet and decreases to a factor ~ 14 at 1.5 GHz. These values are similar to that which had been

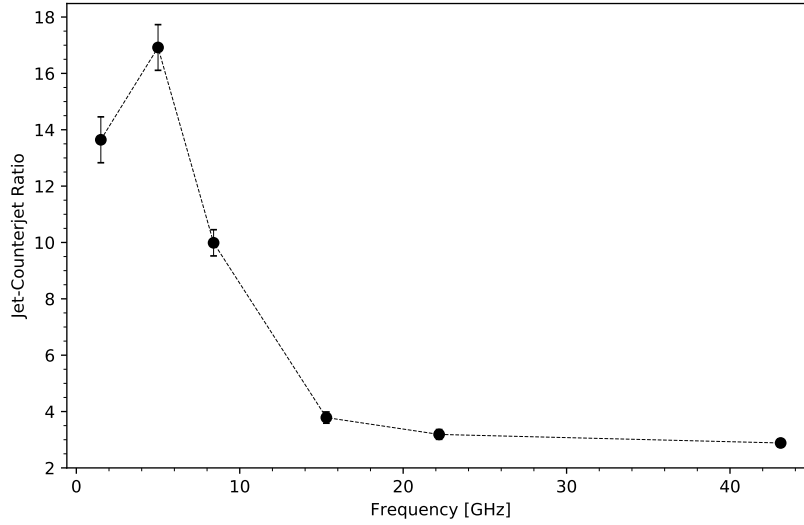


Figure 4.11.: Jet-to-counterjet ratio derived from the flux densities of the model-fit components as a function of frequency.

reported in [Kadler et al. \(2004b\)](#). From [Kameno et al. \(2001\)](#) the jet-to-counterjet ratio is known to be up to 50 at 2.3 GHz. An increase that large towards lower frequencies suggest the torus to have a large impact on the absorption of emission from the western jet.

4.2.4. Ridge-Line Analysis

The ridge-line connects the local flux density maxima along the jet. It has been derived based on the final clean maps for all six frequencies. First, the task SLICE in AIPS had been used to get slices perpendicularly to the jet axis. In the following one Gaussian was fitted to each slice, returning the peak value, the FWHM, peak location, as well as the uncertainties of the fit (for more information on the algorithm see [Vega-García et al. 2019](#); [Vega-García 2018](#)). The ridge-lines are plotted on top of the clean images in [Fig. 4.12](#). After applying the shifts derived in the previous section relative to the 43 GHz image to the ridge-line coordinates, the ridge-lines can be compared for all frequencies (see [Fig. B.4](#)).

There appear to be several structures deviating from a straight line. Particularly, there is a z-shaped structure for all ridge-lines at around -1 mas in RA. By comparing to the clean images in [Fig. 4.12](#) this structure coincides with the location of the emission gap at the respective frequency. Therefore we decided to convolve all images with a circular beam to avoid artefacts produced by an elliptical beam. The beam chosen is a circular beam with size $b = \sqrt{b_{\text{maj}} \times b_{\text{min}}}$, where b_{maj} and b_{min} are the original beam axes, in order to maintain the beam area. [Figure 4.13](#) shows the restored clean maps and the ridge-lines, which had been fitted to the restored images. In [Fig. 4.14](#) all ridge-lines are plotted on top of each other after shifting with respect to the 43 GHz image.

The z-shaped structure which was observed in earlier for the original, elliptical beam, is not visible any more. In addition the ridge-line is much more straight in comparison to [Fig. B.4](#)

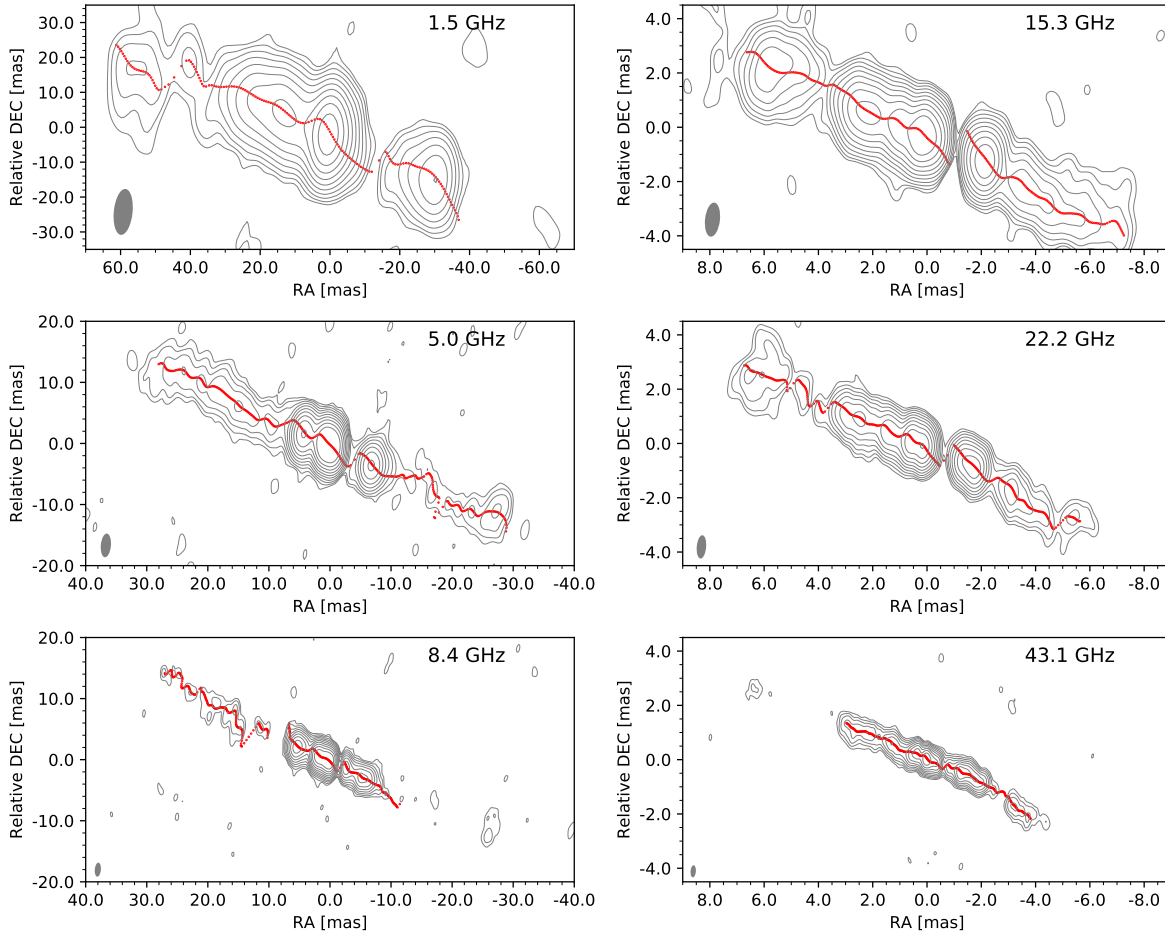


Figure 4.12.: Final clean image of NGC 1052 at all six frequencies with ridge-lines plotted on top (red dots). The contours start at 5, 4, 4, 3, 4, 3 times the noise level for L, C, X, U, K, and Q band, respectively and increase logarithmically by factors of 2. Beams are shown at the bottom left. Images parameters are presented in Tab. 4.1.

and do not show strong curvature. However, there is a slight change of orientation in the counterjet side from about -2 mas to about -5 mas. This may point towards a southward bending of the counterjet, which could also explain the higher jet-to-counterjet ratio at 43 GHz in comparison to the one reported in chapter 3.

Figure 4.15 shows the jet diameter and intensity along the ridge-line which had been derived from the ridge-line fits to slices along the jet for the individual images. The diameter corresponds to the FWHM of the fitted Gaussian. As in Fig. 4.14 the intensity and diameter profile had been shifted with respect to 43 GHz, setting the origin to the map peak at 43 GHz. Only measurements of jet width and intensity were included into the analysis for which the fitted uncertainty on the width did not exceed the width itself.

The diameter of the jets gets smaller towards higher frequencies what can be explained by the improving resolution. If compared to the FWHM of the restored beam (dotted lines in Fig. 4.15) the jets are not resolved at any frequency as the width is in all cases smaller than

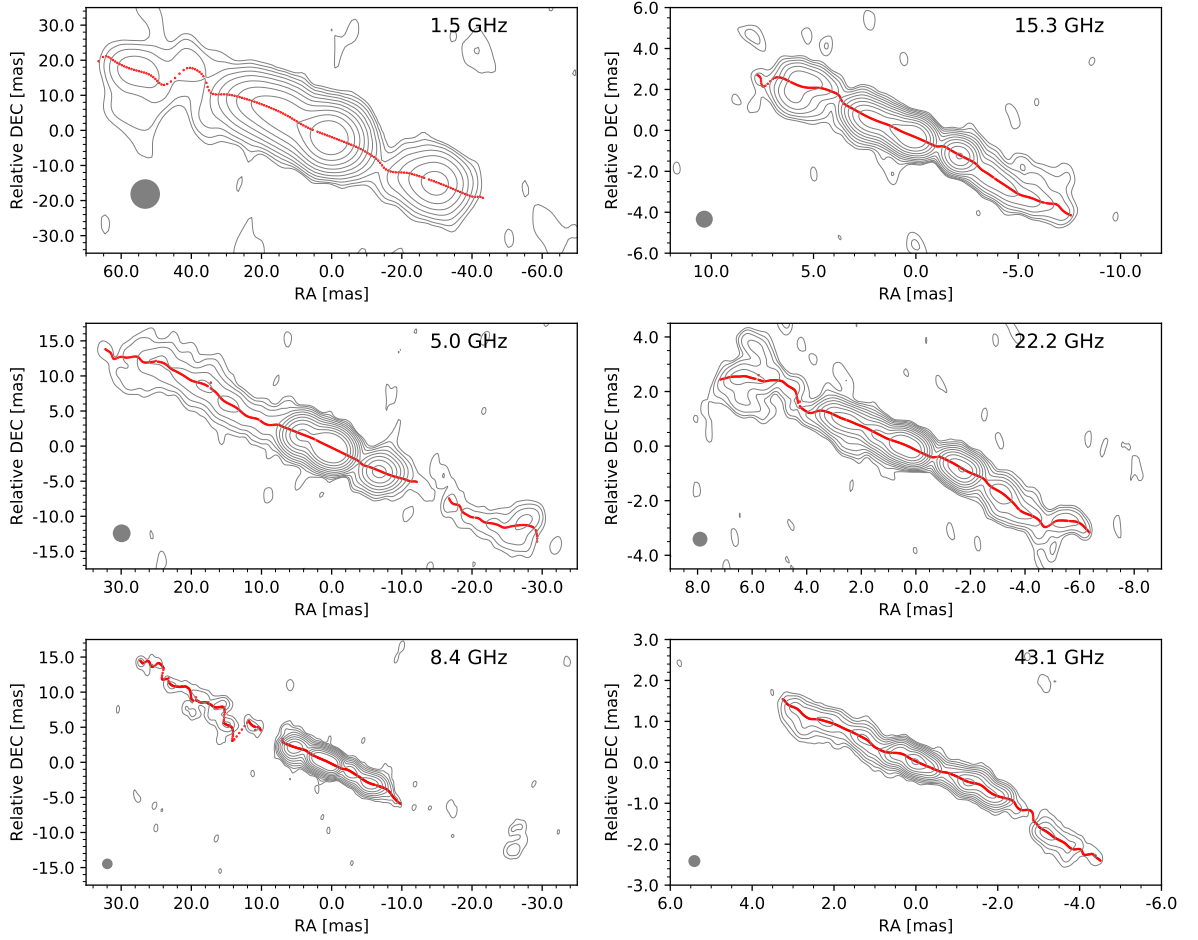


Figure 4.13.: Final clean image at all six frequencies restored with a circular beam with ridge-lines plotted on top (red dots). The contours start at 4, 4, 4, 3, 2, and 3 times the noise level for L, C, X, U, K, and Q band, respectively and increase logarithmically by factors of 2.

the beam in that direction.

The bottom panel in Figure 4.15 shows several structures in the flux-density profile, i.e., local maxima, that fit in location over several frequencies. The main peak at each frequency corresponds to the eastern jet core and is therefore shifted inwards with increasing frequency. The peak at ~ 7 mas corresponds to component A7, its position is stable over all frequencies. The same is true for components A9 located at ~ 3 mas at frequencies ≤ 8.4 GHz in the eastern jet, components B2 at ~ -2 mas from 8 GHz to 22 GHz, and C(2+1) at ~ -5 mas at 5, 8.4 and 22 GHz in the western jet. In addition, the flux density profile in the outermost regions D and A1 to A5 fit well at lower frequencies where the emission is not too faint to detect. This suggests that these regions are not suffering from external absorption. Most likely the increasing faintness of the outer jet regions with increasing frequency results from the spectrum of the synchrotron emission and the decreasing sensitivity towards outer jet regions.

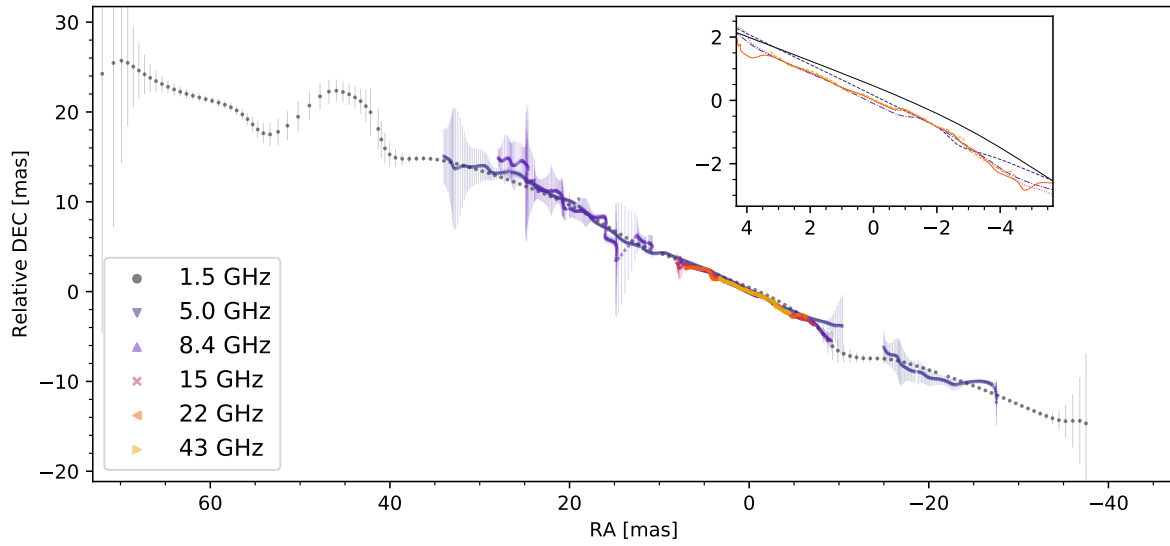


Figure 4.14.: Ridge-lines at all frequency bands. Images were aligned accordingly to the methods presented in Sect. 4.2.1. The inset panel shows a zoom into the inner region of the main plot. Error bars are derived from the Gaussian fit to slices along the jet structure.

4.3. Results of RadioAstron observation of NGC 1052

As discussed in Sect. 4.1.2 there were no fringes detected to the space antenna Spekt-R of the RadioAstron mission, hence the following analysis is based on the ground-array image consisting of twenty-nine antennas.

Even without RadioAstron the 22 GHz image of the ground array gives more insights into the source morphology due to its enhanced North-South resolution. Compared to the VLBA K-band image half a year later (compare Fig. 4.13) the structure along the jets looks very similar. The widths of the jets as seen in the clean image (Fig. 4.5 and 4.16) shrinks accordingly to the improved resolution and it is very likely still not resolved. The change of direction in the western jet is more pronounced than in the VLBA image.

4.3.1. Ridge-Line Analysis

As was done for the VLBA multi-frequency observation I fitted a ridge-line to the RadioAstron ground-array image. Figure 4.16 shows the ridge-line plotted on top of the clean contour map. It is very similar to the result from the VLBA observation when restoring with a circular beam. The stream line is very straight and does not show any significant wiggles except the smooth directional change in the western jet. This proves the previous assumption that an elliptical beam may introduce artefacts.

The RadioAstron image reveals a very similar morphology compared to the 22 GHz VLBA image in Fig. 4.13. The ridge-line was derived for the final natural weighted image in the same manner as described in Sect. 4.2.4 and is plotted on top of the final clean image in Fig. 4.16. It is extraordinarily straight except for the change of jet direction in the western jet at ~ 2 mas.

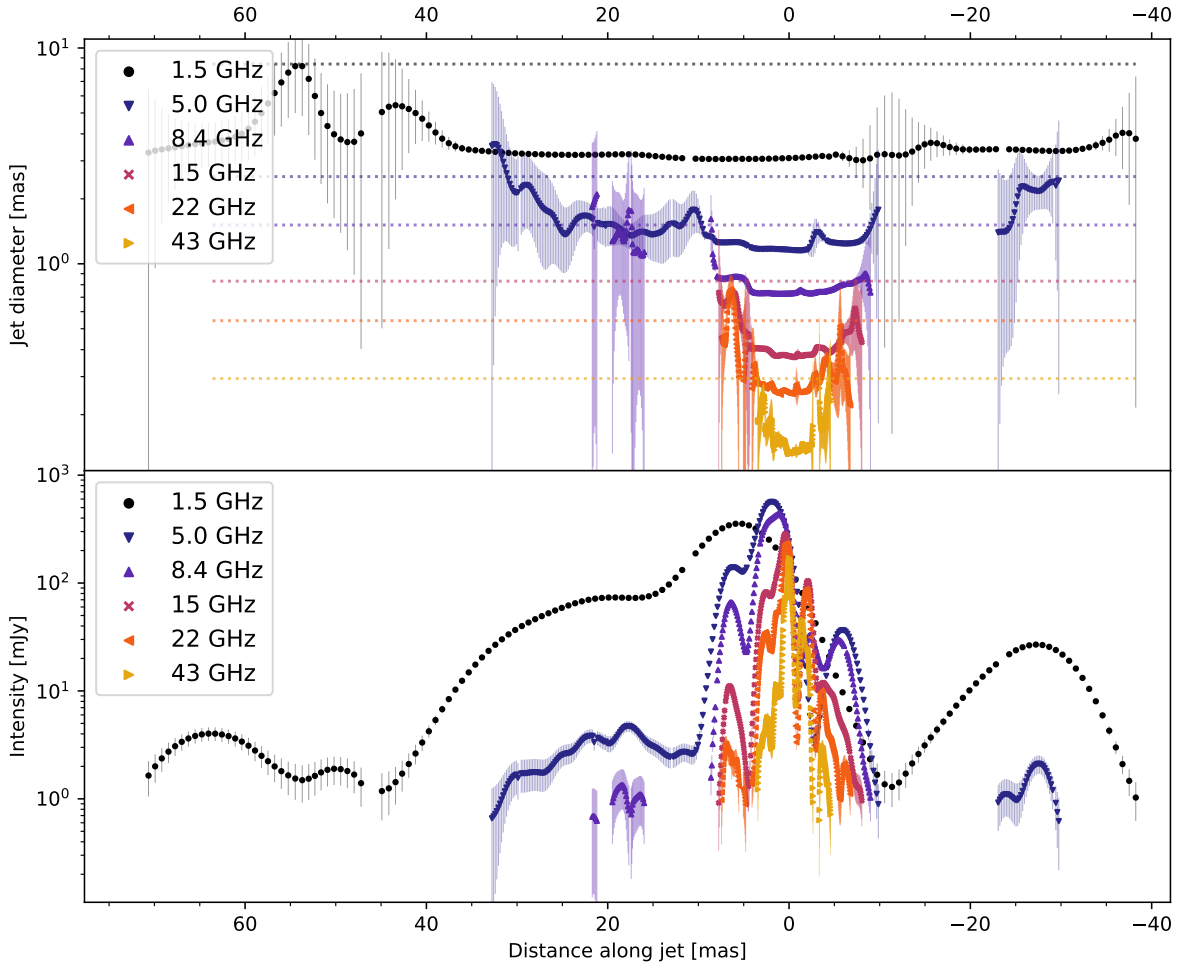


Figure 4.15.: (*Top*) Jet diameter and (*Bottom*) intensity along all jet ridge-lines (see Fig. 4.13 and 4.14). Dotted lines denote the beam FWHM perpendicular to the mean jet axis. Error bars are derived from the Gaussian fit to slices along the jet structure for the individual images.

The jet width along the ridge-line is smaller than the FWHM of the beam perpendicular to the jet axis over the whole jet (compare Fig. 4.18) and therefore still unresolved. The flux density along both jets is similar to the results reported in Sect. 4.2.4.

4.4. Discussion

In this section I compare the results from the multi-frequency VLBA observations and the 22 GHz RadioAstron ground array observation and discuss their implications.

Figure 4.17 shows the ridge-lines corresponding to VLBA 15, 22, and 43 GHz and the RadioAstron ground-array image at 22 GHz plotted on top of each other, to study the innermost region of the source in more detail. The VLBA ridge-lines are shifted according to Sect. 4.2.1, setting the 43 GHz core at the map origin and assuming the same shift for both 22 GHz im-

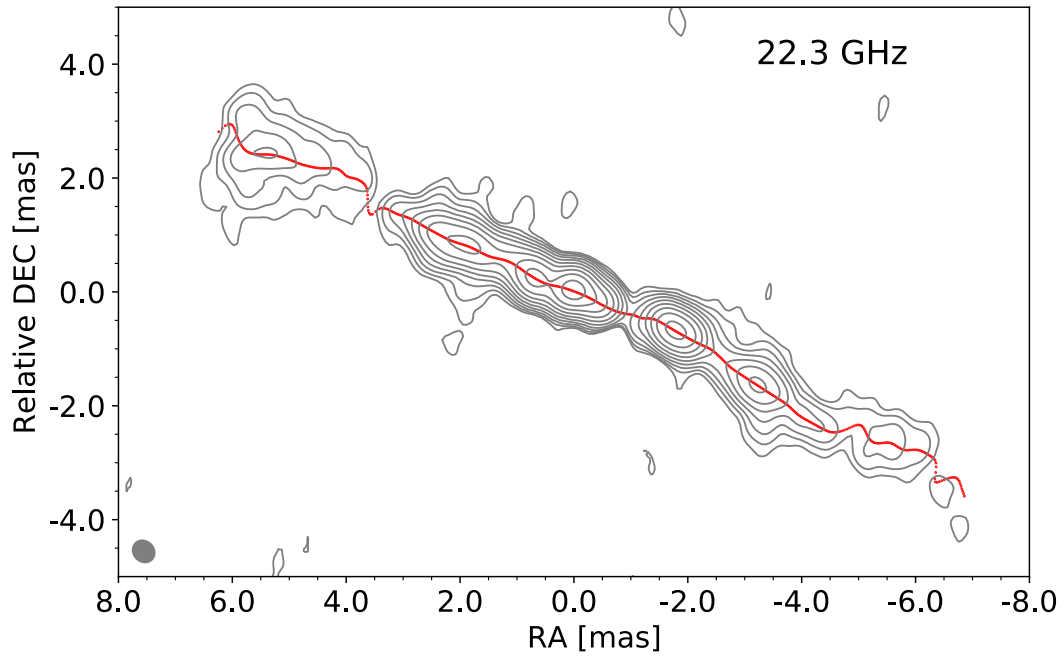


Figure 4.16.: Clean image of RadioAstron ground array observation of NGC 1052 at 22 GHz with ridge-line plotted on top. The contours start at 4 times the noise level and increase logarithmically by factors of 2. See Tab, 4.2 for the image parameters.

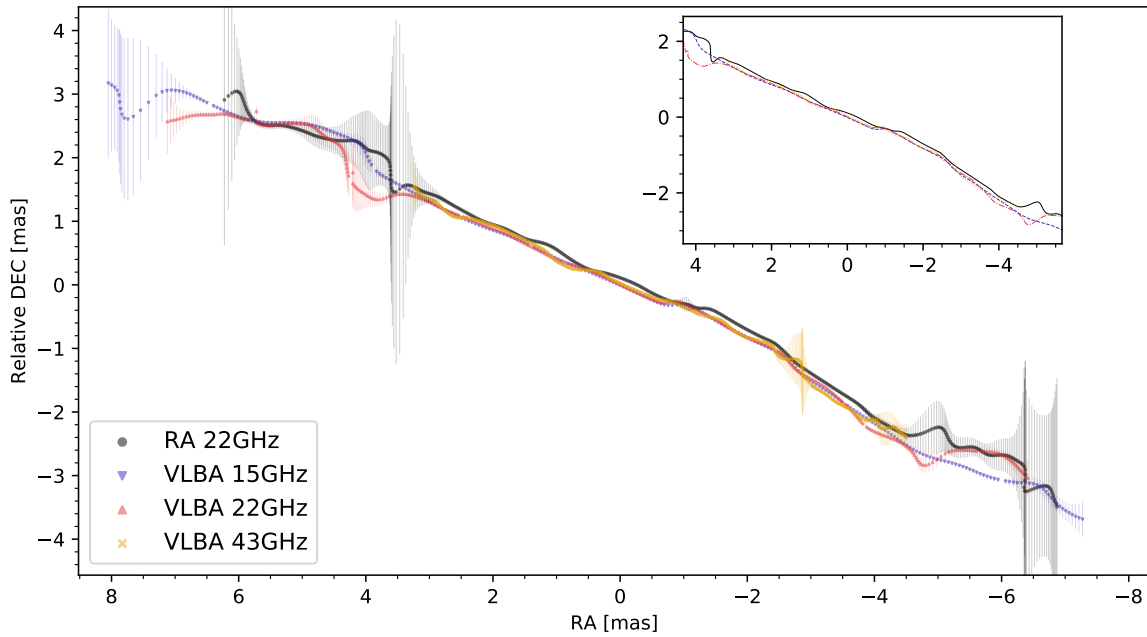


Figure 4.17.: Jet ridge-lines compared for RadioAstron and VLBA U, K, and Q observations. Error bars are derived from the Gaussian fit to slices along the jet structure for the images.

ages. For the RadioAstron ground array observation the same shift was assumed as resulted from the VLBA 22 to 43 GHz alignment.

The observations with the VLBA and RadioAstron are about half a year apart. The source is variable over this time range. Hence, differences between the VLBA and RadioAstron observations are expected. Comparing the flux evolution along the jet for both 22 GHz images in Fig. 4.18 the eastern jet feature at around 2 mas is in case of the VLBA observation (red triangles) about 0.5 mas downstream of the same feature from the RadioAstron ground array measurement (black dots). The same behavior can be observed when comparing to the flux density along the jets of the RadioAstron ground array image to that at 43 GHz, which has a resolution closer to the RadioAstron ground array image. This travel distance is consistent with the expected speeds of jet features in NGC 1052 (see Sect. 3.2.4 and [Lister et al. \(2019\)](#)).

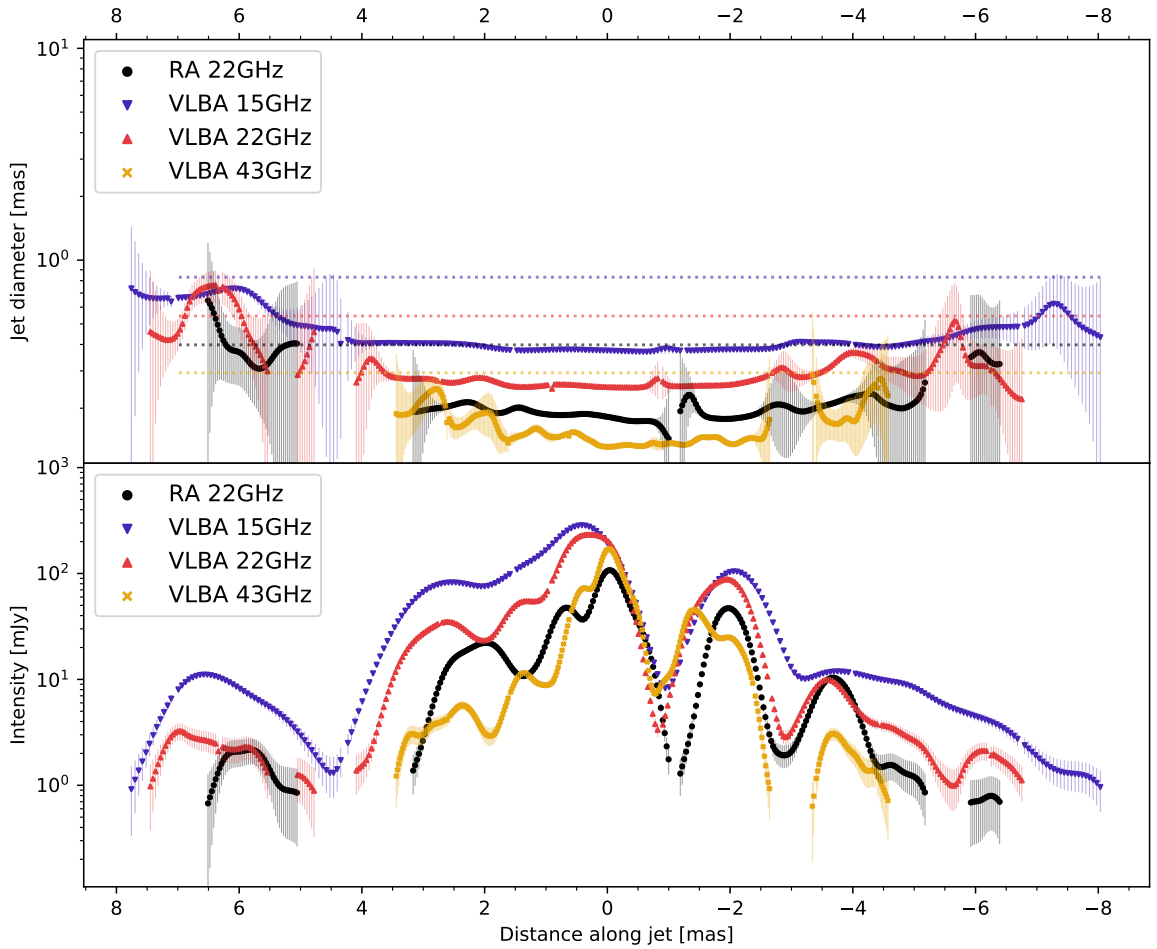


Figure 4.18.: (*Top*) Jet diameter and (*Bottom*) intensity along jet ridge-line for RadioAstron and VLBA U, K, and Q observations. Error bars are derived from the Gaussian fit to slices along the jet structure.

The flux density profile of the 43 GHz VLBA observation in Fig. 4.18 has similarities to the stacked 43 GHz image presented in Sect. 3.2.1 (Fig. 3.4). The central peak is not as

pronounced as can be seen in the flux profile of the stacked image as well as the profile for individual epochs between 2005 and 2009 (compare Fig.A.1). There are two bumps at about -1 mas and -2 mas in the case of the new 43 GHz observation coinciding with the plateau in the stacked image, which may be explained by recollimation shocks resulting from an over-pressured jet (Fromm et al. 2019).

4.4.1. Expansion of the jets in NGC 1052

As recently claimed by Nakahara et al. (2019) the jets in NGC 1052 evolve symmetrically based on VLBI observations between 1989 and 2001. The jet width profile, studied from 300 to $4 \times 10^7 R_S$ (corresponding to 0.045 to 1.4×10^3 mas), was found to show a cylindrical structure which has a transition to a conical outflow at $\sim 10^4 R_S$ (or 1.5 mas), which is consistent with the size of the surrounding torus having a radius of ~ 5 mas (Kamenno et al. 2001). Hence, Nakahara et al. (2019) suggest that the over-collimation leading to a cylindrical shape of the inner jets may be caused by the external pressure by the obscuring material. A more likely explanation is given by (Kovalev et al. 2019). The authors did an extensive search for breaks in the widths profile of AGN jets based mainly on the MOJAVE sample (Lister et al. 2019), including NGC 1052. They find a break in the power law fitted to the jet width of the eastern jet in NGC 1052 at 2.5 mas with power-law indices of $k_1 = 0.391 \pm 0.048$ and $k_2 = 1.052 \pm 0.081$ before and after the break, respectively. The break point for the whole sample is at $r_{\text{break}} \in (10^5, 10^6) r_g$ and therefore, in the area of the Bondi radius ($r_B = 2GM_{\text{BH}}/c_s^2$, with the sound speed of the gas c_s). The break is suggested to take place at the transition location from the magnetically dominated to the particle dominated region.

The jets are not resolved within the herein presented multi-frequency observations. Therefore, it is not possible to verify this result. Even the RadioAstron ground array 22 GHz image could not resolve the jets, for which the beam size perpendicular to the ridge-line is smaller than the beam size for the 22 GHz image reported in Nakahara et al. (2019) and of the same order as the beam size for the 43 GHz image of the same publication. The inner jet of NGC 1052 may be collimated to a width too small to be detectable by present observations and hence appears cylindrically shaped resulting from the resolution limit.

Images with a higher North-South resolution are needed to study the width of the source in greater detail and to be finally able to resolve the twin-jets. One possibility is to go to even longer baselines, which would require space-VLBI. Given that there is currently no operating Radio telescope in space, this road cannot be followed in the near future. Another approach is by combining an improved North-South with high frequency observations at mm-wavelengths. The current progress on enhancing GMVA, ALMA, and EHT is very promising to achieve this goal. Once the ALMA phasing project-phase is finished, the improved flux-density limit will allow to detect fainter sources. A similar enhancement is expected by the enlargement of bandwidth of the GMVA and the bit rate of EHT.

4.4.2. Jet bending and precession or interaction with the ambient medium

Figure 4.17 zooms into the inner 15 mas of NGC 1052. By including only the higher resolution images ≥ 15 GHz of the campaign the innermost streamline is well reproduced by all ridge-lines. All four ridge-lines follow nearly the same path, tracing the changing direction of the western jet at ~ -2 mas, to turn back to the original one at ~ -5 mas. This is the first time this morphology has been observed in NGC 1052. It introduces an asymmetry to the twin-jets, fitting into the picture drawn in chapter 3. This may be caused by the interaction with the ambient medium and/or it is intrinsic to the jet production.

One explanation is the interaction of the jet with the surrounding medium. The directional change is located at a similar distance as the transition location of ~ 1.5 mas towards a conical outflow as suggested by Nakahara et al. (2019). Based on observations at 2.3, 8.4, and 15 GHz, the radius of the free-free absorbing torus was estimated to ~ 5 mas (Kamenov et al. 2001), whereas a spectral analysis from the multi-epoch observations presented in chapter 3 suggests strong absorption effects at 22 GHz up to a distance of ~ 1 mas to the 43 GHz core. The location also fits well with the break of the jet width found by Kovalev et al. (2019).

Another possibility is a bending or helical motion of the jet. If the observed morphology is caused by a helical motion of the jet, the changes of the flux density reported in Chap. 3 may be explained by relativistic boosting and de-boosting of different parts of the outflows. As discussed in Sect. 3.3.3, a precession of the jets cannot be ruled out. However, the directional change only appears about 2 mas downstream to the center and there is no information on the source structure during the period 2014 – 2017, which would allow one to trace the evolution of the jet from ejection of the components observed at a core distance of 2 mas until April 2017. Therefore, the jet stream line cannot be connected directly to a directional change of material emitted at the jet nozzle. To prove whether the change of the jet stream is caused by a precession of the jet nozzle further analysis is needed, especially high-resolution observations over a larger period of time are essential. In addition, there is no hint for a similar change in the eastern jet, and the overall ridge-line is very straight. This makes a precession very unlikely.

Further analysis and more high-resolution multi-frequency and multi-epoch observations are essential to address the impact of the ambient medium as well as the jet formation processes which is beyond the scope of this thesis.

4.5. Summary & Conclusions

In this chapter I presented my results based on VLBA and RadioAstron observations at frequencies between 1.5 GHz and 43 GHz in April 2017 and November 2016, respectively.

- VLBA images were produced following standard calibration in AIPS and hybrid imaging in DIFMAP. The images at all six frequencies were aligned based on a 2D cross-correlation, excluding the innermost region between both jets, which suffer from free-free absorption.

- For the RadioAstron observation there were no fringes detected to the orbiting antenna. However, the ground-only-array including antennas from the EVN, the VLBA with the VLA and the Australian LBA, yields the highest North-South resolution of NGC 1052 at 22 GHz until now. Due to different frequency setups and inconsistency of visibility amplitude over different IFs, the calibration was tedious and needed intensive and careful bookkeeping.
- The final CLEAN images draw a similar picture as observed before: spanning up to a distance of 60 mas with an emission gap between both jets which decreases with increasing frequency
- The derived ridge-lines show very straight jets, with a directional change at -2 mas in the western jet that turns back to the original orientation at ~ -5 mas. There is no comparable structure in the eastern jet.
- The width of the jets was obtained from Gaussian fits to slices perpendicular to the jet stream line. Comparing with the width of the beam, the jets are transversally not resolved. Even with the higher resolution image obtained by the RadioAstron ground-array the jets could not be resolved transversally.
- As the jets are unresolved for these observations no further constrains on the collimation of the jet can be made. In contrast to other AGN sources, as Cyg A, 3C 84, or M 87, the jets in NGC 1052 are much narrower.
- Taking all properties of the jets in NGC 1052 as derived from these observations into account, the most likely explanation for the bending only of the western jet are asymmetries either caused in the ambient medium or in the jets themselves.

5 | GMVA observation of NGC 1052 in 2017

With the aim of probing the structure of NGC 1052 at higher resolution and beyond the torus absorption, the next step is addressing the source at shorter wavelengths. This task is possible with the Global mm VLBI Array (GMVA) at 3.5 mm and the Event Horizon Telescope (EHT) at 1.4 mm.

5.1. Data reduction, results and discussion

NGC 1052 had been observed with the global millimeter VLBI array (GMVA) at 86 GHz on March 31, 2017. The observation was correlated at the DiFX software correlator in Bonn. Data reduction was performed as described in Sect. 3.1 with a few alterations. Observations at high frequencies as 86 GHz are very sensitive to bad weather. This sets a big problem, especially for relatively faint sources as NGC 1052. The fringe fitting calibrator sources 3C 84 and 0224+069 were used for manual phase calibration. The radiometry file (AIPS task ANTAB), which contains all system temperature T_{sys} measurements, had only sparse sampling for Pico Veleta as well as very spread values. Hence I replaced the entries with a mean value for left and right polarization each.

During fringe fitting the data turned out to be very noisy, both for the calibrator sources and the target source. As a consequence, it was difficult to obtain trustworthy solutions for delay and delay rate. As described in Sect. 4.1.2, I applied my collection of scripts for calibration using PARSELTONGUE and AIPS to the GMVA dataset (see Appendix C for more information on the quasi-pipeline). I tested different approaches of calibration, a subset of which includes:

- Amplitude calibration before or after global fringe fitting.
- Using the re-referencing algorithm implemented in the FRING task or in the SNSMO task. When turning off re-referencing in FRING, SNSMO was used to first smooth the solutions resulting from fringing and applying a re-referencing afterwards.
- Different settings of SNSMO, as interpolating the smoothed solutions for flagged entries in the SN table, or leaving flagged entries flagged. Smoothing and interpolating only within the same source or over different sources.

Some approaches resulted in a larger number of visibilities recovered for NGC 1052 after finalizing the calibration. But big parts of the data following from these approaches were spurious and hence had to be flagged later during the imaging phase. In addition, the total flux density of the final image tended to be larger as what is expected from the continuum spectrum, and the final clean image only contained one single, unresolved component without any hints of jets.

Therefore, I am presenting here results from two approaches. One, using SNSMO to interpolate FRING delay and delay rate solutions to flagged solutions and one without interpolation. During fringe fitting, the coherence time of this observation turned out to be quite short, resulting in a solution interval in FRING of 0.15 s. The final uv -coverage from the calibration run not using SNSMO is shown in Fig. 5.2.

After a-priori amplitude and phase calibration in AIPS, standard imaging in DIFMAP was applied to both calibration strategies. Due to the very sparse sampling of the final calibrated VLBI data of NGC 1052, I deviated slightly from the standard procedure. To not loose any more data I turned off *selfflagging* in DIFMAP and flagged any spurious data by hand. A stable model required to add a little bit of emission towards the East and the West of the central component (compare final CLEAN image in Fig. 5.1). These CLEAN components deviate from the typical direction of the jets. It is not clear whether these features are due to problems in the calibration, effects of the sparse uv -coverage or real structure. However, the structure is recovered for both calibration approaches. The parameters of the final CLEAN images are listed in Tab. 5.1. Hence, the source had been detected, even so it was not possible to recover any jet structure.

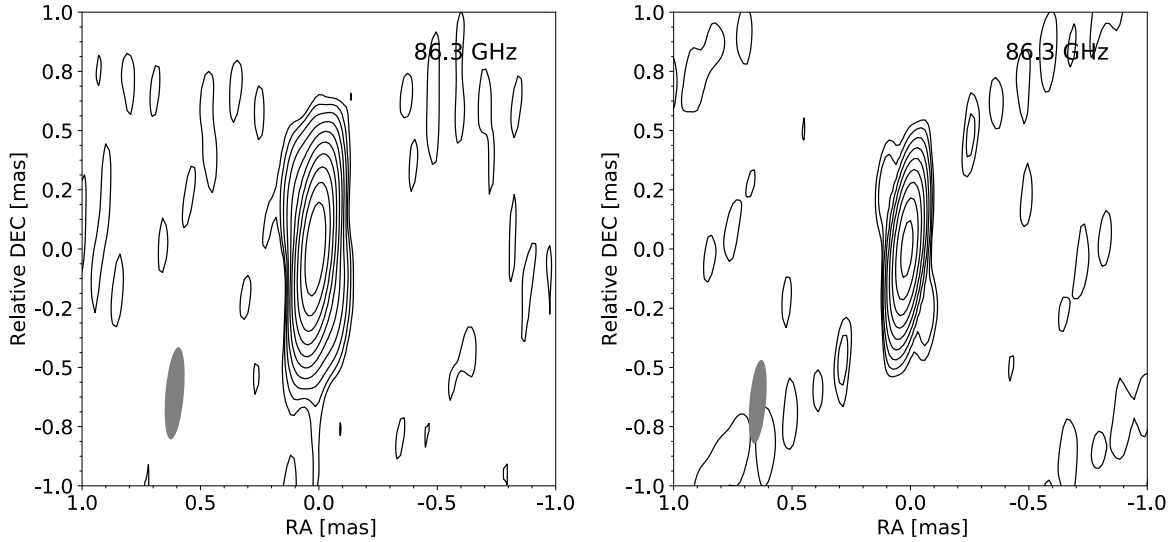


Figure 5.1.: Naturally weighted CLEAN image of NGC1052 at 86 GHz, observed with the GMVA on March 31, 2017. During calibration FRING solutions were not smoothed by task SNSMO (left) or smoothed (right). The contours start at one and four times the noise level, respectively and increase logarithmically by factors of 2 for left and right image, respectively. The dynamic range of the images is 1420:1 and 797:1, for left and right image, respectively. The CLEAN beam is plotted in the lower left corner. The parameters of the final CLEAN images are listed in Tab. 5.1.

Figure 5.3 shows the visibility function as a function of the baseline length $q = \sqrt{u^2 + v^2}$ in the Fourier plane projected along a position angle of 64° after the imaging process with the model plotted on top. The visibility amplitude shows a flat distribution with projected uv -distance, suggesting an unresolved source structure. There is no big difference between the

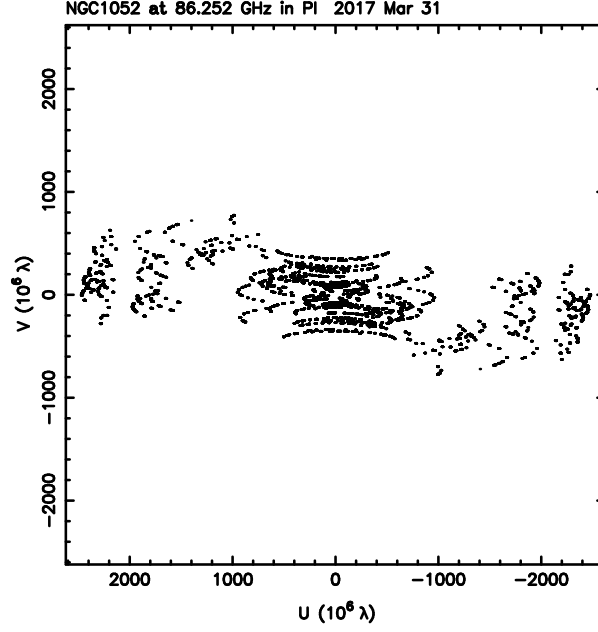


Figure 5.2.: uv -coverage from the the 86 GHz GMVA observation from March 31, 2017, resulting from the calibration run without using SNSMO.

two calibration runs, except a larger number of visibilities when interpolating FRING solutions to flagged values.

The GMVA observation is accompanied by a 43 GHz observation, observed with the eight participating VLBA antennas while the European stations did pointing and calibration scans on nearby calibrator sources. Standard calibration and hybrid imaging was applied as described in Sect. 4.1. The final CLEAN map (compare Fig. 5.4) shows a similar morphology to the VLBA observations a few days later as discussed in chapter 4. Due to the smaller number of scans, the resolution is not as good. The parameters of the final CLEAN images are listed in Tab. 5.1.

Table 5.1.: Image parameters for GMVA observations from March 31, 2017 at 86 GHz with natural weighting and simultaneous 43 GHz observation observed with the eight participating VLBA antennas (PT, OV,NL, MK, LA, KP, FD, BR).

Smoothing	Frequency [GHz]	RMS ¹ [$\frac{\text{mJy}}{\text{beam}}$]	S_{peak} ² [$\frac{\text{Jy}}{\text{beam}}$]	S_{tot} ³ [Jy]	b_{maj} ⁴ [mas]	b_{min} ⁵ [mas]	PA ⁶ [°]	DR ⁷
Yes	86	0.61	0.85	0.90	0.355	0.069	−5	797:1
No	86	0.99	1.0	1.11	0.391	0.078	−5	1424:1
No	43	0.20	0.31	0.82	0.76	0.27	−21	1256:1

¹ Root-mean-square noise level of image ² Peak flux density ³ Total recovered flux density

^{4,5,6} Major, minor axes and major axis position angle of the restoring beam ⁷ Dynamic range: Ratio between the map peak and the rms inside a CLEAN window far away from the source structure

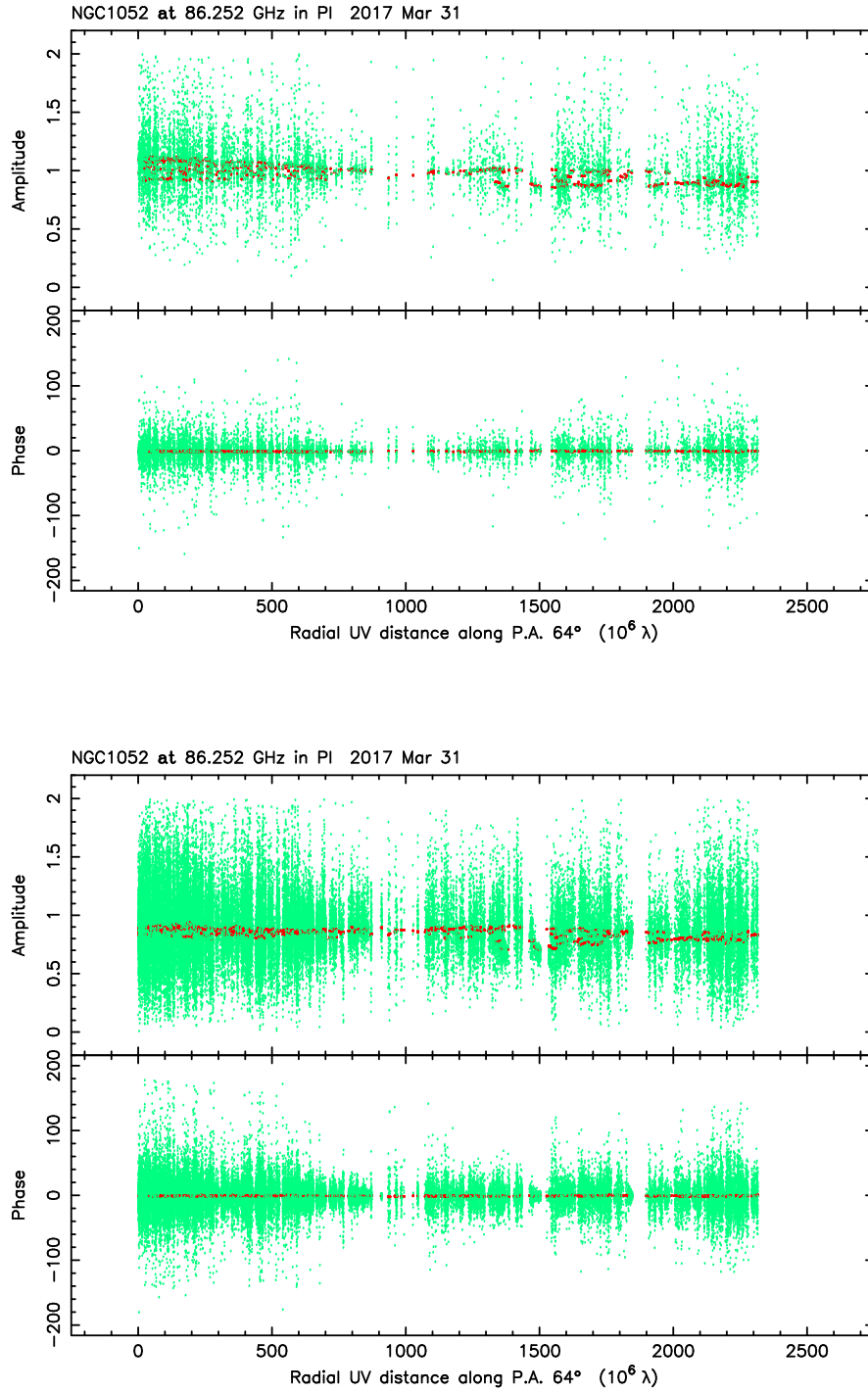


Figure 5.3.: Visibility function as a function of the baseline length $q = \sqrt{u^2 + v^2}$ in the Fourier plane projected along a position angle of 64° (green dots) after CLEAN and self-calibration with final model in red for calibration not applying SNSMO (top) and applying SNSMO (bottom).

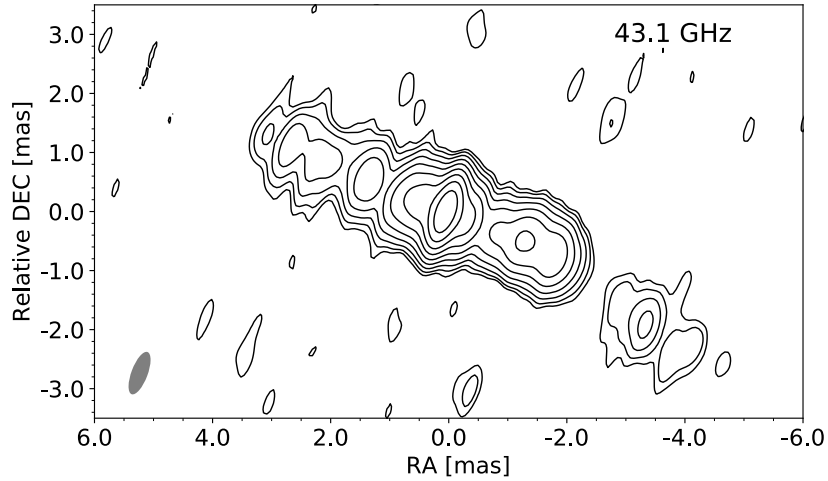


Figure 5.4.: Naturally weighted CLEAN image of NGC1052 at 43 GHz, observed with eight VLBA antennas (PT, OV,NL, MK, LA, KP, FD, BR) on March 31, 2017. The contours start at three times the noise level and increase logarithmically by factors of 2 . The dynamic range of the images is 1256:1. Image parameters are listed in Tab. 5.1.

This observation and the VLBA multi-frequency observation deviate by only 4 days. Hence, there are no large changes in terms of morphology or flux density expected for the 43 GHz images, still the map parameters differ. The total 43 GHz image flux on March 31, 2017 is 0.82 Jy, while 0.59 Jy one week later on April 4. As the dynamic range is above twice as high in case of the observation on April 4, the 43 GHz flux density presented in this chapter is corrected to match the value from April 4th. Assuming the same offset for the 86 GHz observation, the total flux densities obtained from both calibration approaches is corrected as well.

After this correction both 86 GHz and the 43 GHz flux density can be added to the continuum spectrum obtained in Sect. 4.2.3 (compare Fig. 5.1). An uncertainty of 10% was assumed for the amplitude. Even corrected, both 86 GHz flux density measurements are too high, if compared with broad band spectra (see for example [Fromm et al. 2019](#), and references therein).

CLEAN maps resulting from different calibration and imaging approaches reveal some spread of the total flux density. From all calibration approaches only a single component could be recovered.

There are mainly two explanations for the difficulties of the analysis of this data set: 1) The timing of the observation was unlucky as NGC 1052 was in a low state between two brightness peaks as can be seen in the 15 GHz OVRO lightcurve¹ ([Richards et al. 2011](#)). 2) The weather condition during the whole GMVA session were not optimal. Single dish flux measurements at Effelsberg give an estimate on the flux density of 1.5 ± 0.7 Jy (U. Bach, priv. comm.) and calibrations on planets around the observing time suggest an amplitude uncertainty of 30% (U. Bach, priv. comm.).

¹Lightcurve can be found at [OVRO lightcurve of NGC 1052](#)

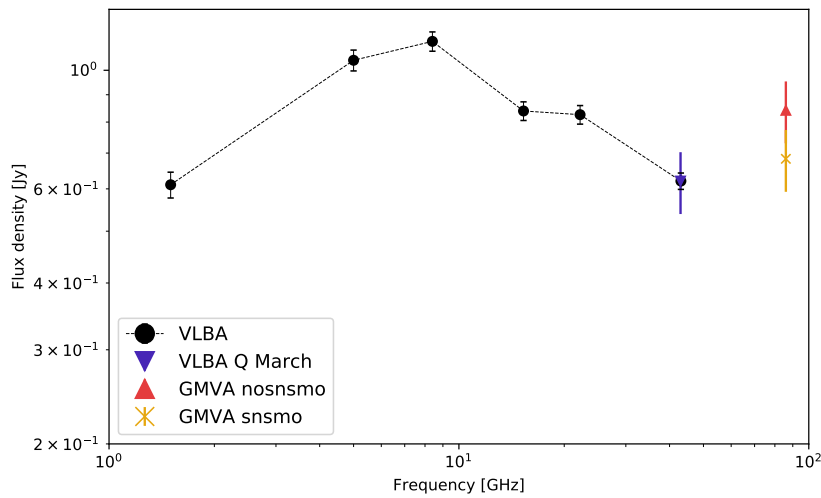


Figure 5.5.: Continuum spectrum of VLBA observations from 1.5 GHz to 43 GHz on April 4, 2017 and observations at 86 GHz obtained with the GMVA and at 43 GHz observed with the VLBA on March 31, 2017.

Smaller flux densities are expected for VLBI observations in comparison to single dish measurements. However, assuming an uncertainty on the VLBI amplitude comparable large to the single dish measurement of NGC 1052 (e.g., of about 45%), the 86 GHz total flux density fit into the VLBA continuum spectrum. Still, the measurement is very inaccurate and can, hence, not be used to enlarge our knowledge on NGC 1052.

These finding show, that observations at a high frequency as 86 GHz are indeed very sensitive to the weather conditions and the source brightness. Still, NGC 1052 was detected at 86 GHz on March 31, 2017.

Additionally, NGC 1052 was observed with the EHT including ALMA in April 2017, the proposal was led by Prof. Dr. Kadler, Prof. Dr. Ros and myself. VLBI with EHT+ALMA at 1.4 mm will provide unprecedented angular resolution and sensitivity that are vital to directly investigate the region where both jets initially form in greater detail than any previous observation. The morphology, close proximity and strong radio emission makes NGC1052 a prime target to examine the formation of a jet powered by a supermassive black hole at scales of several hundreds of gravitational radii without Doppler boosting complications.

On April 6, there were five scans of 6 minutes each with ALMA, Pico Veleta, and South Pole Telescope and on April 7, there were four scans of 6 minutes with ALMA, South Pole Telescope, James Clerk Maxwell Telescope and the Submillimeter Array. The observations are still processed by the EHT collaboration. Presenting preliminary results is, therefore, not within the scope of this thesis. The observation campaign of the EHT in April 2017 led to the first image of a supermassive black hole in M 87 (EHT Collaboration et al. 2019a) as well as the first image of 3C 279 at 1.3 mm (EHT Collaboration et al. 2019b, and Kim et al. in preparation).

6 | Summary & Outlook

This thesis focuses on the innermost region of AGN in which jets are formed, accelerated and collimated. Several theoretical models aim to describe the different classes of AGN and their observables. A main focus is set on their highly collimated, relativistic moving jets, which span to distances up to Mpc. The regions which are mostly relevant in terms of these studies are only accessible by high-resolution observations accessible through VLBI.

This thesis aims to understand the physical processes leading to formation, acceleration and collimation of AGN jets in more detail. By combining high-resolution VLBI observations of the double-sided jet in NGC 1052 over a wide band of radio frequencies with simulations better constraints on theoretical models are provided. In this final chapter I will summarize the results and conclusions of my thesis and discuss how the different observations form a global picture of the twin-jets in NGC 1052.

Main results from multi-epoch VLBA observations of NGC 1052: NGC 1052 was observed at 22 GHz and 43 GHz from 2005 to 2009 involving 29 epochs. The main outcomes of the observations at 43 GHz can be summarized as:

- All images reveal a bright central feature and two jets up to distances of 4 mas from the center. Whereas both jets evolve fairly symmetric in the beginning, the morphology changes to asymmetric in early 2007. The extent of both jets shrinks to about 2 mas and the eastern jet is even shorter compared to the western jet.
- In contrast to previous estimates (see for example [Kameno et al. \(2001\)](#); [Vermeulen et al. \(2003\)](#); [Kadler et al. \(2004a\)](#); [Sawada-Satoh et al. \(2008\)](#)), the flux density of the western jet is higher than that of the eastern jet during the time of our observations. The flux density ratio of western to eastern jet rises from ~ 1.1 up to ~ 2.5 within the observational campaign.
- The mean apparent velocities of eastern and western jet are significant different with $\beta_{\text{wj}} = 0.343 \pm 0.037$ and $\beta_{\text{ej}} = 0.529 \pm 0.038$ for the western and eastern jet, respectively. In addition, the overall jet speeds are faster compared to estimates from lower frequencies ([Vermeulen et al. 2003](#); [Lister et al. 2013](#)). Based on the kinematic study the central feature is likely the dynamic center of the source.
- There is no consistent parameter space of intrinsic velocity and viewing angle for all observations assuming symmetric evolving jets.
- Based on the model-fit components the distribution of brightness temperatures and jet width as a function of the separation from the center was fitted assuming a power law. Whereas the jets seem to be quite collimated in the inner 1 mas, both evolve with a power law index of ~ 0.65 further out. The brightness temperature drops at 1 mas, which can be explained by a reduction of the flux density owing to absorption in the torus.

The combination of the 22 GHz and 43 GHz images lead to additional analysis targeting the spectral behaviour between these two frequencies:

- The spectral index maps between 22 GHz and 43 GHz show an absorbing structure covering the inner 1.5 mas, with a spectral index exceeding $\alpha = 2.5$. This is consistent with previous suggestions of an optically thick torus with a radius of about 5 mas (Kamenov et al. 2001).
- Stacked maps were produced at both frequencies to analyse the morphology and spectral behaviour with a smooth jet. The spectral index map based on the stacked images reveal a plateau-like feature in the western jet at around -2 mas.
- The most likely explanation for the observed differences between the eastern and the western jet are asymmetries either in the ambient medium or the jet. The observations fit well into a picture in which the western jet carries a larger internal energy and/or magnetic flux than the eastern jet, thus becoming brighter at these scales.
- The stacked images were used as input for special-relativity hydrodynamic (SRHD) simulations to model the relativistic jets in NGC 1052 (see Fromm et al. 2019). Non-thermal emission from the jet was taken into account as well as thermal absorption in the surrounding torus. Based on the simulations the calculated number density of $0.7\text{--}1.0 \times 10^{22} \text{ cm}^{-2}$ in the torus is consistent with values reported by Kadler et al. (2004b). Finally the uv sampling and imaging process was taken into account to compare the final simulation results with the VLBI observations. The jets are best modelled assuming a slightly over-pressured jet, hence, a pressure mismatch at the jet nozzle evolving into a decreasing-pressure ambient medium.

Main results from multi-frequency VLBA observations of NGC 1052: NGC 1052 had been observed at six frequencies between 1.5 GHz and 43 GHz with the VLBA in April 2017 and at 22 GHz with RadioAstron in November 2016.

- There were no fringes detected to RadioAstron, still the large ground-array from this observation delivers the highest North-South resolution at 22 GHz of the jets in NGC 1052 until now, resulting in a nearly circular beam.
- The observation support previous findings of an absorbing optically-thick structure, covering large parts of the western jet. There is an emission gap in between both jets, decreasing with increasing frequency
- By fitting a Gaussian function to slices perpendicular to the averaged jet stream line, the ridge-line had been derived for all frequency images for the VLBA as well as the RadioAstron ground array.
- There is a directional change in the western jet at about -2 mas, farther downstream at about -5 mas the jet stream line turns back to the original position angle. There is no comparable structure in the eastern jet.
- Except the directional change in the western jet, the ridge-line do not show any significant deviation from a straight line, which makes a precession very unlikely.
- A additional observable based on the Gaussian fitting to slices, is the width of the jet along its mean stream line. By comparing with the FWHM of the CLEAN beam along the slices both jets turn out to be unresolved for all images.

- Combining the very straight stream line and the bending of the western jet suggests asymmetries either in the jet or the ambient medium as most likely explanation for the observed properties.

GMVA observations of NGC 1052: In 2004, the jets in NGC 1052 were detected for the first time at 86 GHz with the GMVA (Baczko et al. 2016a). In 2017 the source was observed from 1.5 GHz up to 43 GHz with the VLBA, at 86 GHz with the GMVA, and at 230 GHz with the EHT. Even so the GMVA observation suffered from bad weather conditions and a faint source, NGC 1052 was detected. The final CLEAN image reveals a single feature, with no hints of the jets. The total recovered flux density has a untypically large amplitude uncertainty. Therefore, it could not be used to give a reasonable extension to the continuum spectrum obtained with the VLBA from 1.5 GHz to 43 GHz towards higher frequencies. Hence, it was not possible to obtain improved estimates on the source at 86 GHz compared to previous observations at this frequency. The EHT data are being processed within the EHT collaboration at the moment of submitting this work.

The big picture: All observations presented in this thesis reveal some kind of asymmetry between the western and the eastern jet. The kinematic study at 43 GHz resulted in overall faster velocities as compared to similar studies at lower frequencies (Vermeulen et al. 2003; Lister et al. 2019), suggesting a faster inner spine and a slower outer sheath. In addition, the apparent velocities differ for the eastern and the western jet, with the eastern jet moving faster. On the other hand, the western jet is brighter. A likely explanation suggests a larger internal energy and/or magnetic flux in the western jet, which, therefore, becomes brighter. Another hint towards intrinsic asymmetries is the fact, that it is not possible to find a common parameter space of intrinsic velocity and viewing angle for all 43 GHz observations between 2005 and 2009 and both jets.

Furthermore, there is a directional change of the jet stream line, which is only observed in the western jet. Besides this feature, the ridge-line is surprisingly straight and, therefore, offers no hints on Kelvin-Helmholtz instabilities. This makes it also very difficult to explain the observed asymmetries by a precessing jet nozzle. Combining all observational results, the most likely explanation for the differences between eastern and western jet is a kind of asymmetry, either intrinsic to the jet or arising from the ambient medium.

The absorbing effect of the molecular torus around the central engine and the base of the jets is supported by the observations and successfully modelled by the simulations (Fromm et al. 2019). Within both models the emission gap between the jets can be explained by free-free absorption in a geometrically thick structure, having close to no impact at 43 GHz and becomes optically thin at 86 GHz. Hence, observations at 86 GHz and above enable us to directly study the innermost region around the central engine and, therefore, the area of jet formation.

It is intriguing that the jet structure could not be resolved transversally by any of the presented observations. The jets seem to be very thin and straight and no opening angle different than zero could be derived within this work, even so there are hints on a conical expansion further outwards (Kovalev et al. 2019; Nakahara et al. 2019). Other nearby AGN with large

viewing angles draw a different picture. The three sources Cyg A, M 87, and 3C 84 show a very wide jet base as well as an edge brightening structure.

Outlook: It was not possible to resolve the twin-jet transversally to the stream line by any of the presented observations. Compared to other nearby sources as Cyg A, M 87, or 3C 84, in which a wide jet base was found, this kind of study for NGC 1052 will only be possible by reaching spatial resolutions able to estimate the true jet widths. This source is an exceptional case of a very thin and straight jet, with a viewing angle close to the plane of the sky. Whereas jets are typically assumed to evolve symmetrically, NGC 1052 reveals several asymmetries between eastern and western jet. More high-resolution studies, including Southern stations at high frequencies are decisive to study the innermost collimation region in NGC 1052. To narrow down possible origins of the asymmetries between both jets, numerical simulations allowing for asymmetries in the formation of both jets as well as in the ambient medium are needed. In addition, a larger fraction of sources revealing a double-sided jet must be observed at high angular resolutions to further investigate AGN jets within their formation region. Only by enlarging the sample of sources similar to Cyg A, M 87, 3C 84, and NGC 1052 it will be possible to investigate and understand the differences found in the ongoing research.

Bibliography

- Antonucci, R. 1993, *Annual Rev. Astron. Astrophys*, 31, 473
- Astropy Collaboration, Price-Whelan, A. M., Sipőcz, B. M., et al. 2018, *AJ*, 156, 123
- Astropy Collaboration, Robitaille, T. P., Tollerud, E. J., et al. 2013, *A&A*, 558, A33
- Baade, W. & Minkowski, R. 1954, *ApJ*, 119, 206
- Baczko, A.-K. 2015, Master's thesis, Friedrich-Alexander-Universität Erlangen-Nürnberg
- Baczko, A. K., Schulz, R., Kadler, M., et al. 2019, *A&A*, 623, A27
- Baczko, A.-K., Schulz, R., Kadler, M., et al. 2016a, *A&A*, 593, A47
- Baczko, A.-K., Schulz, R., Ros, E., et al. 2016b, *Galaxies*, 4, 48
- Bardeen, J. M. & Petterson, J. A. 1975, *ApJL*, 195, L65
- Beasley, A. J., Gordon, D., Peck, A. B., et al. 2002, *ApJS*, 141, 13
- Beckmann, V. & Shrader, C. 2012, in Proceedings of “An INTEGRAL view of the high-energy sky (the first 10 years)” - 9th INTEGRAL Workshop and celebration of the 10th anniversary of the launch (INTEGRAL 2012). 15-19 October 2012. Bibliothèque Nationale de France, 69
- Blandford, R., Meier, D., & Readhead, A. 2019, *Annual Rev. Astron. Astrophys*, 57, 467
- Blandford, R. D. & Payne, D. G. 1982, *MNRAS*, 199, 883
- Blandford, R. D. & Znajek, R. L. 1977, *MNRAS*, 179, 433
- Boccardi, B., Krichbaum, T. P., Bach, U., et al. 2016, *A&A*, 585, A33
- Böck, M. 2012, PhD thesis, Friedrich-Alexander-Universität Erlangen-Nürnberg
- Boggs, P. T. & Rogers, J. E. 1990, in Contemporary Mathematics Series, Vol. 112, Statistical analysis of measurement error models and applications: proceedings of the AMS-IMS-SIAM joint summer research conference held June 10-16, 1989, ed. P. Brown, W. Fuller, A. Society, I. Statistics, & S. Mathematics (American mathematical society), 186
- Bowman, M., Leahy, J. P., & Komissarov, S. S. 1996, *MNRAS*, 279, 899
- Brenneman, L. W., Weaver, K. A., Kadler, M., et al. 2009, *ApJ*, 698, 528

- Britzen, S., Fendt, C., Witzel, G., et al. 2018, MNRAS, 478, 3199
- Britzen, S., Qian, S.-J., Steffen, W., et al. 2017, A&A, 602, A29
- Burk, B. F. & Graham-Smith, F. 2009, *An Introduction to Radio Astronomy* (Cambridge University Press, New York)
- Caproni, A., Mosquera Cuesta, H. J., & Abraham, Z. 2004, ApJL, 616, L99
- Carroll, B. W. & Ostlie, D. A. 2017, *An introduction to modern astrophysics* 2nd edition (Cambridge University press, United Kingdom)
- Celotti, A. & Fabian, A. C. 1993, MNRAS, 264, 228
- Chael, A. A., Johnson, M. D., Bouman, K. L., et al. 2018, ApJ, 857, 23
- Chael, A. A., Johnson, M. D., Narayan, R., et al. 2016, ApJ, 829, 11
- Claussen, M. J., Diamond, P. J., Braatz, J. A., Wilson, A. S., & Henkel, C. 1998, ApJL, 500, L129
- Contopoulos, I., Nathanail, A., Sądowski, A., Kazanas, D., & Narayan, R. 2018, MNRAS, 473, 721
- Cornwell, T. & Fomalont, E. B. 1999, in *Astronomical Society of the Pacific Conference Series*, Vol. 180, *Synthesis Imaging in Radio Astronomy II*, ed. G. B. Taylor, C. L. Carilli, & R. A. Perley, 187
- Cotton, W. D. 1995, in *Astronomical Society of the Pacific Conference Series*, Vol. 82, *Very Long Baseline Interferometry and the VLBA*, ed. J. A. Zensus, P. J. Diamond, & P. J. Napier, 189
- Denicoló, G., Terlevich, R., Terlevich, E., et al. 2005, MNRAS, 356, 1440
- EHT Collaboration, Akiyama, K., Alberdi, A., et al. 2019a, ApJL, 875, L1
- EHT Collaboration, Akiyama, K., Alberdi, A., et al. 2019b, ApJL, 875, L4
- Engelbrecht, A. P. 2007, *Computational Intelligence: An Introduction* (John Wiley & Sons, Ltd, England)
- Falcke, H., Melia, F., & Agol, E. 2000, ApJL, 528, L13
- Fanaroff, B. L. & Riley, J. M. 1974, MNRAS, 167, 31P
- Fath, E. A. 1909, *Popular Astronomy*, 17, 504
- Fernández-Ontiveros, J. A., López-Gonzaga, N., Prieto, M. A., et al. 2019, MNRAS, 485, 5377

- Fomalont, E. B. 1999, in *Astronomical Society of the Pacific Conference Series*, Vol. 180, *Synthesis Imaging in Radio Astronomy II*, ed. G. B. Taylor, C. L. Carilli, & R. A. Perley, 301
- Forbes, D. A., Georgakakis, A. E., & Brodie, J. P. 2001, *MNRAS*, 325, 1431
- Fosbury, R. A. E., Mebold, U., Goss, W. M., & Dopita, M. A. 1978, *MNRAS*, 183, 549
- Fromm, C. M., Perucho, M., Porth, O., et al. 2018, *A&A*, 609, A80
- Fromm, C. M., Ros, E., Perucho, M., et al. 2013, *A&A*, 557, A105
- Fromm, C. M., Younsi, Z., Baczko, A., et al. 2019, *A&A*, 629, A4
- Ghisellini, G., Tavecchio, F., Maraschi, L., Celotti, A., & Sbarrato, T. 2014, *Nature*, 515, 376
- Giovannini, G., Savolainen, T., Orienti, M., et al. 2018, *Nature Astronomy*, 2, 472
- Greisen, E. 2011, *AIPS Cook Book*, ed. E. Greisen (The National Radio Astronomy Observatory)
- Greisen, E. W. 1990, in *Acquisition, Processing and Archiving of Astronomical Images*, 125–142
- Guizar-Sicairos, M., Thurman, S. T., & Fienup, J. R. 2008, *Opt. Lett.*, 33, 156
- Hardee, P. 2008, in *Journal of Physics Conference Series*, Vol. 131, 012052
- Hawley, J. F. & Krolik, J. H. 2006, *ApJ*, 641, 103
- Ho, L. C., Filippenko, A. V., & Sargent, W. L. W. 1997, *ApJS*, 112, 315
- Högbom, J. A. 1974, *A&AS*, 15, 417
- Homan, D. C., Ojha, R., Wardle, J. F. C., et al. 2002, *ApJ*, 568, 99
- Impellizzeri, V., Roy, A. L., & Henkel, C. 2008, in *Proceedings of “The role of VLBI in the Golden Age for Radio Astronomy” – 9th EVN Symposium. 23-26 September 2008. Bologna, Italy.*, Vol. 9, 33
- Jansky, K. G. 1933, *Popular Astronomy*, 41, 548
- Kadler, M., Kerp, J., Ros, E., et al. 2004a, *A&A*, 420, 467
- Kadler, M., Ros, E., Lobanov, A. P., Falcke, H., & Zensus, J. A. 2004b, *A&A*, 426, 481
- Kamenno, S., Nakai, N., Sawada-Satoh, S., Sato, N., & Haba, A. 2005, *ApJ*, 620, 145
- Kamenno, S., Sawada-Satoh, S., Inoue, M., Shen, Z.-Q., & Wajima, K. 2001, *PASJ*, 53, 169
- Kellermann, K. I., Sramek, R., Schmidt, M., Shaffer, D. B., & Green, R. 1989, *AJ*, 98, 1195

- Kellermann, K. I., Vermeulen, R. C., Cohen, M. H., & Zensus, J. A. 1999, in *Bulletin of the American Astronomical Society*, Vol. 31, American Astronomical Society Meeting Abstracts #194, 856
- Kerr, R. P. 1963, *Physical Review Letters*, 11, 237
- Kettenis, M., van Langevelde, H. J., Reynolds, C., & Cotton, B. 2006, in *Astronomical Society of the Pacific Conference Series*, Vol. 351, *Astronomical Data Analysis Software and Systems XV*, ed. C. Gabriel, C. Arviset, D. Ponz, & S. Enrique, 497
- Kim, J. Y., Krichbaum, T. P., Lu, R. S., et al. 2018, *A&A*, 616, A188
- Kim, J. Y., Krichbaum, T. P., Marscher, A. P., et al. 2019, *A&A*, 622, A196
- Kovalev, Y. Y., Kardashev, N. S., Kellermann, K. I., et al. 2016, *ApJL*, 820, L9
- Kovalev, Y. Y., Kellermann, K. I., Lister, M. L., et al. 2005, *AJ*, 130, 2473
- Kovalev, Y. Y., Pushkarev, A. B., Nokhrina, E. E., et al. 2019, *arXiv e-prints*, arXiv:1907.01485
- Krolik, J. H. 1999, *Active galactic nuclei : from the central black hole to the galactic environment* (Princeton University Press, Princeton)
- Lister, M. L., Aller, M. F., Aller, H. D., et al. 2013, *AJ*, 146, 120
- Lister, M. L., Cohen, M. H., Homan, D. C., et al. 2009, *AJ*, 138, 1874
- Lister, M. L., Homan, D. C., Hovatta, T., et al. 2019, *ApJ*, 874, 43
- Liszt, H. & Lucas, R. 2004, *A&A*, 428, 445
- Liu, S. & Melia, F. 2002, *ApJL*, 573, L23
- Machalski, J., Jamrozy, M., Stawarz, Ł., & Weżgowiec, M. 2016, *A&A*, 595, A46
- Margon, B. & Anderson, S. F. 1989, *ApJ*, 347, 448
- Marscher, A. P. 2009, *arXiv e-prints*, arXiv:0909.2576
- Martí-Vidal, I., Marcaide, J. M., Alberdi, A., et al. 2011, *A&A*, 533, A111
- Matveyenko, L. I. & Sivakov, S. S. 2013, *Astronomy Letters*, 39, 481
- Mayall, N. U. 1939, *PASP*, 51, 282
- Meier, D. L., Koide, S., & Uchida, Y. 2001, *Science*, 291, 84
- Mertens, F., Lobanov, A. P., Walker, R. C., & Hardee, P. E. 2016, *A&A*, 595, A54
- Mohan, P., An, T., Frey, S., et al. 2016, *MNRAS*, 463, 1812

- Nakahara, S., Doi, A., Murata, Y., et al. 2019, arXiv e-prints, arXiv:1909.12510
- Omar, A., Anantharamaiah, K. R., Rupen, M., & Rigby, J. 2002, *A&A*, 381, L29
- Pacholczyk, A. G. 1970, *Radio astrophysics. Nonthermal processes in galactic and extragalactic sources* (W. H. Freeman and Co., San Francisco)
- Parfrey, K., Giannios, D., & Beloborodov, A. M. 2015, *MNRAS*, 446, L61
- Penrose, R. & Floyd, R. M. 1971, *Nature Physical Science*, 229, 177
- Perley, R. A. & Meisenheimer, K. 2017, *A&A*, 601, A35
- Perucho, M., Martí, J. M., Laing, R. A., & Hardee, P. E. 2014, *MNRAS*, 441, 1488
- Perucho, M., Martí-Vidal, I., Lobanov, A. P., & Hardee, P. E. 2012, *A&A*, 545, A65
- Petrov, L., Kovalev, Y. Y., Fomalont, E. B., & Gordon, D. 2011, *AJ*, 142, 35
- Pierce, M., Brodie, J. P., Forbes, D. A., et al. 2005, *MNRAS*, 358, 419
- Pushkarev, A. B., Kovalev, Y. Y., Lister, M. L., & Savolainen, T. 2017, *MNRAS*, 468, 4992
- Reb, L., Fernández-Ontiveros, J. A., Prieto, M. A., & Dolag, K. 2018, *MNRAS*, 478, L122
- Reynolds, C. S., Fabian, A. C., Celotti, A., & Rees, M. J. 1996, *MNRAS*, 283, 873
- Richards, J. L., Max-Moerbeck, W., Pavlidou, V., et al. 2011, *ApJS*, 194, 29
- Rozgonyi, K. & Frey, S. 2016, *Galaxies*, 4, 10
- Rubinur, K., Das, M., Kharb, P., & Honey, M. 2017, *MNRAS*, 465, 4772
- Rybicki, G. B. & Lightman, A. P. 1979, *Radiative processes in astrophysics* (Wiley-VCH, New York)
- Ryle, M. & Hewish, A. 1960, *MNRAS*, 120, 220
- Sawada-Satoh, S., Kamenno, S., Nakamura, K., et al. 2008, *ApJ*, 680, 191
- Sawada-Satoh, S., Roh, D.-G., Oh, S.-J., et al. 2016, *ApJL*, 830, L3
- Schmidt, M. 1963, *Nature*, 197, 1040
- Seyfert, C. K. 1943, *ApJ*, 97, 28
- Shepherd, M. C., Pearson, T. J., & Taylor, G. B. 1994, in *Bulletin of the American Astronomical Society*, Vol. 26, BAAS, 987–989
- Taylor, G. B., Carilli, C. L., & Perley, R. A., eds. 1999, *Astronomical Society of the Pacific Conference Series*, Vol. 180, *Synthesis Imaging in Radio Astronomy II*

- Tchekhovskoy, A. 2015, in *Astrophysics and Space Science Library*, Vol. 414, *The Formation and Disruption of Black Hole Jets*, ed. I. Contopoulos, D. Gabuzda, & N. Kylafis, 45
- Tchekhovskoy, A. & Bromberg, O. 2016, *MNRAS*, 461, L46
- Thompson, A. R., Moran, J. M., & Swenson, George W., J. 2017, *Interferometry and Synthesis in Radio Astronomy*, 3rd Edition (*Astronomy and Astrophysics Library*)
- Tully, R. B., Courtois, H. M., Dolphin, A. E., et al. 2013, *AJ*, 146, 86
- Türler, M., Courvoisier, T. J. L., & Paltani, S. 1999, *A&A*, 349, 45
- Urry, C. M. & Padovani, P. 1995, *PASP*, 107, 803
- Valtonen, M., Kidger, M., Lehto, H., & Poyner, G. 2008, *A&A*, 477, 407
- van Cittert, P. H. 1934, *Physica*, 1, 201
- van der Walt, S., Schönberger, J. L., Nunez-Iglesias, J., et al. 2014, *PeerJ*
- van Gorkom, J. H., Knapp, G. R., Raimond, E., Faber, S. M., & Gallagher, J. S. 1986a, *AJ*, 91, 791
- van Gorkom, J. H., Knapp, G. R., Raimond, E., Faber, S. M., & Gallagher, J. S. 1986b, *AJ*, 91, 791
- Vega-García, L. 2018, PhD thesis, Universität zu Köln
- Vega-García, L., Perucho, M., & Lobanov, A. P. 2019, *A&A*, 627, A79
- Vermeulen, R. C., Ros, E., Kellermann, K. I., et al. 2003, *A&A*, 401, 113
- Virtanen, P., Gommers, R., Oliphant, T. E., et al. 2019, *arXiv e-prints*, arXiv:1907.10121
- Wilson, T. L., Rohlfs, K., & Huttemeister, S. 2009, *Tools of Radio Astronomy*, 5th edition (Springer-Verlag, Berlin Heidelberg)
- Woo, J.-H. & Urry, C. M. 2002, *ApJ*, 579, 530
- Wrobel, J. M. 1984, *ApJ*, 284, 531
- Zensus, J. A. 1997, *Annual Rev. Astron. Astrophys*, 35, 607
- Zernike, F. 1938, *Physica*, 5, 785

A | VLBA multi-epoch observation – parameters and additional figures

Here addition material for Chapter 3 is presented. Tables A.1 to A.8 list the component parameters for all epochs. The parameters for the CLEAN maps are shown in Tab. 3.1.

Table A.1.: Parameters for all components of epochs BR099A and BR099C (from top to bottom). Delta-like components with an unphysical high brightness temperature larger than 10^{18} K have been excluded for each analysis based on brightness temperatures.

Component	S_{tot} [Jy]	Distance [mas]	P.A. [°]	Major [mas]	Ratio	$\log T_b$ [K]
wj1	0.07	-2.36	–	0.36	1.00	8.56
wj2	0.09	-1.81	–	0.28	1.00	8.89
wj4	0.08	-1.16	–	0.21	1.00	9.07
–	0.05	-0.61	23.84	0.50	0.27	8.73
core	0.38	0.00	43.83	0.15	0.00	–
ej3	0.08	0.59	–	0.40	1.00	8.50
ej2	0.07	1.12	–	0.30	1.00	8.68
ej1	0.04	1.66	–	0.33	1.00	8.38
–	0.06	2.28	40.86	0.65	0.58	8.24
Component	S_{tot} [Jy]	Distance [mas]	P.A. [°]	Major [mas]	Ratio	$\log T_b$ [K]
wj1	0.05	-2.80	–	0.47	1.00	8.16
wj2	0.12	-2.18	–	0.34	1.00	8.85
wj3	0.08	-1.79	–	0.15	1.00	9.36
wj4	0.09	-1.41	–	0.36	1.00	8.68
wj5	0.11	-0.47	–	0.30	1.00	8.92
core	0.43	0.00	5.50	0.13	0.39	10.63
ej4	0.07	0.48	–	0.07	1.00	9.96
ej3	0.15	0.82	–	0.28	1.00	9.10
ej2	0.05	1.53	–	0.50	1.00	8.12
ej1	0.03	2.19	–	0.18	1.00	8.71
–	0.03	2.58	–	0.22	1.00	8.58

Table A.2.: Parameters for all components of epoch BR099D, BR099E, and BR099F (from top to bottom). Delta-like components with an unphysical high brightness temperature larger than 10^{18} K have been excluded for each analysis based on brightness temperatures.

Component	S_{tot} [Jy]	Distance [mas]	P.A. [°]	Major [mas]	Ratio	$\log T_b$ [K]
wj1	0.02	-3.13	–	0.21	1.00	8.38
wj2	0.08	-2.40	–	0.39	1.00	8.53
wj3	0.08	-1.92	–	0.23	1.00	9.02
wj4	0.06	-1.49	–	0.32	1.00	8.62
wj5	0.05	-0.78	–	0.36	1.00	8.46
wj6	0.09	-0.31	–	0.31	1.00	8.82
core	0.31	0.00	18.66	0.10	0.00	–
ej5	0.12	0.27	–	0.41	1.00	8.66
ej4	0.08	0.78	–	0.23	1.00	9.04
ej3	0.06	1.24	–	0.37	1.00	8.45
ej2	0.05	1.87	–	0.52	1.00	8.04
ej1	0.05	2.50	–	0.44	1.00	8.23
Component	S_{tot} [Jy]	Distance [mas]	P.A. [°]	Major [mas]	Ratio	$\log T_b$ [K]
wj1	0.02	-3.23	–	0.29	1.00	8.23
wj2	0.09	-2.51	–	0.32	1.00	8.77
wj3	0.16	-1.99	–	0.29	1.00	9.11
wj4	0.09	-1.57	–	0.31	1.00	8.82
wj5	0.07	-0.82	–	0.24	1.00	8.87
wj6	0.19	-0.34	–	0.35	1.00	9.02
core	0.48	0.00	12.03	0.18	0.00	–
ej5	0.15	0.31	–	0.37	1.00	8.87
ej4	0.14	0.81	–	0.27	1.00	9.11
ej3	0.09	1.35	–	0.41	1.00	8.54
ej2	0.08	2.07	–	0.43	1.00	8.42
ej1	0.04	2.57	–	0.29	1.00	8.47
Component	S_{tot} [Jy]	Distance [mas]	P.A. [°]	Major [mas]	Ratio	$\log T_b$ [K]
wj2	0.08	-2.67	–	0.47	1.00	8.37
wj3	0.11	-2.07	–	0.32	1.00	8.85
wj4	0.06	-1.59	–	0.18	1.00	9.07
wj5	0.06	-1.04	–	0.23	1.00	8.91
wj6	0.10	-0.50	–	0.15	1.00	9.51
core	0.53	0.00	–	0.08	1.00	10.74
ej5	0.14	0.58	–	0.42	1.00	8.72
ej4	0.08	1.19	–	0.24	1.00	8.95
ej3	0.07	1.74	–	0.32	1.00	8.66
ej2	0.07	2.32	–	0.43	1.00	8.38
ej1	0.04	2.92	–	0.37	1.00	8.34

Table A.3.: Parameters for all components of epoch BR099G, BR099I, and BR119A (from top to bottom). Delta-like components with an unphysical high brightness temperature larger than 10^{18} K have been excluded for each analysis based on brightness temperatures.

Component	S_{tot} [Jy]	Distance [mas]	P.A. [$^{\circ}$]	Major [mas]	Ratio	$\log T_b$ [K]
wj2	0.02	-2.88	–	0.17	1.00	8.61
wj3	0.07	-2.17	–	0.38	1.00	8.52
wj4	0.05	-1.71	–	0.25	1.00	8.71
wj5	0.05	-1.33	–	0.27	1.00	8.64
wj6	0.09	-0.55	–	0.52	1.00	8.35
core	0.30	0.00	–	0.09	1.00	10.40
ej6	0.04	0.50	–	0.11	1.00	9.37
ej5	0.08	0.82	–	0.35	1.00	8.64
ej4	0.05	1.33	–	0.25	1.00	8.76
ej3	0.05	1.96	–	0.55	1.00	8.03
ej2	0.04	2.73	–	0.58	1.00	7.87
Component	S_{tot} [Jy]	Distance [mas]	P.A. [$^{\circ}$]	Major [mas]	Ratio	$\log T_b$ [K]
wj2	0.02	-3.16	–	0.47	1.00	7.88
wj3	0.07	-2.22	–	0.42	1.00	8.41
wj5	0.06	-1.66	–	0.28	1.00	8.70
wj6	0.05	-0.83	–	0.30	1.00	8.62
wj7	0.03	-0.48	–	0.00	1.00	–
core	0.36	0.00	–	0.07	1.00	10.68
ej7	0.04	0.46	–	0.00	1.00	–
ej6	0.05	0.77	–	0.16	1.00	9.15
ej5	0.02	1.26	–	0.00	1.00	20.05
ej4	0.05	1.62	–	0.27	1.00	8.64
ej3	0.02	2.14	–	0.19	1.00	8.63
ej2	0.03	2.93	–	0.45	1.00	7.99
Component	S_{tot} [Jy]	Distance [mas]	P.A. [$^{\circ}$]	Major [mas]	Ratio	$\log T_b$ [K]
wj3	0.05	-2.41	–	0.57	1.00	8.03
wj5	0.06	-1.80	–	0.36	1.00	8.47
wj6	0.05	-1.12	–	0.23	1.00	8.81
wj7	0.06	-0.58	–	0.48	1.00	8.24
core	0.44	0.00	40.59	0.09	0.00	18.64
ej7	0.06	0.69	–	0.36	1.00	8.48
ej6	0.04	1.16	–	0.17	1.00	8.94
ej5	0.03	1.60	–	0.33	1.00	8.29
ej4	0.04	2.03	–	0.38	1.00	8.24
ej2	0.04	3.22	–	0.75	1.00	7.65

Table A.4.: Parameters for all components of epoch BR119B, BR120A, BR120B, and BR120C (from top to bottom). Delta-like components with an unphysical high brightness temperature larger than 10^{18} K have been excluded for each analysis based on brightness temperatures.

Component	S_{tot} [Jy]	Distance [mas]	P.A. [$^{\circ}$]	Major [mas]	Ratio	$\log T_b$ [K]
wj2	0.02	-3.60	–	0.66	1.00	7.44
wj3	0.06	-2.49	–	0.52	1.00	8.14
wj5	0.06	-1.91	–	0.36	1.00	8.50
wj6	0.12	-1.09	–	0.43	1.00	8.64
wj7	0.03	-0.80	–	0.13	1.00	9.02
–	0.09	-0.28	–	0.34	1.00	8.71
core	0.42	0.00	12.03	0.14	0.00	–
–	0.04	0.22	–	0.05	1.00	10.03
–	0.04	0.44	–	0.08	1.00	9.57
ej7	0.05	0.79	–	0.29	1.00	8.62
ej6	0.06	1.23	–	0.31	1.00	8.60
ej5	0.06	1.83	–	0.49	1.00	8.23
ej3	0.06	2.82	–	0.79	1.00	7.79
ej1	0.02	3.91	–	0.50	1.00	7.68

Component	S_{tot} [Jy]	Distance [mas]	P.A. [$^{\circ}$]	Major [mas]	Ratio	$\log T_b$ [K]
–	0.02	-3.37	–	0.49	1.00	7.75
–	0.03	-2.27	–	0.21	1.00	8.72
wj8	0.09	-1.43	–	0.18	1.00	9.25
wj9	0.13	-0.72	–	0.32	1.00	8.93
core	0.32	0.00	–	0.18	1.00	9.81
–	0.14	0.69	–	0.32	1.00	8.95
–	0.02	2.30	–	0.08	1.00	9.34
–	0.02	3.48	–	0.27	1.00	8.14

Component	S_{tot} [Jy]	Distance [mas]	P.A. [$^{\circ}$]	Major [mas]	Ratio	$\log T_b$ [K]
wj8	0.05	-1.60	–	0.35	1.00	8.48
wj9	0.11	-0.98	–	0.15	1.00	9.55
wj10	0.07	-0.21	–	0.26	1.00	8.87
core	0.28	0.00	26.09	0.14	0.62	10.21
ej9	0.14	0.66	73.04	0.35	0.27	9.44
ej8	0.01	1.45	–	0.08	1.00	8.93

Component	S_{tot} [Jy]	Distance [mas]	P.A. [$^{\circ}$]	Major [mas]	Ratio	$\log T_b$ [K]
wj8	0.03	-1.80	–	0.32	1.00	8.27
wj9	0.06	-1.16	–	0.22	1.00	8.93
wj10	0.07	-0.36	–	0.46	1.00	8.32
core	0.27	0.00	28.12	0.10	0.28	10.83
ej10	0.02	0.51	–	0.16	1.00	8.76
ej9	0.05	0.80	–	0.48	1.00	8.12

Table A.5.: Parameters for all components of epoch BR120D, BR120E, BR120F, BR120H and (from top to bottom). Delta-like components with an unphysical high brightness temperature larger than 10^{18} K have been excluded for each analysis based on brightness temperatures.

Component	S_{tot} [Jy]	Distance [mas]	P.A. [$^{\circ}$]	Major [mas]	Ratio	$\log T_b$ [K]
wj8	0.04	-1.93	–	0.38	1.00	8.23
wj9	0.08	-1.22	–	0.40	1.00	8.51
wj10	0.07	-0.46	–	0.29	1.00	8.71
–	0.03	-0.18	–	0.00	1.00	20.59
core	0.33	0.00	49.60	0.08	0.00	–
ej10	0.09	0.62	–	0.55	1.00	8.31
Component	S_{tot} [Jy]	Distance [mas]	P.A. [$^{\circ}$]	Major [mas]	Ratio	$\log T_b$ [K]
wj8	0.02	-2.02	–	0.30	1.00	8.15
–	0.03	-1.62	–	0.25	1.00	8.52
wj9	0.04	-1.23	–	0.25	1.00	8.69
wj10	0.06	-0.53	–	0.35	1.00	8.51
–	0.04	-0.20	-4.58	0.24	0.30	9.12
core	0.27	0.00	20.67	0.09	0.00	–
–	0.02	0.21	–	0.09	1.00	9.22
ej10	0.05	0.63	–	0.37	1.00	8.40
ej9	0.01	1.07	–	0.20	1.00	8.30
ej8	0.01	1.96	–	0.70	1.00	7.24
–	0.01	3.41	-19.34	0.93	0.48	7.32
Component	S_{tot} [Jy]	Distance [mas]	P.A. [$^{\circ}$]	Major [mas]	Ratio	$\log T_b$ [K]
–	0.02	-3.03	–	0.95	1.00	7.11
wj9	0.08	-1.69	–	0.17	1.00	9.28
wj10	0.12	-0.90	–	0.34	1.00	8.85
core	0.33	0.00	–	0.17	1.00	9.88
ej10	0.09	0.72	–	0.36	1.00	8.65
ej8	0.01	1.92	–	0.28	1.00	7.95
Component	S_{tot} [Jy]	Distance [mas]	P.A. [$^{\circ}$]	Major [mas]	Ratio	$\log T_b$ [K]
–	0.01	-2.25	–	0.40	1.00	7.63
wj11	0.06	-1.63	-22.40	0.25	0.84	8.87
wj12	0.14	-1.05	-85.65	0.21	0.51	9.62
wj13	0.02	-0.55	–	0.20	1.00	8.43
wj14	0.01	-0.22	–	0.00	1.00	23.31
core	0.33	0.00	80.64	0.20	0.52	10.04
ej12	0.14	0.56	–	0.32	1.00	8.97
ej11	0.03	1.32	–	0.46	1.00	7.91

Table A.6.: Parameters for all components of epoch BR120I, BR130A, BR130B, and BR130C (from top to bottom). Delta-like components with an unphysical high brightness temperature larger than 10^{18} K have been excluded for each analysis based on brightness temperatures.

Component	S_{tot} [Jy]	Distance [mas]	P.A. [°]	Major [mas]	Ratio	$\log T_b$ [K]
wj11	0.05	-1.78	48.69	0.51	0.20	8.83
wj12	0.04	-1.24	–	0.22	1.00	8.68
wj13	0.03	-0.84	–	0.21	1.00	8.64
wj14	0.05	-0.37	–	0.32	1.00	8.54
core	0.26	0.00	–	0.00	1.00	22.56
ej13	0.05	0.40	–	0.26	1.00	8.67
ej12	0.04	0.81	–	0.22	1.00	8.72
ej11	0.03	1.62	–	0.70	1.00	7.55
Component	S_{tot} [Jy]	Distance [mas]	P.A. [°]	Major [mas]	Ratio	$\log T_b$ [K]
wj11	0.10	-1.65	–	0.33	1.00	8.77
wj12	0.06	-1.12	–	0.12	1.00	9.42
wj13	0.02	-0.78	–	0.00	1.00	21.76
wj14	0.10	-0.41	–	0.30	1.00	8.86
core	0.29	0.00	40.50	0.08	0.00	–
ej12	0.12	0.55	–	0.37	1.00	8.77
ej11	0.02	1.68	–	0.16	1.00	8.73
Component	S_{tot} [Jy]	Distance [mas]	P.A. [°]	Major [mas]	Ratio	$\log T_b$ [K]
wj11	0.06	-1.92	–	0.34	1.00	8.55
wj12	0.07	-1.36	–	0.32	1.00	8.65
wj13	0.03	-0.85	–	0.26	1.00	8.53
wj14	0.08	-0.39	–	0.36	1.00	8.61
core	0.28	0.00	27.61	0.13	0.00	–
ej13	0.06	0.38	–	0.33	1.00	8.56
ej12	0.05	0.83	–	0.28	1.00	8.60
ej11	0.02	1.70	–	0.80	1.00	7.39
Component	S_{tot} [Jy]	Distance [mas]	P.A. [°]	Major [mas]	Ratio	$\log T_b$ [K]
wj11	0.05	-1.92	–	0.31	1.00	8.55
wj12	0.05	-1.48	–	0.27	1.00	8.63
wj13	0.04	-0.91	–	0.32	1.00	8.47
wj14	0.05	-0.46	–	0.28	1.00	8.68
core	0.37	0.00	19.85	0.12	0.00	–
ej13	0.03	0.46	–	0.10	1.00	9.23
ej12	0.07	0.86	–	0.40	1.00	8.45
ej11	0.02	1.80	–	0.74	1.00	7.34

Table A.7.: Parameters for all components of epoch BR130D, BR130E, and BR130F (from top to bottom). Delta-like components with an unphysical high brightness temperature larger than 10^{18} K have been excluded for each analysis based on brightness temperatures.

Component	S_{tot} [Jy]	Distance [mas]	P.A. [$^{\circ}$]	Major [mas]	Ratio	$\log T_b$ [K]
wj11	0.05	-2.05	–	0.31	1.00	8.49
wj12	0.08	-1.53	–	0.32	1.00	8.71
wj13	0.04	-1.07	–	0.23	1.00	8.69
wj14	0.09	-0.36	–	0.37	1.00	8.62
core	0.31	0.00	-24.93	0.02	0.00	–
ej14	0.02	0.20	–	0.00	1.00	21.95
ej13	0.08	0.60	–	0.46	1.00	8.42
ej12	0.02	1.14	–	0.21	1.00	8.56
ej11	0.03	2.02	–	0.91	1.00	7.34
Component	S_{tot} [Jy]	Distance [mas]	P.A. [$^{\circ}$]	Major [mas]	Ratio	$\log T_b$ [K]
wj11	0.03	-2.18	–	0.39	1.00	8.18
wj12	0.05	-1.75	–	0.23	1.00	8.83
wj13	0.14	-1.39	–	0.15	1.00	9.60
wj14	0.05	-0.71	–	0.43	1.00	8.23
wj15	0.13	-0.21	–	0.19	1.00	9.39
core	0.09	0.00	-14.80	0.14	0.42	9.85
ej14	0.22	0.34	–	0.37	1.00	9.01
ej13	0.05	0.91	–	0.18	1.00	9.02
ej12	0.03	1.20	–	0.15	1.00	8.92
Component	S_{tot} [Jy]	Distance [mas]	P.A. [$^{\circ}$]	Major [mas]	Ratio	$\log T_b$ [K]
wj11	0.02	-2.17	–	0.22	1.00	8.50
wj12	0.04	-1.85	–	0.14	1.00	9.17
wj13	0.11	-1.50	–	0.19	1.00	9.30
wj14	0.05	-0.91	–	0.10	1.00	9.54
wj15	0.14	-0.24	–	0.16	1.00	9.56
core	0.14	0.00	–	0.14	1.00	9.68
ej14	0.12	0.41	–	0.28	1.00	9.03
ej13	0.08	0.94	–	0.32	1.00	8.70
ej12	0.02	1.44	–	0.42	1.00	7.82

Table A.8.: Parameters for all components of epoch BR130G, BR130H, and BR130I(from top to bottom). Delta-like components with an unphysical high brightness temperature larger than 10^{18} K have been excluded for each analysis based on brightness temperatures.

Component	S_{tot} [Jy]	Distance [mas]	P.A. [°]	Major [mas]	Ratio	$\log T_b$ [K]
wj12	0.05	-1.95	–	0.25	1.00	8.70
wj13	0.09	-1.51	–	0.19	1.00	9.20
wj14	0.07	-0.89	–	0.07	1.00	9.93
wj15	0.08	-0.30	–	0.11	1.00	9.65
core	0.16	0.00	–	0.01	1.00	11.73
ej15	0.11	0.26	–	0.10	1.00	9.90
ej14	0.08	0.70	–	0.24	1.00	9.00
ej13	0.06	1.23	–	0.36	1.00	8.46
Component	S_{tot} [Jy]	Distance [mas]	P.A. [°]	Major [mas]	Ratio	$\log T_b$ [K]
wj11	0.01	-2.33	–	0.20	1.00	8.38
wj12	0.02	-2.06	–	0.23	1.00	8.42
wj13	0.08	-1.73	–	0.22	1.00	9.02
wj14	0.09	-1.04	–	0.15	1.00	9.41
wj15	0.06	-0.36	–	0.15	1.00	9.25
core	0.28	0.00	53.49	0.34	0.15	10.04
ej14	0.05	0.68	–	0.33	1.00	8.45
ej13	0.05	1.09	–	0.41	1.00	8.34
Component	S_{tot} [Jy]	Distance [mas]	P.A. [°]	Major [mas]	Ratio	$\log T_b$ [K]
wj12	0.04	-2.18	–	0.39	1.00	8.22
wj13	0.06	-1.80	–	0.20	1.00	8.97
–	0.02	-1.31	–	0.12	1.00	9.08
wj14	0.07	-1.16	–	0.08	1.00	9.91
wj15	0.07	-0.42	–	0.32	1.00	8.68
core	0.28	0.00	54.02	0.26	0.19	10.15
–	0.04	0.36	–	0.26	1.00	8.56
–	0.01	0.62	–	0.00	1.00	21.90
ej14	0.05	0.96	–	0.34	1.00	8.45
ej13	0.01	1.45	–	0.16	1.00	8.57

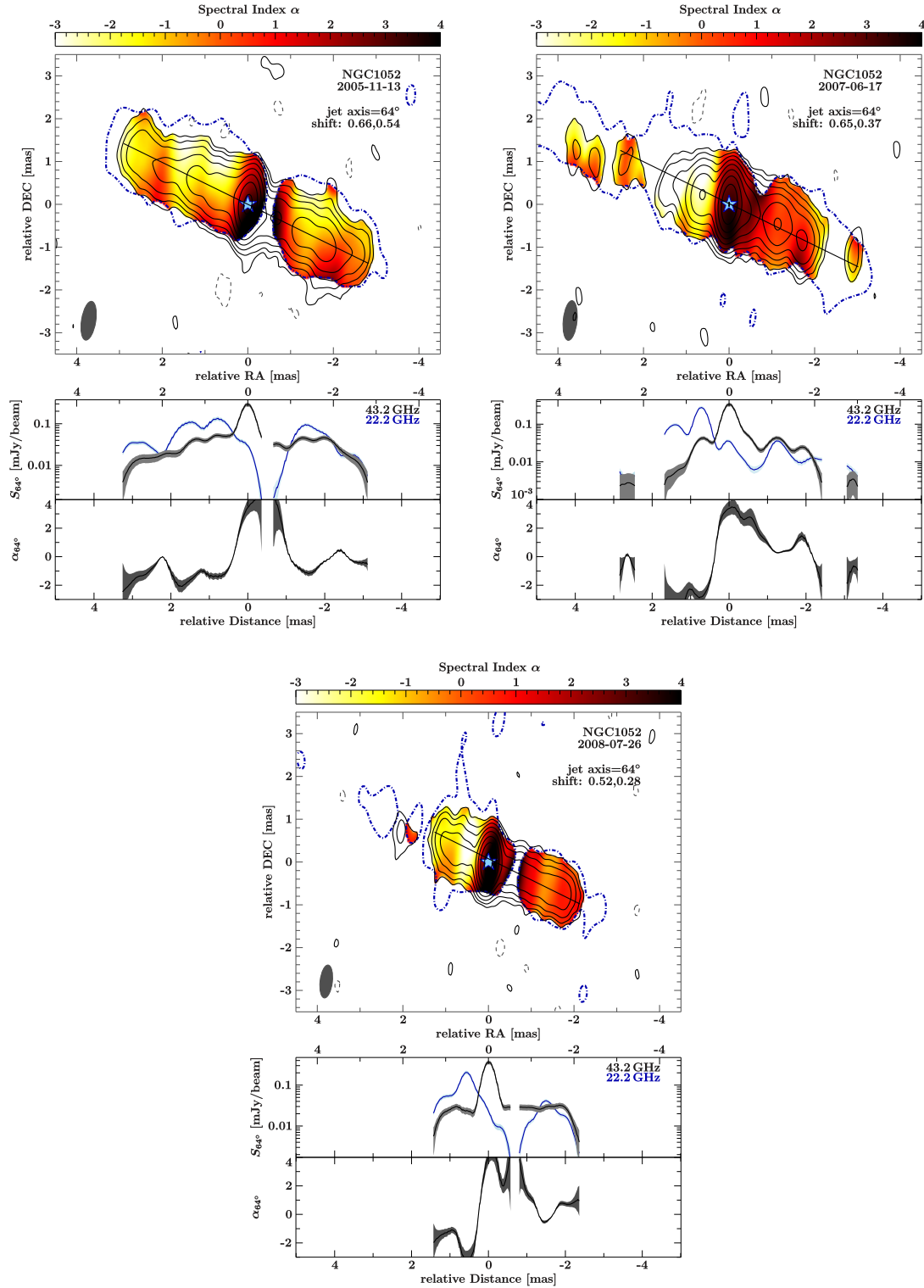


Figure A.1.: Spectral index maps between 22 GHz (dot-dashed blue contour) and 43 GHz (solid black contours) for three selected observations of the monitoring campaign after alignment based on optically thin features (compare Fig. 3.5). The restoring beam for each epoch is plotted in the lower left corner. A cut along the direction of the jets (64°) results in the bottom panels, showing the spectral index (bottom panels) and the flux density (middle panel) along the jet axis. The blue star indicates the assumed location of the dynamical center.

Table A.9.: Calculated velocities (v) and ejection times (t_{ej}) for the individual components including errors.

ID	v [mas/yr]	β_{app} [c]	t_{ej} [yr]
ej1	2.12 ± 0.11	0.64 ± 0.04	2004.95 ± 0.05
ej2	2.16 ± 0.06	0.65 ± 0.02	2005.17 ± 0.02
ej3	2.03 ± 0.14	0.62 ± 0.05	2005.51 ± 0.04
ej4	1.91 ± 0.13	0.58 ± 0.04	2005.54 ± 0.03
ej5	2.15 ± 0.15	0.65 ± 0.05	2005.84 ± 0.03
ej6	1.79 ± 0.26	0.54 ± 0.08	2005.80 ± 0.06
ej7	–	–	–
ej8	–	–	–
ej9	–	–	–
ej10	0.45 ± 0.11	0.14 ± 0.04	2006.39 ± 0.27
ej11	1.71 ± 0.10	0.52 ± 0.03	2007.70 ± 0.05
ej12	1.25 ± 0.13	0.38 ± 0.04	2008.16 ± 0.06
ej13	1.18 ± 0.10	0.36 ± 0.03	2008.56 ± 0.05
ej14	1.21 ± 0.13	0.37 ± 0.04	2008.84 ± 0.05
ej15	–	–	–
wj1	-2.15 ± 0.14	0.65 ± 0.05	2004.32 ± 0.08
wj2	-1.60 ± 0.04	0.48 ± 0.01	2004.61 ± 0.03
wj3	-0.75 ± 0.05	0.23 ± 0.02	2003.45 ± 0.16
wj4	-0.76 ± 0.08	0.23 ± 0.03	2003.95 ± 0.17
wj5	-1.73 ± 0.10	0.53 ± 0.03	2005.57 ± 0.04
wj6	-1.18 ± 0.10	0.36 ± 0.03	2005.70 ± 0.05
wj7	–	–	–
wj8	-1.03 ± 0.08	0.31 ± 0.03	2005.91 ± 0.11
wj9	-0.81 ± 0.19	0.25 ± 0.06	2006.34 ± 0.26
wj10	-0.80 ± 0.13	0.24 ± 0.04	2007.19 ± 0.07
wj11	-0.78 ± 0.08	0.24 ± 0.03	2006.61 ± 0.21
wj12	-1.10 ± 0.05	0.33 ± 0.02	2007.79 ± 0.05
wj13	-1.17 ± 0.06	0.36 ± 0.02	2008.24 ± 0.04
wj14	-0.86 ± 0.07	0.26 ± 0.03	2008.50 ± 0.06
wj15	-0.44 ± 0.02	0.13 ± 0.01	2008.57 ± 0.03

Table A.10.: Values of reduce chi square from Difmap for Gaussian model fitting, by comparing the final Gaussian model to the raw visibility data. Ideally the reduced χ^2_{red} should be equal to 1. As presented in the table, a few observations have $\chi^2_{\text{red}} < 1$, which suggests an over-fitting of the data (for example too deep cleaning) or an over-estimation of the errors. Probably another weighting of the relevant observations would lead to a more accurate result.

Epoch	χ^2_{red}	Epoch	χ^2_{red}
BR099A	1.06	BR120E	1.02
BR099C	0.93	BR120F	0.65
BR099D	1.07	BR120G	1.25
BR099E	1.07	BR120H	0.81
BR099F	0.99	BR120I	1.08
BR099G	1.10	BR130A	1.07
BR099H	1.02	BR130B	1.02
BR099I	0.93	BR130C	0.93
BR119A	1.00	BR130D	0.98
BR119B	0.96	BR130E	0.93
BR120A	0.81	BR130F	0.85
BR120B	0.81	BR130G	0.77
BR120C	0.98	BR130H	0.94
BR120D	0.96	BR130I	0.94

B | Images, alignment, and model fitting results of NGC 1052 from the VLBA multi- λ and RadioAstron data sets

This appendix contains additional figures and tables corresponding to chapter 4.

B.1. VLBA multi-frequency observation of NGC1052

In the following additional figures from the alignment of the multi-frequency VLBA observations presented in Sect. 4.2.1 are presented, as well as additional plots for the Gaussian model fit components.

Table B.1.: Parameters of Gaussian model fitting components for all frequencies of the multi-frequency observation of NGC 1052 from April 2017.

ID	Flux density [Jy]	RA [mas]	DEC [mas]	Radius [mas]	Angle [°]	Major ¹ [mas]	Ratio ²	PA ³ [°]	log T_b [K]
L - Band									
EJ	0.011	57.21	20.06	60.62	70.67	15.92	1.00	–	7.37
A1	0.008	33.28	15.20	36.59	65.46	6.17	1.00	–	8.04
A2	0.034	26.78	12.57	29.59	64.85	5.18	1.00	–	8.84
A3	0.023	22.50	10.16	24.68	65.70	2.36	1.00	–	9.35
A4	0.038	18.90	9.57	21.19	63.15	1.60	1.00	–	9.91
A5	0.037	15.51	6.90	16.97	66.03	2.19	1.00	–	9.63
A6	0.041	10.76	4.78	11.77	66.06	3.48	1.00	–	9.26
A7	0.324	5.30	2.54	5.87	64.39	1.89	1.00	–	10.70
A9/10	0.054	1.90	0.93	2.12	63.87	2.38	1.00	–	9.72
D2	0.013	–19.91	–9.14	21.90	–114.65	8.62	1.00	–	7.99
D1	0.028	–25.63	–10.83	27.82	–112.92	4.44	1.00	–	8.90
C - Band									
A2	0.008	26.57	12.87	29.52	64.16	5.39	1.00	–	7.13
A3	0.002	22.67	11.21	25.29	63.70	0.00	–	–	–
A4	0.008	19.66	9.85	21.99	63.39	2.87	1.00	–	7.66
A5	0.008	16.00	7.24	17.56	65.65	2.61	1.00	–	7.78
A6	0.008	11.49	4.47	12.33	68.73	3.98	1.00	–	7.40
A7	0.166	5.77	2.82	6.42	63.97	1.42	1.00	–	9.61
A8	0.016	4.18	2.90	5.09	55.24	0.29	1.00	–	9.98

Table B.1.: Continuation from previous side

ID	Flux density [Jy]	RA [mas]	DEC [mas]	Radius [mas]	Angle [°]	Major [mas]	Ratio	PA [°]	log T_b [K]
A9	0.176	2.71	1.37	3.04	63.15	0.67	1.00	–	10.28
A10	0.304	1.90	1.12	2.20	59.35	0.78	1.00	–	10.39
A11/12	0.256	0.94	0.61	1.12	57.05	0.52	1.00	–	10.66
A13/14	0.033	0.09	0.30	0.31	16.35	0.00	–	–	–
C2	0.030	–4.97	–2.30	5.48	–114.87	1.12	1.00	–	9.07
C1	0.019	–6.02	–2.60	6.56	–113.32	1.31	1.00	–	8.74
WJ-D	0.001	–15.30	–6.70	16.70	–113.65	0.00	–	–	–
D2	0.002	–21.28	–9.70	23.39	–114.51	4.98	1.00	–	6.63
D1	0.005	–25.65	–10.46	27.70	–112.18	5.31	0.41	–29.97	7.35
X - Band									
A4	0.007	19.08	9.32	21.23	63.96	5.29	1.00	–	6.65
A5	0.005	14.72	6.02	15.90	67.77	3.92	1.00	–	6.77
A7	0.105	5.84	2.57	6.38	66.25	1.38	1.00	–	8.98
A8	0.018	4.00	2.04	4.48	62.99	1.35	1.00	–	8.23
A9	0.167	2.69	1.12	2.91	67.43	0.50	1.00	–	10.06
A10	0.218	2.02	0.86	2.19	66.99	0.57	1.00	–	10.07
A11/12	0.225	1.16	0.50	1.27	66.85	0.36	1.00	–	10.47
A13	0.285	0.45	0.11	0.46	76.39	0.47	1.00	–	10.34
B2	0.032	–2.10	–0.85	2.26	–111.96	0.40	1.00	–	9.54
B1	0.014	–3.21	–1.60	3.58	–116.50	0.96	1.00	–	8.42
C2	0.019	–4.41	–2.49	5.06	–119.50	0.36	1.00	–	9.42
C1	0.032	–5.48	–2.76	6.13	–116.70	1.25	1.00	–	8.55
WJ-C	0.002	–7.42	–3.82	8.35	–117.23	0.34	1.00	–	8.58
D1	0.003	–24.92	–12.20	27.75	–116.09	2.84	1.00	–	6.86
U - Band									
A7	0.037	5.88	2.59	6.43	66.26	1.40	1.00	–	8.00
A8	0.005	4.39	2.59	5.10	59.42	0.67	1.00	–	7.79
A9	0.071	2.74	1.19	2.99	66.49	0.63	1.00	–	8.97
A10	0.079	2.16	0.89	2.33	67.55	0.60	1.00	–	9.06
A11	0.063	1.35	0.64	1.50	64.58	0.33	1.00	–	9.49
A12	0.060	1.07	0.40	1.14	69.32	0.24	1.00	–	9.73
A13	0.275	0.41	0.17	0.45	67.01	0.36	1.00	–	10.05
A14	0.073	–0.04	–0.06	0.08	–145.18	0.24	1.00	–	9.83
B3	0.028	–1.63	–0.50	1.70	–106.90	0.22	1.00	–	9.47
B2	0.102	–1.97	–0.84	2.14	–113.01	0.35	1.00	–	9.64
B1	0.019	–3.22	–1.66	3.62	–117.36	0.85	1.00	–	8.15
C2	0.012	–4.10	–2.31	4.70	–119.41	0.71	1.00	–	8.08
C1	0.014	–5.33	–2.72	5.99	–117.06	1.44	1.00	–	7.54
K - Band									
A7	0.022	5.89	2.63	6.45	65.98	1.42	1.00	–	7.43
A8	0.003	4.31	2.13	4.81	63.68	0.34	1.00	–	7.81
A9	0.028	2.88	1.34	3.18	65.06	0.50	1.00	–	8.45

Table B.1.: Continuation from previous side

ID	Flux density [Jy]	RA [mas]	DEC [mas]	Radius [mas]	Angle [$^{\circ}$]	Major [mas]	Ratio	PA [$^{\circ}$]	log T_b [K]
A10	0.065	2.27	0.96	2.46	66.95	0.69	1.00	–	8.54
A11	0.057	1.32	0.52	1.42	68.57	0.33	1.00	–	9.13
A12	0.022	0.99	0.42	1.08	66.93	0.18	1.00	–	9.25
A13	0.237	0.44	0.21	0.49	64.21	0.33	1.00	–	9.72
A14	0.170	0.03	0.00	0.03	92.06	0.18	1.00	–	10.13
A15	0.023	–0.23	–0.10	0.25	–112.73	0.00	–	–	–
B3	0.065	–1.51	–0.48	1.59	–107.47	0.38	1.00	–	9.04
B2	0.095	–1.88	–0.83	2.06	–113.72	0.35	1.00	–	9.28
B1	0.020	–3.28	–1.63	3.66	–116.51	0.46	1.00	–	8.37
C2	0.010	–4.05	–2.27	4.64	–119.28	0.68	1.00	–	7.74
C1	0.006	–5.86	–2.66	6.43	–114.41	0.79	1.00	–	7.41
Q - Band									
A7	0.002	6.13	2.53	6.63	67.57	0.66	1.00	–	6.51
A9	0.018	2.71	1.18	2.95	66.53	0.62	1.00	–	7.48
A10	0.018	1.91	0.90	2.11	64.75	0.53	1.00	–	7.62
A11	0.016	1.27	0.63	1.42	63.46	0.25	1.00	–	8.23
A12	0.024	0.84	0.26	0.88	72.84	0.44	1.00	–	7.93
EJ	0.024	0.54	0.15	0.56	74.05	0.08	1.00	–	9.43
A13	0.086	0.32	0.22	0.39	55.73	0.19	1.00	–	9.19
A14	0.161	0.00	0.03	0.03	–5.74	0.12	1.00	–	9.88
A15	0.064	–0.18	–0.08	0.20	–115.19	0.13	1.00	–	9.39
EJ	0.048	–0.40	–0.15	0.43	–110.21	0.11	1.00	–	9.40
WJ-B	0.019	–0.91	–0.24	0.94	–104.86	0.34	1.00	–	8.03
WJ-B	0.039	–1.26	–0.49	1.35	–111.14	0.16	1.00	–	8.98
B3	0.037	–1.51	–0.49	1.58	–107.83	0.24	1.00	–	8.62
B2	0.050	–1.86	–0.77	2.01	–112.53	0.36	1.00	–	8.42
B1	0.009	–3.09	–1.69	3.53	–118.68	0.41	1.00	–	7.56
C2	0.005	–3.92	–2.16	4.47	–118.88	0.26	1.00	–	7.70

¹ FWHM major axis of restoring beam ² Ratio of minor to major axis ³ PA of major axis of restoring beam

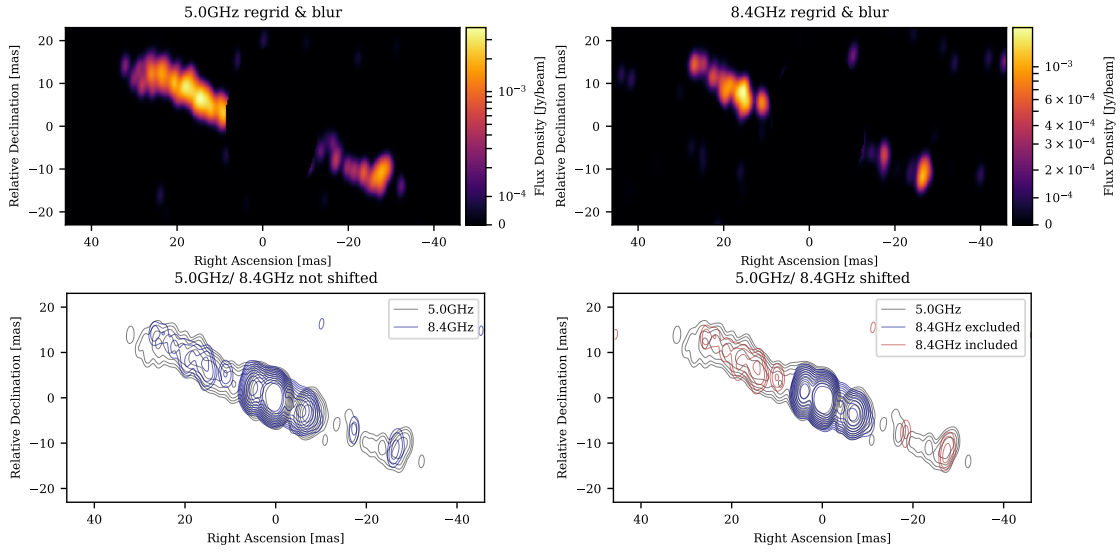


Figure B.1.: Alignment of NGC 1052 images. (*Top*) images of the CLEAN model convolved with the CLEAN beam for 5.0 GHz (*left*) and 8.4 GHz (*right*). An elliptical mask with position angle equal to that of the beam was applied to both images before cross-correlation. The mask was shifted slightly towards the western jet to exclude regions affected by free-free absorption. (*Bottom*) Contour maps without shift (*left*) and with shift applied (*right*). The red contours illustrate the region of the 8.4 GHz image used for the cross-correlation.

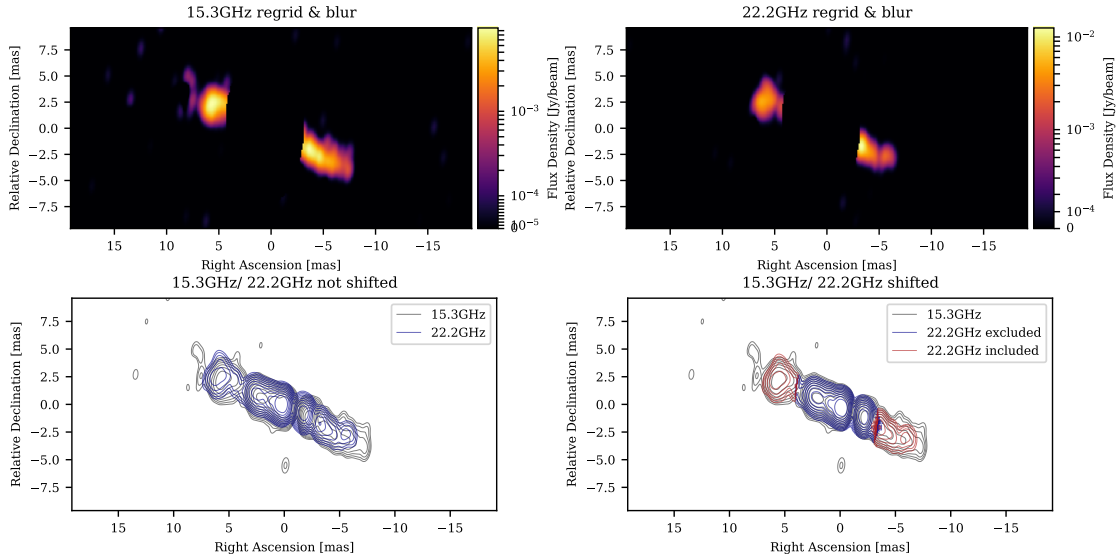


Figure B.2.: Alignment of NGC 1052 images. (*Top*) images of the CLEAN model convolved with the CLEAN beam for 15 GHz (*left*) and 22 GHz (*right*). An elliptical mask with position angle equal to that of the beam was applied to both images before cross-correlation. The mask was shifted slightly towards the western jet to exclude regions affected by free-free absorption. (*Bottom*) Contour maps without shift (*left*) and with shift applied (*right*). The red contours illustrate the region of the 22 GHz image used for the cross-correlation.

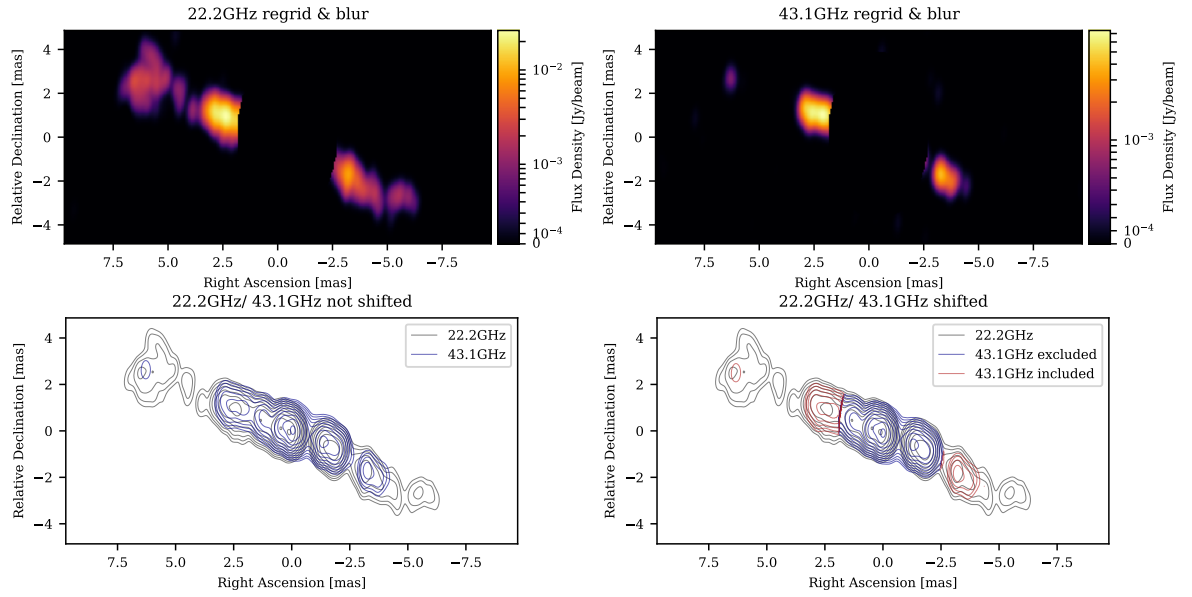


Figure B.3.: Alignment of NGC 1052 images. (*Top*) images of the CLEAN model convolved with the CLEAN beam for 22 GHz (*left*) and 43 GHz (*right*). An elliptical mask with position angle equal to that of the beam was applied to both images before cross-correlation. The mask was shifted slightly towards the western jet to exclude regions affected by free-free absorption. (*Bottom*) Contour maps without shift (*left*) and with shift applied (*right*). The red contours illustrate the region of the 43 GHz image used for the cross-correlation.

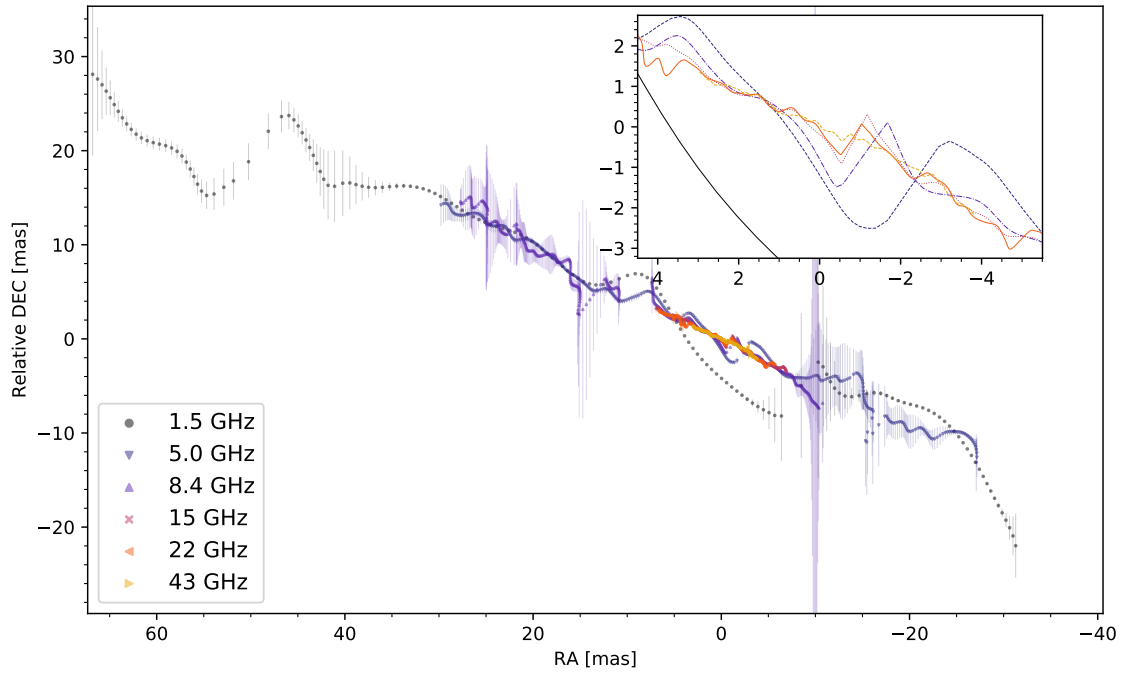


Figure B.4.: All ridge-lines of the images of NGC 1052 observed in April 2017 with the VLBA plotted on top of each other shifted according to the alignment in Sect. 4.2.1. The upper in-line panel shows a zoom into the inner region of the main plot. The error-bars are derived from the Gaussian fit to the data.

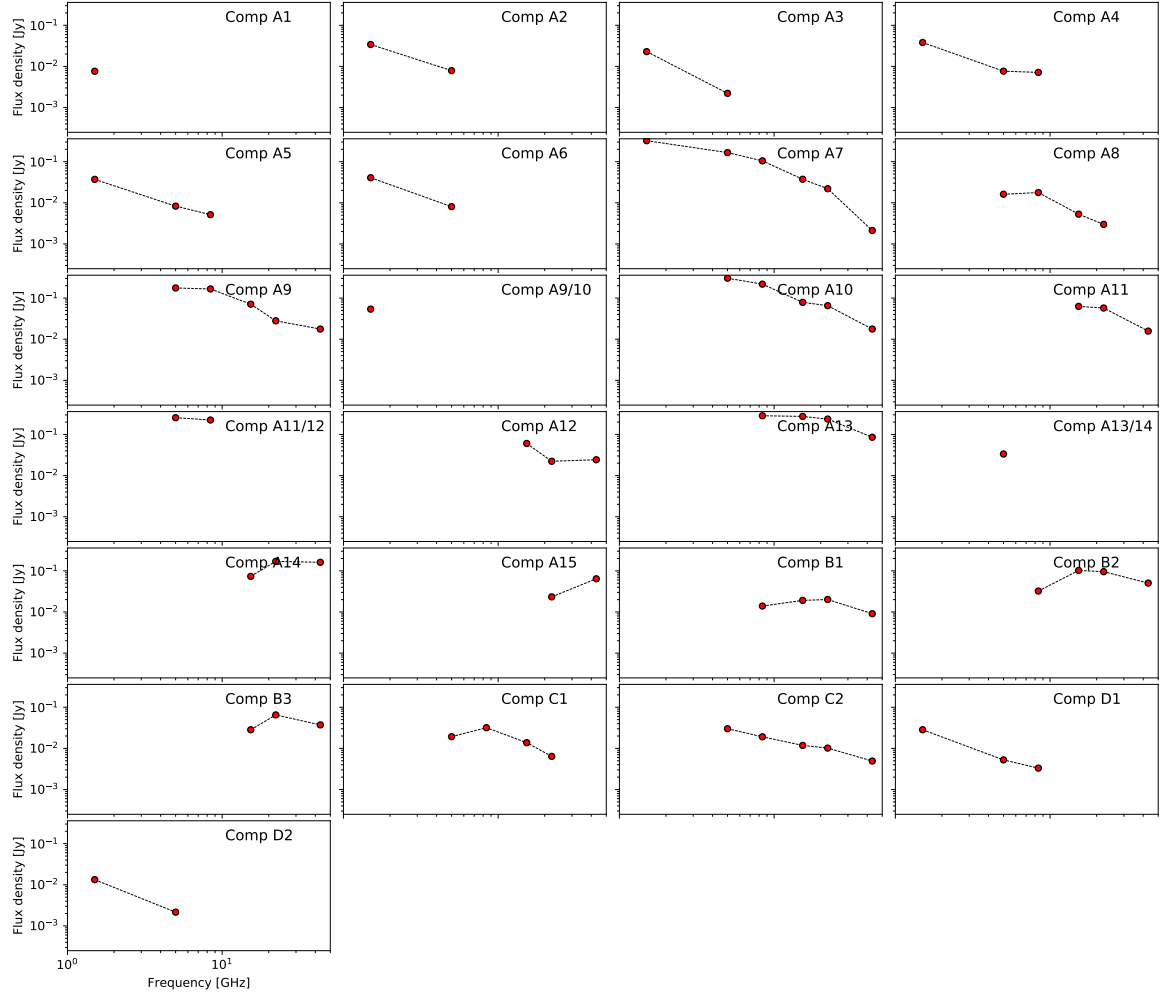


Figure B.5.: Radio spectra for all Gaussian model fit components to the NGC 1052 data observed in epoch April 2017. Images with Gaussian model components plotted on top are shown in Fig. 4.2.

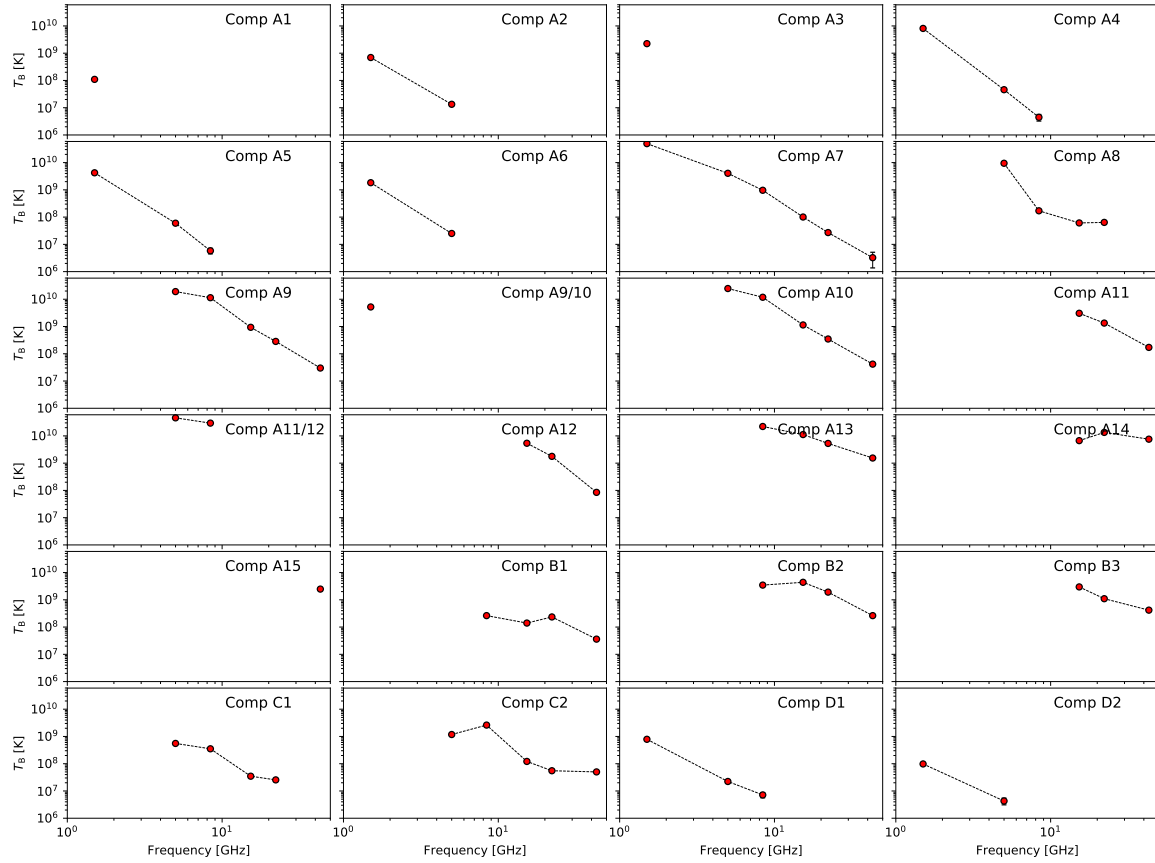


Figure B.6.: Brightness temperature with respect to frequency for all Gaussian model fit components to the NGC 1052 data observed in epoch April 2017. Images with Gaussian model components plotted on top are shown in Fig. 4.2.

B.2. RadioAstron observation of NGC1052

Below a fringe plot obtained during the RadioAstron correlation is shown.

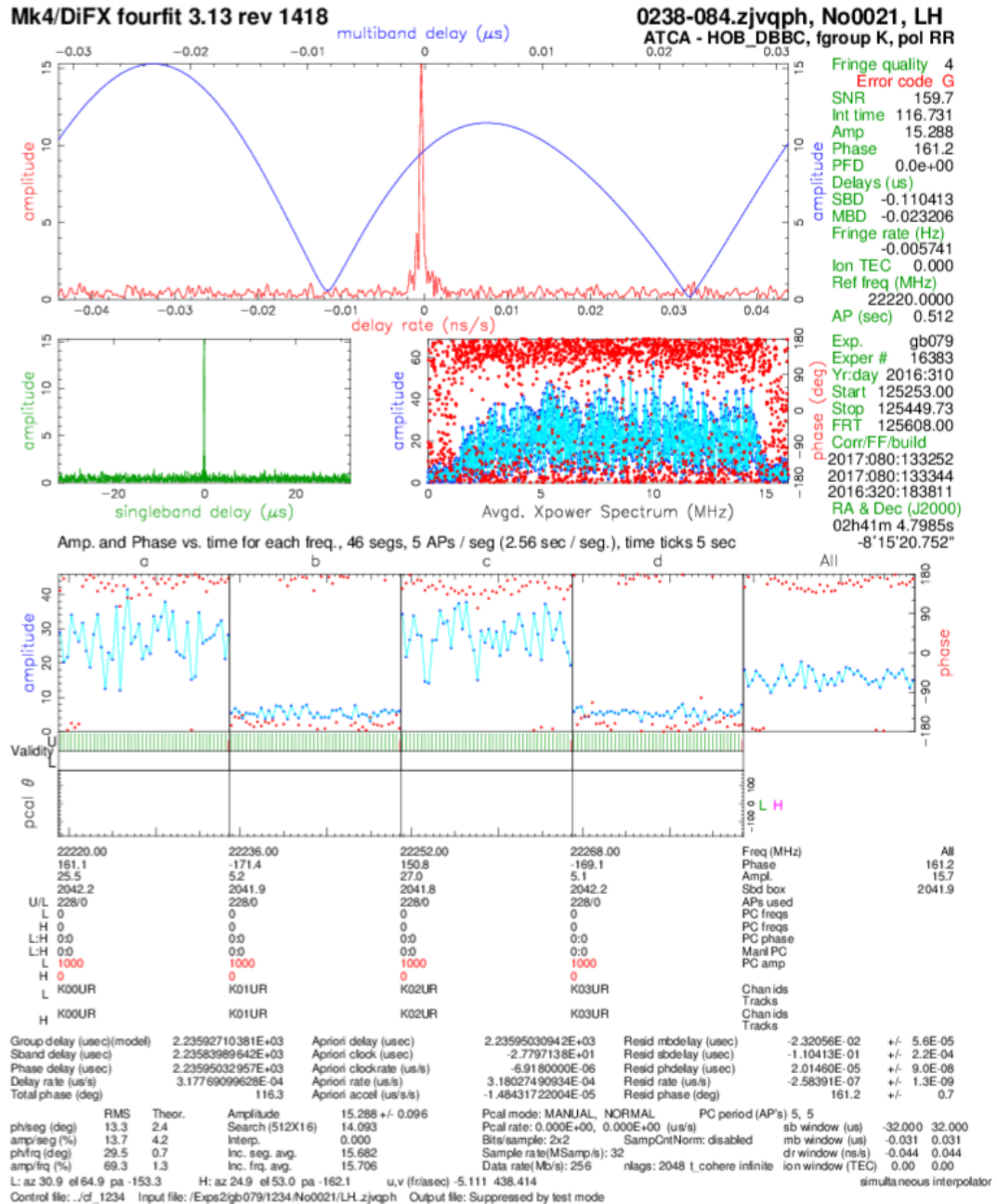


Figure B.7.: Fringe plot for baseline ATCA-Hobart and polarization RR for the RadioAstron observations on November 5, 2016 at 22 GHz (code GB079).

C | Development of Python scripts for calibration and analysis

Within the scope of this work I developed a set of Python scripts to ease the calibration and data analysis. Here I shortly introduce the different sets of scripts, as follows: Appendix C.1 presents my setup to use the PARSELTONGUE python interface to AIPS and in appendix C.2 several routines developed for data analysis as, for example, 2D cross-correlation of VLBI images, are presented.

C.1. Calibration using AIPS and PARSELTONGUE

Calibrating VLBI data requires standard procedures to be used depending for example on the observing frequency or noise level of the data. Many of the single steps are very similar for different observations. In case of VLBA observations this fact resulted in the development of dedicated procedures to be run in AIPS, the VLBAUTILS. The included run files set most of the parameters typically needed for VLBA calibration of the interferometric visibilities in phase and amplitude as a function of time and a function of frequency. It leaves the user with a small amount of additional parameters that have to be specified.

I followed a similar approach for the observations presented in this work, making use of the PARSELTONGUE python interface to AIPS (Kettenis et al. 2006)¹. I developed a set of scripts to ease calibration of VLBI data (all scripts can be found at <https://github.com/abaczko/VLBIcalib>).

There are several advantages of scripting. For example I easily could test several approaches for the multi-frequency VLBA observation of NGC 1052 presented in chapter 4. Including different settings of AIPS tasks, various versions of bandpass calibration (amplitude and phase corrections as a function of frequency), or smoothing of solution tables with only small changes to the corresponding python script.

Before going into detail, I will give a short overview on the structure of AIPS. It is still the standard software for calibrating VLBI observations, as it includes all routines (called *tasks*) to perform dedicated VLBI analysis. Each task has a set of parameters (called *adverbs*), which needs to be adjusted for the specific observation. For example the calibration source and scan that should be used during fringe fitting. After all *adverbs* are set appropriate, the *task* is run and the routine starts. PARSELTONGUE is an interface allowing to control all aspects of AIPS with python. There is the possibility to work only on the command line or to set up scripts to

¹More information on PARSELTONGUE can be found at <http://old.jive.nl/jivewiki/doku.php?id=parsel tongue:parsel tongue>

be run. PARSELTONGUE itself already comes with a lot of functionality. The module is build up of several classes, for example *AIPSTask*, which implements running AIPS tasks or *AIPS* which among other things provides the *AIPSDisc* class². If there is a local installation of AIPS the PARSELTONGUE module can use this one as well as the directories loaded by AIPS. In addition, there is the possibility to make use of *AIPSLite*, which comes with PARSELTONGUE. In this case each task evoked will be downloaded from the Internet and saved locally in the

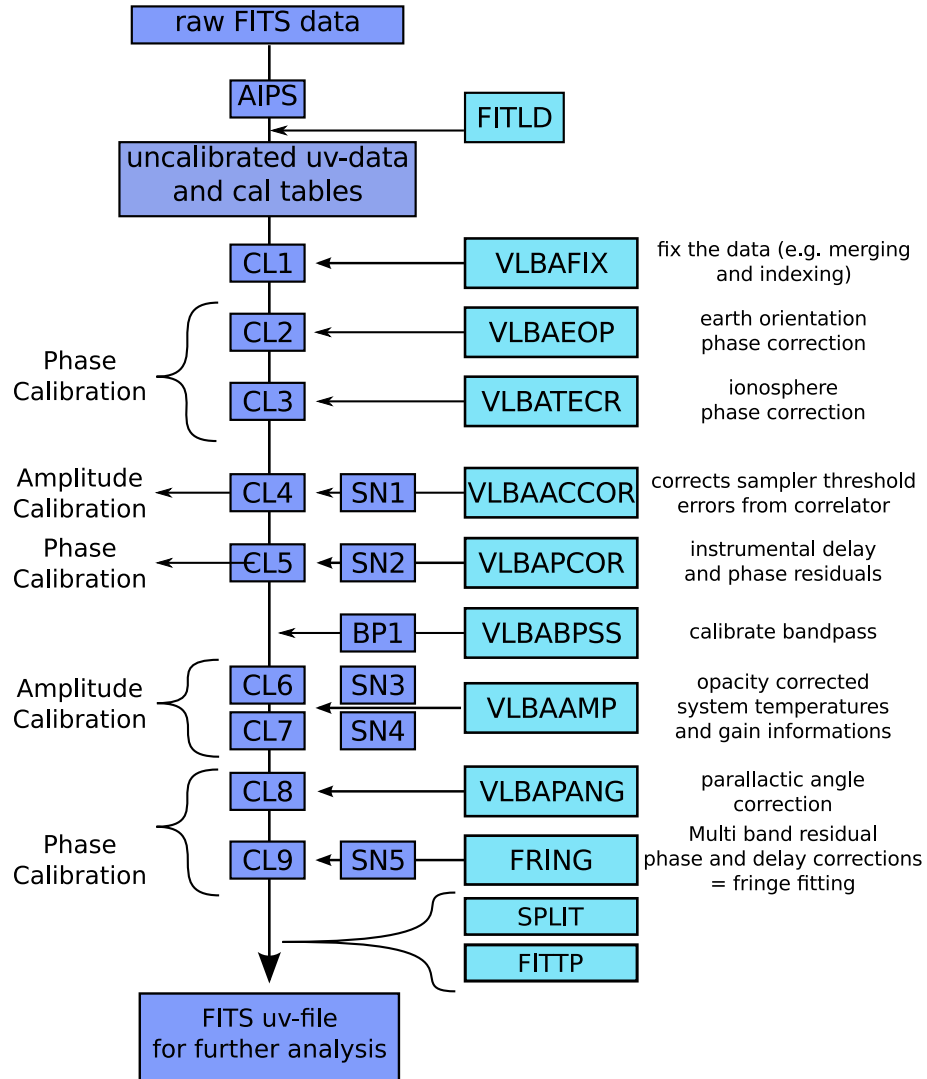


Figure C.1.: Block diagram of the typical calibration routine in AIPS for a VLBA observation.

working directory. All tasks are available through the module, but the parameters have to be set manually and the task have to be run in the same manner as is done in AIPS. However, all commands to set adverbs and to run the tasks can be put into a script and run directly. In

²A full description of the classes implemented in PARSELTONGUE can be found at <http://www.jive.nl/parseltongue/doc/index.html>

this setup AIPS is controlled by Python via PARSELTONGUE which allows easy access to calibration tables and visibility data. In addition, all available python modules can be used during calibration. For example this allows easy manipulation and plotting of the visibility data or calibration results themselves.

For calibrating VLBI data one typically has to follow several steps of calibration, that are more or less the same for all experiments with slight deviations depending on the observation. A block diagram showing the typical procedures that have to be run in AIPS for a VLBA observation is shown in Fig. C.1. A extensive description of the individual procedures can be found at <http://www.aips.nrao.edu/cook.html>. This makes VLBI calibration an ideal problem to automate as far as possible.

C.1.1. ParseLTongue setup

Fig. C.2 gives a short overview on the calibration module, consisting of several individual scripts, which are shortly described in the following. All scripts can also be found on my private github repository (<https://github.com/abaczko/VLBIcalib>).

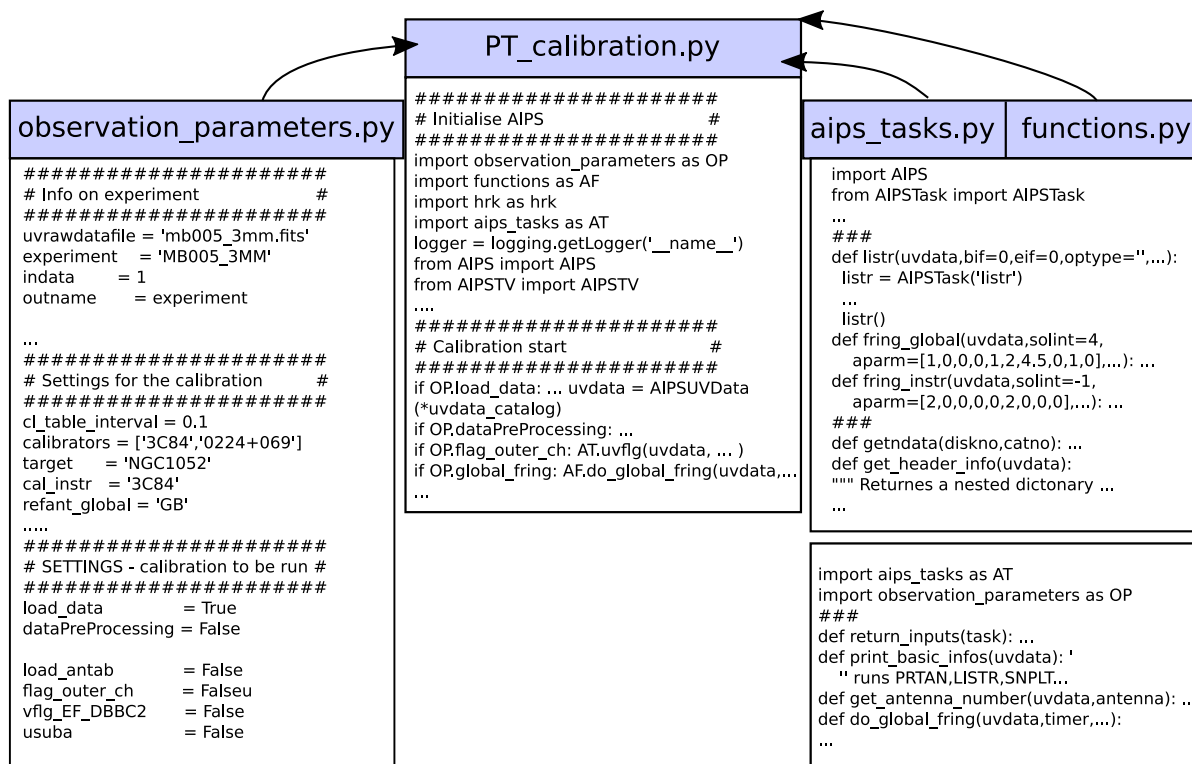


Figure C.2.: An overview of my Python modules for calibration using PARSELTONGUE.

aips_tasks.py: In order to run tasks in a *pythonic* way, the most common used tasks are wrapped into a python function, allowing to call them as:

```
1 AT.snplt(uvdata, ine='TY', inv=1, optype='TSYS', stokes='', sources=[], opcode='
    ALIF')
```

This example plots the TY 1 table to an output file using the task SNSMO. The function located in *aips_tasks.py* looks as:

```
1 def snplt(uvdata, ine='CL', antennas=[], nplots=16, inv=0, optype='PHAS',
2     stokes='', sources=[], opcode='ALIF', plotname=False):
3     outn = uvdata.name
4     if plotname != False:
5         outfile=outn+'_'+plotname+'_snplt_'+ine+str(inv)+'.ps'
6     else:
7         outfile=outn+'_snplt_'+ine+str(inv)+'.ps'
8     snplt = AIPSTask('snplt')
9     snplt.indata = uvdata
10    snplt.intable = uvdata.table(ine, inv)
11    snplt.optype = optype
12    snplt.antennas[1:] = antennas
13    snplt.stokes = stokes
14    snplt.sources = sources
15    snplt.dotv = -1
16    snplt.do3col = 2
17    snplt.opcode = opcode
18    snplt.nplots = nplots
19    HF.print_inp_to_log(snplt, 'SNPLT')
20    snplt()
21    lwpla(uvdata, outfile)
```

All functions inside *aips_tasks.py* have already a few standard inputs, which are commonly used. In the example above this is, e.g., opcode='ALIF' to plot all IFs combined per default. In addition, the function directly calls the LWPLA task to save the plot to a file, which gets a standard name if not set by plotname. Another line inside the code should not get unnoticed: HF.print_inp_to_log(snplt, 'SNPLT'). It calls another function inside the *helper_functions.py* sub-module, which prints all keywords used for the function snplt to a text file. The setup of all scripts keeps track of everything that was done. The outputs, which are typically printed on the AIPS message window are saved to file. In addition a logging file is set up, in which all input parameters for functions are saved by using HF.print_inp_to_log(function, functionname to be written as header line). The python module logging is used to write some additional information to this log file. An example output from the above code would be:

```
1 Inputs for SNPLT:
2
3 'inname': BB377_L
4 'inclass': UVDATA
5 'inseq': 1.0
6 'indisk': 2.0
7 'inext': SN
8 'invers': 5.0
9 'sources': ['', '', '', '', '', '', '', '', '', '', '', '', '', '', '', '', '', '', '']
10 'qual': -1.0
```

```

11 'timerang': [0.0, 0.0, 0.0, 0.0, 0.0, 0.0, 0.0, 0.0]
12 'stokes': HALF
13         :
14 File /aux/vlb119b/baczko/calibration/vlba_4_17/ParselTongue/aips_out/
    BB377_L_apcal_snplt_SN5.ps will be created.

```

functions.py, helper_functions.py: These are two additional modules containing functions that do not have to have access to the PARSELTONGUE libraries. Several functions inside are automatically called when the main calibration script runs. By using the *task* functions defined in *aips_tasks.py*, more specific problems are addressed during calibration. For example running the task APCAL by using a function called *do_apcal* will run APCAL two times, while using the fitting values for opacity and receiver temperature for the second run. In this way the fitting results can be improved. In addition, these modules add functionality to easily access properties of the interferometric data. For example returning the antenna number for a given antenna name (as named in the antenna table) or returning an *astropy Table* object containing all scans. Here is an example code to retrieve the scans and to convert a scan into its starting and end time. This functionality enables the user of my modules to enter either a time range to task functions as *fring* or a scan number (as it is possible inside AIPS):

```

1  def get_scans(uvdata):
2      '''
3      Get back an astropy Table of all scans
4      '''
5      if not os.path.isfile(aips_out+uvdata.name+'_listr_SCAN.txt'):
6          AT.listr(uvdata)
7      else:
8          pass
9      lines=[]
10     with open(aips_out+uvdata.name+'_listr_SCAN.txt','r') as f:
11         for row in islice(f,0,5,1):
12             pass
13             header=next(f)
14             for row in f:
15                 if row.startswith('\x0c'):
16                     break
17                 lines.append(row)
18
19     header1=header.split()
20     header1[-1]=' '.join([header1[-2],header1[-1]])
21     header1.pop(-2)
22     header1[-2]=' '.join([header1[-3],header1[-2]])
23     header1.pop(-3)
24     ind=[0,5,21,29,37,41,66,73,81,-1]
25     l1=[]
26     for l in lines:
27         l1.append([l[ind[i]:ind[i+1]].strip() for i in range(len(ind)-1)])
28     scans=Table(rows=l1,names=header1,masked=True)
29     scans['Time_start']=[tt.split('-')[0].strip() for tt in scans['Timerange']]

```

```

30 scans['Time_end']=[tt.split('-')[1].strip() for tt in scans['Timerange'
31 ]]
32 del scans['Timerange']
33 return scans
34
35 def scantime(uvdata,scan):
36     '''
37     returns the timer of the specified scan as used for e.g. fring.timer
38     '''
39     scans=get_scans(uvdata)
40     time1,time2=[0],[0]
41     time1.extend([int(x) for x in scans[scan-1]['Time_start'].split('/')[1].
42                  split(':')])
43     time2.extend([int(x) for x in scans[scan-1]['Time_end'].split('/')[1].
44                  split(':')])
45     time1.extend(time2)
46     return time1

```

observation_parameters.py: This script is the only file, which had to be adjusted for each observation. It sets all variables needed to run the calibration, e.g., the location of *antab* files or other calibration files. If AIPSLite should be used or not. In case the local AIPS installation is used, it is important to be careful by setting the parameters *outname*, *outclass*, *outdisk* and *outseq*. Accordingly the dedicated AIPS catalog will be used on the disk that is specified. In addition, the file contains information about the calibration settings, e.g. inputs for global fringe fitting, as calibration source and solution interval. The last important set of parameters control which calibration steps should be made. In the following I show a few examples:

```

1 load_data          = False # loading the data from the correlator
2 swpol              = False # applying swpol
3 tabed              = False # using tabed, e.g. to correct mounting for PV
4 flag_outer_ch      = False # flag the first and last 3 channel
5 correct_eop        = False # correct for EOP. The file will automatically
6                     be downloaded.
7 runaccor           = False # to run ACCOR
8 clear_manual_phasecal= False # deletes all tables produced after ACCOR to
9                     start delay calibration over again. The history file will be searched
10                    to find the last SN and CL tables as were produced by ACCOR and deletes
11                    all SN and CL tables higher than these found
12 global_fring       = False # do global fring
13 runapcal           = False # run APCA
14 opacity            = False # fit for opacity

```

Setting the individual variables to *True* will tell python to run this calibration step.

PT_calibration.py: This is the main script for running a calibration. It loads all python modules needed for the calibration as well as the *observation_parameters.py* script to set all variables accordingly. In addition, it sets up the whole environment by importing several PARSELTONGUE modules as well as importing AIPSLITE if required. If not already existing, the logging file will be created and a header will be written to it. Afterwards all variables given

in `observation_parameters.py` are checked if *True* or *False* and the respective code is run or not. Here are a few example parts from the script:

```

1  # Import python AIPS libraries
2  #
3  if OP.AIPSLite:
4      logger.info('Will use AIPSLite')
5      import AIPSLite
6      AIPSLite.setup()
7  else:
8      logger.info('Will use local AIPS installation')
9  #
10 from AIPS import AIPS#, AIPSDisk # I am not sure if I need AIPSDisk
11 from AIPSTask import AIPSTask, AIPSList
12 from AIPSData import AIPSUVDData, AIPSImage, AIPSCat
13 from Wizardry.AIPSData import AIPSUVDData as WizAIPSUVDData
14 from AIPSTV import AIPSTV
15                                     :
16 if OP.load_data:
17     if len(OP.uvrawdatafile)>1:
18         for files in OP.uvrawdatafile:
19             uvdata_catalog = hrk.loaddata(files, OP.outname, OP.outclass, OP.outdisk
20             , OP.outseq, clint=OP.cl_table_interval, digicor=OP.digicor, doconcat=1)
21     else:
22         uvdata_catalog = hrk.loaddata(OP.uvrawdatafile[0], OP.outname, OP.
23         outclass, OP.outdisk, OP.outseq, clint=OP.cl_table_interval, digicor=OP.
24         digicor)
25     uvdata = AIPSUVDData(*uvdata_catalog)
26     AF.data_exists(uvdata)
27 elif not OP.load_data and OP.dataPreProcessing:
28     logger.info('Use existing data\n')
29     uvdata_catalog = [OP.outname, OP.outclass, OP.outdisk, OP.outseq]
30     print uvdata_catalog
31     uvdata = AIPSUVDData(*uvdata_catalog)
32     AF.data_exists(uvdata)
33     uvdata.clrstat()
34                                     :
35 if OP.runacscl:
36     AT.acscl(uvdata, doband=1, bpv=1)
37     cl_hv = uvdata.table_highver('CL')
38     sn_hv = uvdata.table_highver('SN')
39     AT.snsmo(uvdata, samptype='MWF', smotype='AMPL', doblank=-1, dobtween=1, inv=
40     sn_hv, outv=sn_hv+1, refant=OP.refant)
41     AT.clcal(uvdata, ine='SN', gainv=cl_hv, gainu=cl_hv+1, snv=sn_hv+1, refant=OP
42     .refant, doblank=1, interpol='self')
43     AT.snplt(uvdata, ine='SN', inv=sn_hv+1, optype='AMP', stokes='', sources=[],
44     opcode='ALST', plotname='acscl')

```

The development of these modules enabled me to easily try out different calibration approaches for VLBI data. Especially for noisy and challenging data this turned out to save time on the long hand. Once the parameters in `observation_parameters.py` are set correctly, the calibration is run one step after the other without the need to interact in between. It can be

started and the final calibrated data and output files can be examined once the calibration is finished.

C.2. Data analysis Python scripting

In scope of my doctoral studies I developed a set of python scripts in order to analyse the final VLBI images. All scripts can be found at <https://github.com/abaczko/VLBIana>. In the following I shortly describe a few of the main modules.

fit_functions.py, jet_calculus.py: Two modules with a collection of functions, required by several other modules. For example, to derive the number of pixels in a beam, deriving the axis of the beam along a given angle, or fit a function to a given set of parameters using the ODR package (Boggs & Rogers 1990) in order to account for errors in two dimensions.

derive_beta_theta.py: A small python module to plot the parameter space of intrinsic velocity and the angle of the jet(s) to the line of sight (see, e.g., Fig. 3.12). It is based on equations 2.3.6 and 2.3.7. The module contains the JetCalc class, which holds several parameters and functions needed for plotting the parameter space as well as the plotting function. A child class is added to account for two jets. Here, I give a small glimpse on the basic structure of this module:

```

1 class JetCalc(object):
2     def __init__(self, theta, ba, R, block=False, jet='jet'):
3         self.block=block
4         self.jet=jet
5         self.ba=ba
6         self.R=[(x if x>=1. else 1.+1e-10) for x in R]
7         self.theta = np.deg2rad(theta)
8         self.theta_deg=theta
9         def beta_jet(self, b_app=1):
10             bapp=(self.ba if b_app==1 else b_app)
11             ''' Caculates intrinsic beta as dependent of apparent beta for jet on
12                 a range of theta_LOS'''
13             return [x/(np.sin(self.theta)+x*np.cos(self.theta)) for x in bapp]
14             :
15         def plot_theta_beta(self, savefig=True, beta_j=False, beta_R=False, plot_ip=
16             False):
17             '''
18             To plot beta-theta as dependent from beta_app and the flux density
19             Ratio R.
20             Uses self value of jet to calculate curves either for Jet or
21             counterjet
22             '''
23             :
24
25 class BothJets(JetCalc):
26     def __init__(self, theta, ba, R, ba_c, block=False, jet='jet', cjet='cjet'):
27         JetCalc.__init__(self, theta, ba, R, block)
28         self.ba_c=ba_c

```



```
24 self.cjet=cjet
```

This module can directly be called in the command line. In order to produce the plot, the apparent velocity and the flux density ratio have to be given directly to the calling function. It will be interpreted using argparse:

```
1 $ python derive_beta_theta.py --ratio xxx --beta xxx
```

This will write a plot for a given flux density ratio and velocity for one jet. A short description of its capabilities at time of submitting this thesis is given by:

```
1 $ python derive_beta_theta.py --help
2
3 usage: derive_beta_theta.py [-h] [-r RATIO RATIO] [-b BETA BETA] [--jet
4     JET]
5                               [-br BETA_R BETA_R] [-t THETA THETA]
6 If run as '__main__': Produce beta_theta plot of given beta and flux ratio
7 .
8 Function assumes theta(beta_app) for approaching jet. If formular for
9 receding
10 jet is required set --jet='cjet'. In case there are different velocities
11 for
12 approaching and receding jet it is possible to plot both graphs into one
13 figure. For this set --beta_r to beta_apparent for receding jet.
14
15 optional arguments:
16   -h, --help                show this help message and exit
17   -r RATIO RATIO, --ratio RATIO RATIO
18                               Flux density ratio, give [R, R_err]
19   -b BETA BETA, --beta BETA BETA
20                               Apparent beta of jet, give [beta,beta_err]
21   --jet JET                 Specify if jet or counterjet. Valid 'jet'/'cjet'
22   -br BETA_R BETA_R, --beta_r BETA_R BETA_R
23                               Apparent beta of an receding jet, give [beta,
24                               beta_err]
25   -t THETA THETA, --theta THETA THETA
26                               Define the theta_range to plot. Default [35,90]
```

plot_spix.py: A simple function to plot a spectral index map based on two images. It requires input images, which are already aligned, re-gridded, and convolved with the same beam.

align_images.py: This module was used to align the images in Sect. 4.2.1 pairwise. It makes use of EHTIM (Chael et al. 2016, 2018) and the scikit package (van der Walt et al. 2014).

Basically, EHTIM is used in order to re-grid the input images to the same pixel size and field of view (fov) and restore these images with the same beam according to the requirements listed in Sect. 4.2.1. The beam of the lower frequency image is used and the fov and map dimension of the higher frequency image. Afterwards the images are aligned based on a 2D cross-correlation in Fourier space implemented in the skimage module according to:

```

1                                     :
2 from skimage.feature import register_translation
3 from skimage.feature.register_translation import _upsampled_dft
4 from scipy.ndimage import fourier_shift
5
6 def apply_shift(img, shift):
7     offset_image = fourier_shift(np.fft.fftn(img), shift)
8     imgalign = np.fft.ifftn(offset_image)
9     img2 = imgalign.real
10
11     return img2
12
13 def align(img1, img2, inc1, inc2):
14
15     #align image1 with image2
16     shift, error, diffphase = register_translation((img1), (img2), 100)
17     print ('register images new shift (y,x): [{0} : {1}] mas'.format(shift[0]*
18         inc1, shift[1]*inc2))
19     print ('register images new shift (y,x): {0} px +- {1}'.format(shift, error
20         ))
21
22     #shift img2 to found position
23     img2 = apply_shift(img2, shift)
24
25     #return aligned image and the computed shift
26     return {'align':img2, 'shift':shift}

```

The images are shifted based on the outputs from `register_translation()` which is based on [Guizar-Sicairos et al. \(2008\)](#). The output of the main function inside this module are several plots showing the difference between the original image and the re-gridded and convolved map as well the result from aligning as is seen, e.g., in Fig. 4.6. To account only for optically thin jet emission, a mask can be applied to the image before cross-correlation. The masks available at the time of submitting this work are masking:

- the left or right part of an image, starting at n pixel from the center of the map
- an elliptical area with an offset of n pixels from the center, defined by minor and major axis and a position angle
- a circular area with given radius and a possible offset from the center of the image
- masking everything below a certain flux density

The main function returns the re-gridded maps and the shifting values. It can be called by (giving an array of the images and parameters defining which region to mask):

```

1 from align_images import *
2 shifting = plot_aligned_maps(maps, flux_cut=False, radius=False, npix_x=False
    , npix_y=False, e_maj=False, e_min=False, e_pa=False)

```

Figure C.3 shows an example of two images presented in chapter 4 before and after re-gridding and convolving with the same beam.

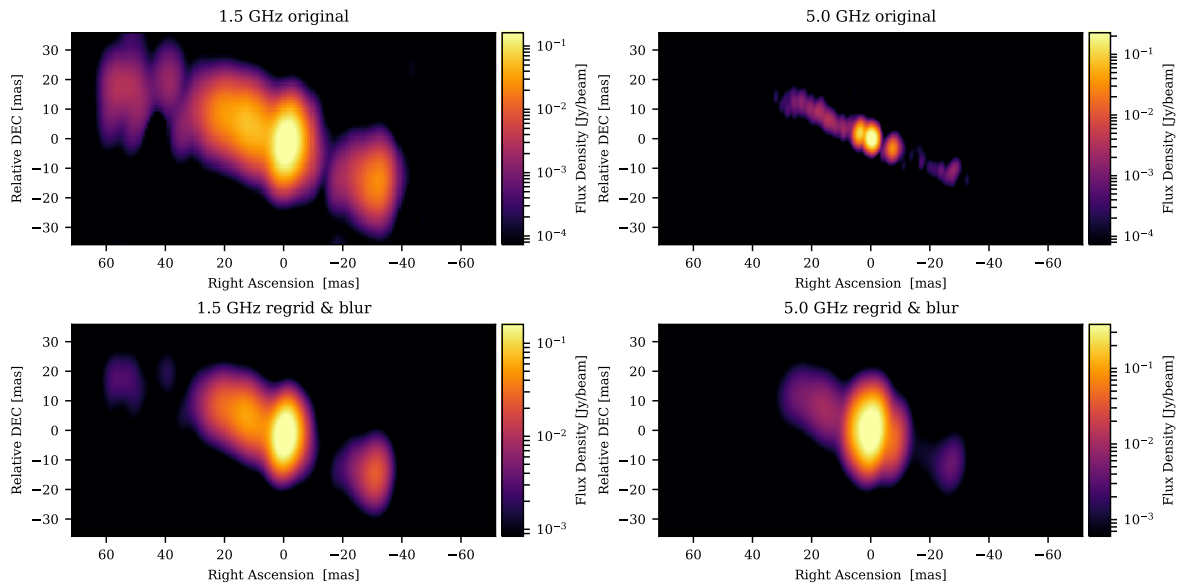


Figure C.3.: Example of the process to re-grid two given images and convolve them with the same beam. The two shown images at 1.5 GHz and 5 GHz are described in chapter 4. Before re-gridding the images did had a different fov. However, the images shown in the top panels are shrieded to the fov of the final images in the bottom panels, to better visualize the process of blurring with a larger beam.

Acknowledgements

First of all, I want to thank my supervisors Prof. Eduardo Ros and Prof. Matthias Kadler. Without their knowledge and expertise regarding AGN and radio astronomy, as well as their confidence in my skills I could not have developed my own project and career as successfully as it turned out to be. I always felt to be taken serious regarding my ideas and concerns. Eduardo's door was always open and he was happy to help and advise at any time of the day. I am really thankful for that. I am especially grateful that I was never criticised or treated differently because of my family planning.

My special thanks goes to Prof. Zensus for giving me the opportunity to conduct my doctoral studies in his group at the MPIfR. I thank Prof. Eckart for being my local supervisor at the University of Cologne. I am grateful for being part of the IMPRS which offered not only educational achievements but also social activities with other PhD students. I am thankful for the effort put into this program by Rainer and Simone.

In Prof. Manel Perucho and Dr. Christian Fromm I found great collaborators for digging more deeply into the theoretical modelling and physical understanding of the processes driving AGN jets. Their guidance and , sometimes, long discussions helped me to expand my studies towards theoretical astrophysics. I thank Garbiele Bruni for spending a lot of time explaining to me the principles of VLBI correlation and guiding me in correlating my own experiment.

Without great people around to talk to and to discuss with, it is impossible to develop an own opinion and to drive forward the own research, and not at last to enjoy being at work. I had the pleasure to have many great colleagues, which made me enjoy the time at this institute, I really want to thank all of them. Especially I like to thank our small PhD group consisting of Laura, Roberto, Jae-Young, Dhanya, Felix, and Thalia. We had a great time together, also outside of the working environment. I appreciate all the discussions with Laura and Jae-Young regarding programming, especially in python. I am thankful that I always could count on Jae-Young and Thalia when having difficulties especially in GMVA calibration. I thank Carolina for being part of my thesis committee, I always could count on her for giving good advise for several scientific problems.

I only came so far, because of all the people I had the pleasure to work with during my undergraduate studies. I really thank all members of the Dr. Karl-Remeis observatory in Bamberg, as well as the groups of Prof. Matthias Kadler and Prof. Karl Mannheim at the University of Würzburg. Without the support I got by Prof. Jörn Wilms and Prof. Matthias Kadler during my undergraduate studies I probably would not have developed in the field of astronomy as it is the case. My special thanks go to Dr. Robert Schulz, Dr. Cornelia Müller, Dr. Moritz Böck, and Dr. Christoph Grossberger who were great companions during my first steps in the field of AGN and astronomy.

Finally I want to thank my family. My father always supported me in whatever I was

enthusiastic about, thanks to him I never doubted that I am going in the right direction. Hannes, I cannot be more thankful to have found someone like you. You are the inspiration of my life and I would never have achieved all this without your unconditional love and support during all the difficult phases of my life. I am extremely happy to have Carlotta in my life and soon another little family member.

Lastly, I like to acknowledge all the tools and services used throughout this work. The SAO/NASA Astrophysical Data System³ were frequently used. This research has made use of the NASA/IPAC Extragalactic Database (NED) which is operated by the Jet Propulsion Laboratory, California Institute of Technology, under contract with the National Aeronautics and Space Administration. This research has made use of data obtained with the Global Millimeter VLBI Array (GMVA), the VLBA Network, which is a facility of the National Science Foundation operated by the Associated Universities, Inc., and RadioAstron. This research has made use of data from the MOJAVE team (Lister et al. 2009), of Astropy, a community-developed core Python package for Astronomy (Astropy Collaboration et al. 2013, 2018), the scikit-image bibliography (van der Walt et al. 2014), and scipy (Virtanen et al. 2019).

³<https://ui.adsabs.harvard.edu>

Astronomy and Astrophysics

Editor in Chief: T. Forveille

T. Forveille

Astronomy & Astrophysics
Observatoire de Paris
61, avenue de l'Observatoire
75014 Paris, France

Tel.: 33 0(1) 43 29 05 41
Fax: 33 0(1) 43 29 05 57
e-mail: aanda.paris@obspm.fr
Web: <http://www.aanda.org>

merging
Annales d'Astrophysique
Arkiv for Astronomi
Bulletin of the Astronomical Institutes
of the Netherlands
Bulletin Astronomique
Journal des Observateurs
Zeitschrift für Astrophysik
Bulletin of the Astronomical Institutes
of Czechoslovakia

Paris, October 8, 2019

Reprint Permission

Material:

Article by Baczko et al., A&A 623, A27 (2019)

Article by Baczko et al., A&A 593, A47 (2016)

To be used in:

PhD thesis entitled "Multi-Frequency VLBI Observations of the Active Galaxy NGC 1052"

University: Universität zu Köln (University of Cologne)

Permission granted to:

Anne-Kathrin Baczko
baczko@mpifr-bonn.mpg.de

I hold copyright on the material referred to above, and hereby grant permission for its use as requested herewith.

The article should be reproduced as a whole in a coherent fashion fully consistent with the version published in A&A.

Credit should be given as follows:

Credit: Author, A&A, vol, page, year, reproduced with permission © ESO.



Thierry Forveille
A&A Editor-in-Chief

Sponsored by Argentina, Armenia, Austria, Belgium, Bulgaria, Chile, Croatia, Czech Republic, Denmark, Estonia, Finland, France, Germany, Greece, Hungary, Italy, Lithuania, Netherlands, Norway, Poland, Portugal, Slovak Republic, Spain, Sweden, and Switzerland.

Produced and distributed by EDP Sciences for ESO.

Erklärung

Ich versichere, dass ich die von mir vorgelegte Dissertation selbständig angefertigt, die benutzten Quellen und Hilfsmittel vollständig angegeben und die Stellen der Arbeit – einschließlich Tabellen, Karten und Abbildungen –, die anderen Werken im Wortlaut oder dem Sinn nach entnommen sind, in jedem Einzelfall als Entlehnung kenntlich gemacht habe; dass diese Dissertation noch keiner anderen Fakultät oder Universität zur Prüfung vorgelegen hat; dass sie – abgesehen von unten angegebenen Teilpublikationen – noch nicht veröffentlicht worden ist, sowie, dass ich eine solche Veröffentlichung vor Abschluss des Promotionsverfahrens nicht vornehmen werde. Die Bestimmungen der Promotionsordnung sind mir bekannt. Die von mir vorgelegte Dissertation ist von Prof. Dr. Andreas Eckart und Prof. Dr. J. Anton Zensus betreut worden.

Bonn, 5th July 2020

Anne-Kathrin Baczko

Publications / Teilpublikationen

- Fromm, C. M.; Younsi, Z.; **Baczko, A.**; Mizuno, Y.; Porth, O.; Perucho, M.; Olivares, H.; Nathanail, A.; Angelakis, E.; Ros, E.; Zensus, J. A. and Rezzolla, L., 2019, *Using evolutionary algorithms to model relativistic jets. Application to NGC 1052*, A&A, 629, A4
- **Baczko, A.-K.**; Schulz, R.; Kadler, M.; Ros, E.; Perucho, M.; Fromm, C. M. and Wilms, J., 2019, *Asymmetric jet production in the active galactic nucleus of NGC 1052*, A&A, 623, A27
- **Baczko, A.-K.**; Schulz, R.; Ros, E.; Kadler, M.; Perucho, M. and Wilms, J., 2016, *Millimeter VLBI of NGC 1052: Dynamics*, Galaxies, 4, 48
- **Baczko, A.-K.**; Schulz, R.; Kadler, M.; Ros, E.; Perucho, M.; Krichbaum, T. P.; Böck, M.; Bremer, M.; Grossberger, C.; Lindqvist, M.; Lobanov, A. P.; Mannheim, K.; Martí-Vidal, I.; Müller, C.; Wilms, J. and Zensus, J. A., 2016, *A highly magnetized twin-jet base pinpoints a supermassive black hole*, A&A, 593, A47

Anne-Kathrin Baczko

Curriculum Vitae

Max-Planck-Institut für Radioastronomie
Auf dem Hügel 69
53121 Bonn, Germany
☎ +49 160 93842364
☎ +49 228-525-385
✉ baczko@mpifr-bonn.mpg.de

Persönliche Daten

Geburt: 17. July 1988 in Erlangen, Deutschland
Staats- Deutsch
angehörigkeit

Ausbildung

- seit 3/2016 **Doktorand**, *Max-Planck-Institut für Radioastronomie*, Bonn, Deutschland.
Titel: “Multi-Frequency VLBI Observations of the Active Galaxy NGC 1052.”
wiss. Betreuer: Prof. Dr. A. Eckart, Prof. Dr. A. Zensus, Prof. Dr. E. Ros und Prof. Dr. M. Kadler
- 9/2012 – **Master of Science in Physik**, *Friedrich-Alexander-Universität*, Erlangen, Deutschland.
5/2015 Titel: “Multi-Epoch Millimeter VLBI Observations of the Twin-Jet System in NGC 1052”
(supervisors: Prof. Dr. M. Kadler, Prof. Dr. J. Wilms)
- 9/2008 – **Bachelor of Science in Physik**, *Friedrich-Alexander-University*, Erlangen, Deutschland.
9/2012 Titel: “Calibration and imaging of GMVA observations of NGC 1052”
(wiss. Betreuer: Prof. Dr. M. Kadler, Prof. Dr. J. Wilms)
- 2008 **Abitur** (equivalent to high school diploma), *Christian-Ernst-Gymnasium*, Erlangen, Deutschland.
Leistungskurse in Physik und Kunst

Berufserfahrung

- 9/2015 – **Stipendiat**, *Max-Planck-Institut für Radioastronomie*, Bonn, Deutschland.
3/2016 cm & mm radio-interferometric (VLBI) data calibration and analysis (wiss. Betreuer: Prof. Dr. E. Ros, Prof. Dr. M. Kadler & Prof. Dr. A. Zensus)
- 4/2010 – **Studentische Hilfskraft**, *Dr. Karl-Remeis Sternwarte*, Bamberg, Deutschland.
9/2015
 - cm & mm radio-interferometric (VLBI) data calibration and analysis (wiss. Betreuer: Prof. Dr. M. Kadler & Prof. Dr. E. Ros)
 - Kinematic analysis of the VLBI jet in the active galactic nucleus of AP Lib (wiss. Betreuer: Prof. Dr. M. Kadler)